

2013-01-01

Microstructure and Properties for Titanium Aluminide Superalloy Prototypes Fabricated by Electron Beam Melting and Thermally Processed

Jennifer Hernandez

University of Texas at El Paso, jhernandez42@miners.utep.edu

Follow this and additional works at: https://digitalcommons.utep.edu/open_etd



Part of the [Materials Science and Engineering Commons](#), and the [Mechanics of Materials Commons](#)

Recommended Citation

Hernandez, Jennifer, "Microstructure and Properties for Titanium Aluminide Superalloy Prototypes Fabricated by Electron Beam Melting and Thermally Processed" (2013). *Open Access Theses & Dissertations*. 1838.
https://digitalcommons.utep.edu/open_etd/1838

This is brought to you for free and open access by DigitalCommons@UTEP. It has been accepted for inclusion in Open Access Theses & Dissertations by an authorized administrator of DigitalCommons@UTEP. For more information, please contact lweber@utep.edu.

MICROSTRUCTURES AND PROPERTIES FOR TITANIUM ALUMINIDE
SUPERALLOY PROTOTYPES FABRICATED BY ELECTRON BEAM
MELTING AND THERMALLY PROCESSED

JENNIFER HERNANDEZ

Materials Science and Engineering

APPROVED:

Lawrence E. Murr, Ph.D., Chair

Stephen W. Stafford, Ph.D.

Felicia S. Manciu, Ph.D.

Russell R. Chianelli, Ph.D.

Benjamin C. Flores, Ph.D.
Dean of the Graduate School

by
Jennifer Hernandez
2013

DEDICATION

This is dedicated to my parents, Antonio and Antonia Elorreaga, my love and best friend, Matthew Flores, and my sister and brother, Andrea and Jason Elorreaga. I could never have achieved this without their faith, support, and constant encouragement during all these years of study. To Krista Amato, I couldn't have had a better friend to experience it all with. Seven years together every step of the way! I also dedicate this to my God and Lord for being by my side and giving me the strength to pursue and achieve my goals.

I can do all things through Christ who strengthens me. - Philippians 4:13

**MICROSTRUCTURES AND PROPERTIES FOR TITANIUM ALUMINIDE
SUPERALLOY PROTOTYPES FABRICATED BY ELECTRON BEAM
MELTING AND THERMALLY PROCESSED**

by

JENNIFER HERNANDEZ,

Bachelor of Science in Metallurgical and Materials Engineering

DISSERTATION

Presented to the Faculty of the Graduate School of

The University of Texas at El Paso

in Partial Fulfillment

of the Requirements

for the Degree of

DOCTOR OF PHILOSOPHY

Materials Science and Engineering

THE UNIVERSITY OF TEXAS AT EL PASO

May 2013

ACKNOWLEDGEMENTS

I would like to express the deepest appreciation to my committee chair, Professor Lawrence E. Murr, who not only supported and advised me through my dissertation research, but gave me the opportunity to experience more than I ever thought I would. Without his help and guidance this dissertation would not have been possible. Also, to Frank Medina and the W.M. Keck Center for their help and support, as well as my research group, Dr. Sara Gaytan, Dr. Diana Ramirez, Dr. Krista Amato, Edwin Martinez, and Patrick Shindo. I thank you all very much from the bottom of my heart.

ABSTRACT

Gamma TiAl has been considered to be an ideal replacement for Ni-base superalloy aerospace applications, particularly in weight-critical applications. While bulk, fully dense gamma-TiAl is 50% less dense than Ni-base superalloys, it also has excellent mechanical properties at high temperature (up to $\sim 800^{\circ}\text{C}$). Pre alloyed (Ti-48Al-2Cr-2Nb) powder was used to fabricate solid, fully dense (3.85 g/cm^3) components and foam components with densities ranging from 0.33 g/cm^3 to 0.46 g/cm^3 by electron beam melting (EBM). A 10:1 blend of 2-phase TiAl (Ti-48Al-2Cr-2Nb in $\text{at}\%$) : Inconel 625 (Ni-22Cr-6Mo-2Nb in $\text{at}\%$) pre-alloyed powders produced a complex alloy having the composition 44Ti-39Al-7Ni-4Nb-4Cr-2Mo (in $\text{at}\%$). Solid, reticulated mesh samples and stochastic foam samples were fabricated by electron beam melting (EBM) using this blended alloy.

The microstructures of the solid and open-cellular components were observed by optical metallography (OM) and transmission electron microscopy (TEM), and confirmed by XRD analysis. The microstructure and residual hardness for solid components of 2-phase TiAl and Inconel 625 fabricated by EBM were compared to that of the blended alloy. The 2-phase TiAl alloy exhibited a duplex, equiaxed γ (TiAl) grain structure ($15\text{ }\mu\text{m}$) with lamellar colonies characterized by thin α_2 (Ti_3Al) plates $\sim 20\text{ nm}$ thick having an orientation relationship: $(111)\gamma\parallel(0001)\alpha_2$. The hardness (HV) of the blended alloy reached 7.5 GPa compared to 1.4 GPa for the Alloy 625 and 4.0 for the 2-phase TiAl alloy. Relative stiffness versus relative density values were plotted on a log-log basis for the reticulated mesh and stochastic foam samples for the blended alloy and were consistent with other alloys fitted to a straight line with a slope $n=2$ for ideal open cellular materials.

TABLE OF CONTENTS

ACKNOWLEDGEMENTS.....	v
ABSTRACT	vi
TABLE OF CONTENTS	vii
LIST OF TABLES.....	ix
LIST OF FIGURES	x
PROBLEM STATEMENT	1
PROPOSAL.....	1
CHAPTER 1: INTRODUCTION.....	2
CHAPTER 2: BACKGROUND	4
2.1 Gamma Titanium Aluminides	4
2.2 Additive Manufacturing.....	5
2.3 Applications	6
CHAPTER 3: DOCUMENTATION OF PUBLISHED WORK.....	7
CHAPTER 4: MATERIAL AND METHODS	8
4.1 Manufacturing of specimens: solid, reticulated mesh, and stochastic foam.....	8
4.2 Mesh and Foam Building Strategy	12
4.3 Sample Preparation.....	14
4.4 Microscopy	14
4.4.1 Optical Microscopy (OM)	14
4.4.2 Scanning Electron Microscopy (SEM).....	14
4.4.3 Transmission Electron Microscopy (TEM)	15
4.5 X-Ray Diffraction	15
4.6 Hardness	15
4.7 Dynamic Stiffness.....	15
4.8 Thermal Post-Processing Treatment.....	16
CHAPTER 5: RESULTS.....	17
5.1 Microstructures for Two-Phase Gamma Titanium Aluminide Fabricated by Electron Beam Melting	17
5.1.1 As-Fabricated EBM Components.....	17

5.1.2 Thermal Post-Processing	38
5.1.3 Discussion.....	45
5.1.4 Summary.....	47
5.2 Microstructures and Properties for a Superalloy Powder Mixture Processed by Electron Beam Melting	48
5.2.1 Comparative Microstructures for Solid Alloy 625, 2-Phase TiAl, and Blended TiAl ...	52
5.2.3 Open Cellular Mesh and Foam Components.....	63
5.2.4 Hardness Measurements	71
5.2.5 Measurement of Dynamic Stiffness for Blended TiAl Mesh and Foam Components: Implications for Ideal Foam Model	71
5.2.6 Summary.....	73
CHAPTER 6: DISCUSSION	75
6.1 Transmission Electron Microscopy	75
6.2 Hardness	76
6.3 Dynamic Stiffness.....	77
CHAPTER 7: CONCLUSIONS	78
REFERENCES	79
APPENDIX A: PERMISSION TO INCLUDE MATERIAL FROM THE JOURNAL METALLOGRAPHY, MICROSTRUCTURE, AND ANALYSIS	82
APPENDIX B: PERMISSION TO INCLUDE MATERIAL FROM THE JOURNAL OF MATERIALS SCIENCE RESEARCH.....	84
VITA.....	85

LIST OF TABLES

Table 5.2.1: Chemical Composition for Pre-Alloyed Powders and EBM Fabricated Solid Components.	51
Table 5.2.2: Chemical Composition for Blended TiAl Components Fabricated by EBM.	61
Table 5.2.3: Dynamic Stiffness and Density Measurements for TiAl/Ni-Cr Alloy (Blended TiAl).....	72

LIST OF FIGURES

Figure 1.1: Schematic of the central portion of the binary Ti-Al phase diagram (McCullough et al, 1989). The hatched region is the composition ranges used for two-phase engineering materials. The dashed line represents the alloy composition used in this study.	3
Figure 4.1.1: Schematic of an A2 EBM system and two solid components with different geometries.	9
Figure 4.1.2: Pre-alloyed TiAl precursor powder particles (a) and powder particle size distribution with average particle size shown to be 52 μm (b).	11
Figure 4.1.3: Pre-alloyed Inconel 625 powder particles.	12
Figure 4.2.1: Software model views using dode-thin software element; dode-thin element orientations at 0° (a) and 45° (b) with corresponding unit-cell representation and software model view of mesh array (c) (Murr, 2010).	13
Figure 4.2.2: Chronological representation of the process to manufacture foam components by additive manufacturing.	13
Figure 5.1.1: Magnified views for the precursor Ti-48Al-2Cr-2Nb powder in Figure 4.1.2.	18
Figure 5.1.2: LOM section views showing internal, equiaxed, dendritic grain structure ($\sim 2\ \mu\text{m}$) of the pre-alloyed powder.	19
Figure 5.1.3: XRD spectra for the Ti-48Al-2Cr-2Nb precursor powder in Figure 4.1.2(a).	20
Figure 5.1.4: 3D-LOM composite view for dual-phase γ -TiAl microstructure representative of the EBM fabricated rectangular solid (Figure 4.1.1). Build direction is indicated by arrow (left).	20
Figure 5.1.5: 3D-LOM composite view for dual-phase γ -TiAl microstructure representative of the EBM fabricated cylindrical solid (Figure 4.1.1). Build direction is indicated by arrow (left).	21
Figure 5.1.6: XRD spectra corresponding to the horizontal (a) and vertical (b) reference planes for a rectangular EBM-fabricated block (represented by Figure 5.1.4).	22
Figure 5.1.7: XRD spectra corresponding to the horizontal (a) and vertical (b) reference planes for a cylindrical EBM-fabricated component (represented by Figure 5.1.5).	23
Figure 5.1.8: Low-magnification LOM image showing additive-layer structures in the vertical reference plane for a cylindrical EBM-fabricated component (represented by Figure 5.1.5).	24
Figure 5.1.9: Ti-48Al-2Cr-2Nb foam prototypes fabricated by EBM. Top row shows edge orientations while bottom row shows face orientations at slight larger magnifications. Measured densities are indicated.	25
Figure 5.1.10: SEM views for ligament structure of foam sample ($\rho = 0.33\ \text{g/cm}^3$) showing partially sintered powder particles. (a) Low-magnification SEM image. (b) High-magnification view showing partially sintered powder particles.	26
Figure 5.1.11: Foam ligament microstructure: OM image showing duplex (two-phase) structure.	27
Figure 5.1.12: XRD spectra for the foam components.	28
Figure 5.1.13: Comparative TEM images for two-phase microstructures in EBM-fabricated γ -TiAl cylindrical component. (a) Horizontal reference plane. (b) Vertical reference plane (Figure 5.1.4)	29
Figure 5.1.14: TEM bright-field image showing lamellar (α_2/γ) filled grain (top) and primarily γ -TiAl grains (bottom).	30
Figure 5.1.15: Magnified TEM bright-field image showing thin α_2 -Ti ₃ Al plates in γ -TiAl. The SAED pattern inset shows rows of γ and α_2 diffraction spots. These rows are in the $[111]_\gamma$ direction (arrow). The grain surface orientation is (123).	31
Figure 5.1.16: TEM bright-field (a) dark-field (b) sequence for α_2/γ lamellar microstructure. The DF image in (b) utilized the apertured γ diffraction spot shown circled in the SAED pattern inset. Only small fraction of the γ -phase regions are imaged.	32

Figure 5.1.17: TEM bright-field image for dislocation and lamellar microstructures observed in the horizontal reference plane for an EBM-fabricated cylindrical component (Figure 4.1.1).	34
Figure 5.1.18: TEM image showing a large area composed of dislocation dipoles in a sample similar to Figure 5.1.17. The α_2 lamellae at the extreme left of the micrograph exhibit strain-field contrast features (arrow) which may arise from interfacial steps or ledges.	35
Figure 5.1.19: TEM showing lamellar microstructures in the vertical reference plane for an EBM-fabricated cylindrical component. The SAED pattern inset is the same as that in Figure 5.1.15. The arrow (black in the image and white in the SAED pattern) represent the $[111]_\gamma$ direction. The surface orientation is (123).	36
Figure 5.1.20: Bright-field (a) dark-field (b) TEM image sequence of α_2/γ lamellar microstructure in an EBM-fabricated cylindrical component (in the vertical reference plane). The DF image in (b) corresponds to the circled α_2 diffraction spot in the SAED pattern inset. The DF images in (b) represent portions of α_2 plates.	37
Figure 5.1.21: LOM views for annealed EBM-built blocks in the vertical reference plane (parallel to the build direction). (a) Anneal 1.): 1150°C at 5 h. (b) Anneal 2.): 1380°C at 1 h.	39
Figure 5.1.22: Bright-field TEM images representing Anneal 1.) (1150°C at 5 h.); corresponding to the LOM image in Figure 5.1.21(a). (a) Mixture of fine α_2 and γ -twins. (b) Similar features for a larger grain with a (123) surface orientation. Corresponding γ - $\{111\}$ trace direction are noted.	40
Figure 5.1.23: TEM bright-field (a) dark-field (b) image sequence utilizing the combined α_2/γ diffraction spots shown circled in the SAED pattern inset in (b). The TEM image sequence corresponds to Anneal 2.) (1380°C at 1 h.) in the vertical reference plane, characteristic of the LOM image in Figure 5.1.21(b). The arrow in the SAED pattern inset corresponds to $[111]$ for a (123) grain surface orientation.	41
Figure 5.1.24: XRD spectra corresponding to the vertical reference planes represented in Figure 5.1.21(a) and (b), respectively, for annealed 1.) (a) and 2.) (b) EBM-fabricated components.	43
Figure 5.1.25: TEM bright-field image for γ -twins with (111) in a γ -TiAl (222) grain surface orientation. A DF image portion is inserted and corresponds to the twinned regions referenced by the arrow(s).	44
Figure 5.1.26: Comparison of Vickers microindentation hardness averages (HV) and Rockwell C-scale hardness averages (HRC) for experimental specimens noted. The block, cylinder, Anneal 1.), and Anneal 2.) specimens averaged measurements made in the horizontal and vertical reference planes.	46
Figure 5.2.1: SEM views of pre-alloyed powder microstructure. (a) Gamma TiAl. (b) Inconel 625.	49
Figure 5.2.2: XRD spectra for pre-alloyed powders. (a) Gamma TiAl. (b) Inconel 625.	50
Figure 5.2.3: 3D OM composite section for an EBM fabricated Alloy 625 component. The build direction is shown by the lower right arrow. Grain boundaries are denoted by GB.	53
Figure 5.2.4: TEM vertical plane section view (parallel to the build direction in Figure 5.2.3; characteristic of the circled zone (arrow)). The grain surface orientation is (110). The trace directions shown correspond to $[110]$ (1); $[112]$ (2); $[112]$ (3).	54
Figure 5.2.5: XRD spectra corresponding to the horizontal (a) and vertical (b) reference plane for an Inconel 625 EBM-fabricated cylindrical component (Figure 5.2.3).	55
Figure 5.2.6: 3D OM image composite section for an EBM-fabricated 2-phase TiAl component. The build direction is shown by the arrow (lower right).	56
Figure 5.2.7: 3D OM image composite section for an EBM-fabricated blended TiAl component. The build direction is shown by the arrow (lower right).	57
Figure 5.2.9: XRD spectra corresponding to the horizontal reference plane (a) and vertical reference plane (b) for a 2-phase TiAl EBM-fabricated component.	59
Figure 5.2.10: XRD spectra corresponding to the horizontal reference plane (a) and vertical reference plane (b) for a blended TiAl EBM-fabricated component.	60
Figure 5.2.11: SEM analysis sequence representing an area corresponding to the horizontal surface region shown in the box in Figure 5.2.7. (a) BE image showing complex phase structure and atomic	

number (Z) contrast. Phase regions are denoted A, B, C, D. (b) Ti X-ray map. (c) Ni X-ray map. (d) Mo X-ray map. (20 kV accelerating potential).....	63
Figure 5.2.12: EBM-fabricated open-cellular structures. (a) Mesh components observed in the face plane. Arrow shows the build direction. (b) Mesh components observed along an edge at 45° to the face view in (a). Densities shown in units of g/cm ³ . (c) Foam components observed in the face plane. Densities shown in units of g/cm ³	65
Figure 5.2.13: Blended TiAl mesh (a) and foam (b) cross-sections in the top face section perpendicular to the build direction. (a) corresponds to a density of 1.11 g/cm ³ ; (b) corresponds to a density of 0.74 g/cm ³	65
Figure 5.2.14: Polished and etched section for a mesh strut shown in Figure 5.2.13(a). Unmelted, liquid-phase sintered TiAl powder particles are observed in (a). (b) shows a magnified view of (a) (arrow). ..	67
Figure 5.2.15: 3D OM composite for a mesh strut cross-section. The build direction is shown by arrow.	68
Figure 5.2.16: 3D OM composite for a foam ligament cross-section. The build direction is shown by arrow.	68
Figure 5.2.17: XRD spectra for blended TiAl mesh strut and foam ligament section. (a) Horizontal reference plane for a mesh strut. (b) Horizontal reference plane for a foam ligament.	69
Figure 5.2.18: Backscatter electron (BE) image showing phase morphologies and stoichiometries referenced to Figure 5.2.11(a): A, B, C, and D.	70
Figure 5.2.19: Vickers microindentation hardness (HV) and Rockwell C-scale macrohardness (HRC) measurements for blended TiAl alloy EBM-fabricated components.	71
Figure 5.2.20: Log-log plot of measured stiffness versus density for the blended TiAl mesh and foam samples.	73
Figure 6.1.1: TEM horizontal plane section views (perpendicular to the build direction). (a) 2-phase TiAl. (b) Blended TiAl.	75
Figure 6.2.1: Comparison of Vickers microindentation hardness (HV) and Rockwell C-scale macrohardness (HRC) measurements. Blended refers to the blended TiAl components – 10:1 – 2-phase TiAl : Inconel 625.....	76
Figure 6.3.1: Log-log plot of relative stiffness versus relative density for blended TiAl mesh and foam components (indicated by Ti-Al alloy) in comparison with Ti-6Al-4V and Co-based alloy data from Murr et al. (2010a, 2010b).	77

PROBLEM STATEMENT

Manufacturing technology has greatly improved in the past couple of decades. The need for newer and more advanced materials has also become of great interest, as well as characterizing these materials in hopes of successfully obtaining results that reveal excellent mechanical properties. Additive manufacturing by electron beam melting has shown to have great potential in producing near-net shaped, complex components using a 3D-CAD model in which pre-alloyed powder is melted layer by layer. Titanium aluminides have not yet been fabricated in porous or open-cellular structure forms successfully, unlike that of nickel-titanium or nickel aluminides (Hernandez, *et al.*, 2012a). The aim of this study is to obtain these types of components fabricated by electron beam melting technology and compare the results to that of solid, fully dense components fabricated by electron beam melting (EBM).

PROPOSAL

The purpose of this study is to characterize the properties of Ti-48Al-2Cr-2Nb prototypes fabricated by electron beam melting (EBM) and explore ways of enhancing titanium aluminides. It is important to obtain results comparable to that of other results shown in the literature for solid, fully dense and open-cellular components. Different heat treatment cycles are also important to investigate in order to achieve an ideal microstructure and improve the mechanical properties of the as-fabricated material. The temperature and time are the parameters that must be determined for the heat treatment process. It is important to gather literature relevant to this study to fully understand the process and results obtained. All properties and microstructures will be analyzed using optical microscope, scanning electron microscope, and transmission electron microscope, as well as micro and macro hardness testers. The main focus of this project is to obtain results for open-cellular TiAl components fabricated by electron beam melting technology comparable to that of solid, fully dense components.

CHAPTER 1: INTRODUCTION

Research has shown that γ -TiAl-based alloys are useful in high temperature structural applications, where low density and high strength are needed, to replace the heavier nickel-based superalloys. This is mainly due to its excellent mechanical properties such as low density ($\sim 3.8 \text{ g/cm}^3$), high specific yield strength, good oxidation resistance and high specific stiffness up to high temperatures. These properties provide considerable potential for use in aerospace components, automotive engine components and structural applications in oxidizing environments up to $\sim 700^\circ\text{C}$ (Hernandez, *et al.*, 2012a).

Single phase γ -TiAl exhibits poor ductility and fracture toughness at room temperature. However, improved ductility and toughness can be obtained in two-phase γ -TiAl in the $(\gamma + \alpha)$ region of the phase diagram, shown in Figure 1.1. Two-phase γ -TiAl-based alloys are used for structural applications, consisting of phases γ -TiAl and α_2 -Ti₃Al. Extensive research has been made to develop this two-phase γ -TiAl-based alloy. The mechanical properties depend greatly on the type of microstructure of the material, which is considered in the design process of the material for structural applications. A desired microstructure can be obtained by post thermal processing using certain cycles. The actual γ/α_2 -volume fraction is strongly influenced by heat treating, which affects the mechanical properties.

Conventional manufacturing methods of titanium aluminides is possible but has shown to be difficult due to the fact that TiAl is brittle causing serious cracking problems to occur within the material. One application where TiAl can be used to replace the heavier nickel based superalloy is for low pressure turbine blades. However, TiAl components fabricated by conventional manufacturing methods would need post manufacturing to obtain the complex structure of the blade. This is also challenging due to the material's low fracture toughness causing the material to fracture very easily.

Electron beam melting technology produces near net-shaped components by additive manufacturing using pre-alloyed powders and a 3D CAD model. Solid, fully dense γ -TiAl components fabricated by EBM have been developed (Hernandez, *et al.*, 2012a). Electron beam melting is an advanced processing technique which has low material waste, few internal defects compared to casting,

and very little, if any, post-manufacturing is needed on complex structures. Current research is still being developed for open-cellular structure components fabricated by electron beam melting (EBM). Titanium aluminides, in this form, have yet to be developed, unlike copper, CoCr or Ti-6Al-4V alloy components.

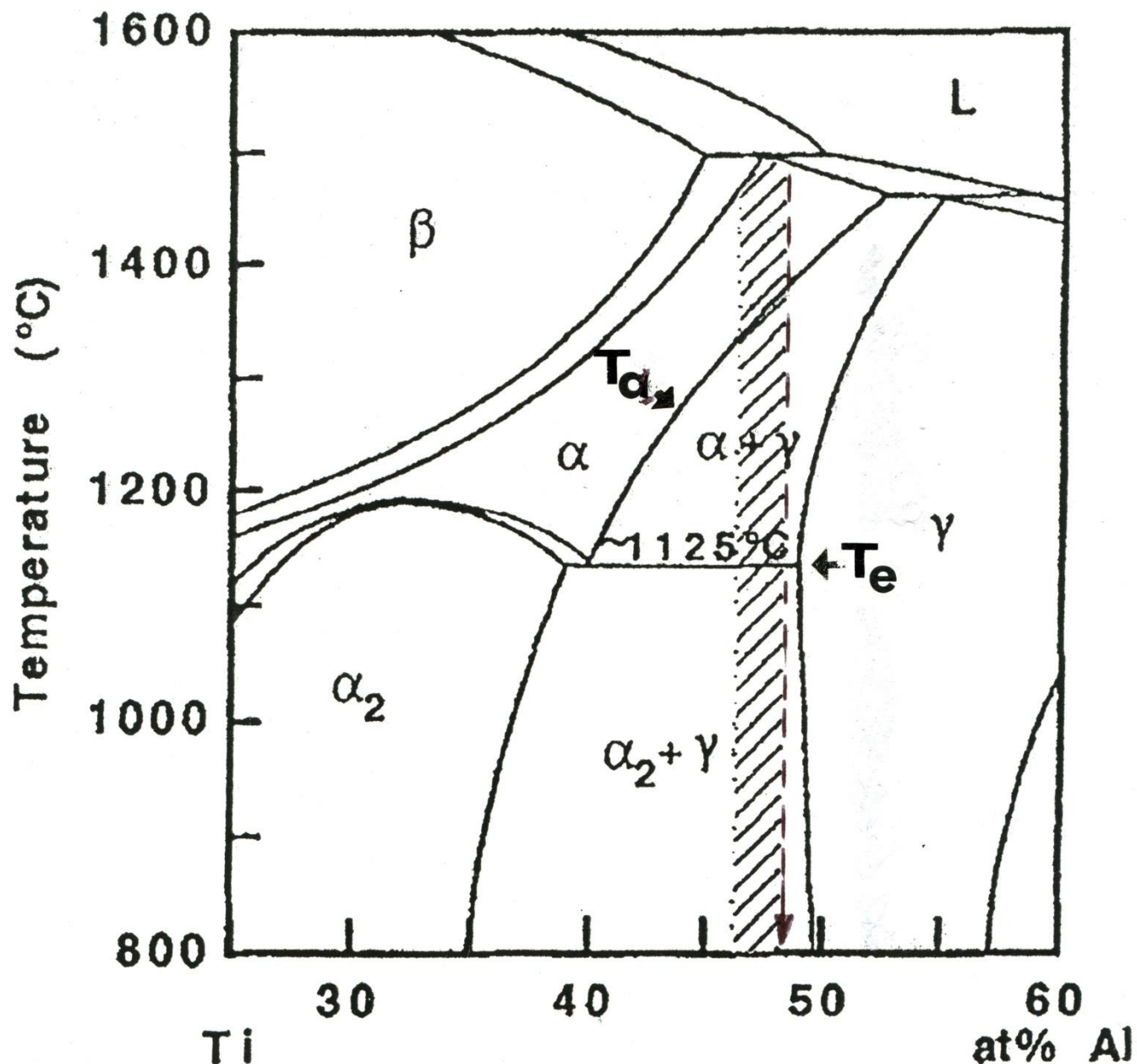


Figure 1.1: Schematic of the central portion of the binary Ti-Al phase diagram (McCullough et al, 1989). The hatched region is the composition ranges used for two-phase engineering materials. The dashed line represents the alloy composition used in this study.

CHAPTER 2: BACKGROUND

2.1 GAMMA TITANIUM ALUMINIDES

As noted before, the single phase γ -TiAl-based alloys have low ductility and fracture toughness at room temperature, whereas, two-phase γ -TiAl-based alloys have improved ductility and fracture toughness with compositions in the $(\gamma + \alpha)$ two-phase region in the binary phase diagram of Ti-Al, shown in Figure 1.1 (Hernandez, *et al.*, 2012). The desired two-phases are γ -TiAl with the ordered face-centered tetragonal Ll_0 structure (p4mmm; $a \cong 0.41 \text{ nm} \cong b$ and essentially, fcc), and α_2 -Ti₃Al with the hexagonal DO_{19} structure (p63/mmc; $a = 0.58 \text{ nm}$, $c = 0.46 \text{ nm}$) (Appel, 1998).

The purpose of obtaining a two-phase γ -TiAl-based alloy is to achieve balanced properties, which are greatly impacted by the composition of the alloy. It has been found that the composition (at. %) of conventional engineering γ -TiAl-based alloys is represented by:

$$\text{Ti}_{45-52} - \text{Al}_{45-48} - \text{X}_{1-3} - \text{Y}_{2-5} - \text{Z}_{<1} \quad (2)$$

where X = Cr, Mn, V; Y = Nb, Ta, W, Mo; Z = Si, B, C (Appel, *et al.*, 1998). The majority of the material properties are improved by the Nb-content, especially the oxidation resistance. The ductility can be improved by the addition of V, Mn, Mo, and Cr, and the γ -TiAl phase, at ambient temperatures, can be strengthened by adding Ta, Mo, W, and C (Appel, *et al.*, 1998). A decrease in the Al-content has a positive effect on low temperature ductility (Clemens, *et al.*, 2000). However, high Al-content shows good elevated temperature strength, creep resistance and environmental resistance (Froes, *et al.*, 1992). In this study, a composition of Ti-48Al-2Cr-2Nb is used because it has been researched and has shown to have great potential.

Gamma titanium aluminide, γ -TiAl, has been considered to replace the nickel-based superalloys commonly used in jet engines for high temperature applications due mainly to its much lower density. Even though the properties of nickel-based superalloys are superior to that of γ -TiAl, the much lower density of γ -TiAl allows for this material to have a much higher specific strength and specific ultimate tensile strength (Franzen, *et al.*, 2010).

The mechanical properties of two-phase γ -TiAl-based alloys are also greatly influenced by the microstructure. There are three different microstructures, lamellar, duplex, and equiaxed, that can

appear within this material. The lamellar structure is composed of alternating γ and α_2 platelets creating zebra-like grains, causing the material to be more ductile compared to that of the equiaxed structure. The equiaxed microstructure only appears in single γ phase material, having improved high temperature properties but poor room temperature properties and making the material very brittle. These two microstructures appear in two-phase γ -TiAl-based alloys as a mixture of equiaxed γ grains and lamellar colonies, also known as a duplex microstructure. The properties of both microstructures influence the overall properties of the material, including improved ductility. This type of microstructure is preferred for structural applications. The addition of the lamellar colonies not only improves the ductility of the material, creep resistance, fracture toughness, and strength at high temperature is also improved. The microstructure is not only affected by manufacturing processes but can also be altered by subjecting the as-fabricated material to different heat treatments.

2.2 ADDITIVE MANUFACTURING

Conventional manufacturing processes, including investment castings, wrought processes, and powder processing, of γ -TiAl-based alloys has shown to be difficult and have problems such as thermal stress-induced cracking (Froes, *et al.*, 1992). These difficulties and problems that occur within the material are the reason why there is little use of γ -TiAl-based alloys today. Recently, research has been made on the fabrication of γ -TiAl-based alloys by additive manufacturing using electron beam melting technology. Additive manufacturing uses a model that is initially generated using a three-dimensional Computer Aided Design, or 3D CAD, system, and are built layer by layer (Gibson, *et al.*, 2010). The thinner each layer is, the more precise the final part will be. Near net shaped components are obtained through this technology, as well as producing complex 3D components directly from the 3D CAD model.

There are many different types of commercialized additive manufacturing machines, in which each differ in the types of materials that can be used and how the layers are created and bonded to each other (Gibson, *et al.*, 2010). Novel research shows that this technology allows for successfully producing fully dense TiAl parts. The benefits of additive manufacturing are that parts are produced more rapidly compared to other manufacturing processes because multiple stages, such as post-

processing, can be removed. This technology reduces time to market, allows for mass customization, and reduces material waste and number of design iterations.

2.3 APPLICATIONS

Finding materials that have relatively low density but still show great mechanical properties at high temperatures is of great interest. Gamma titanium aluminide based alloys not only have low density, but also excellent mechanical properties at high temperatures, such as high strength, good oxidation resistance and high specific stiffness. All of these, and more, allow for this particular type of material to be a great candidate for applications in advanced aerospace engine and airframe components, as well as automotive components. This type of material is considered to be an “advanced” material because it can be “engineered” to exhibit properties required for a certain application (Froes, *et al.*, 1992).

There have already been a number of successful jet engine components that have been produced using this two-phase γ -TiAl-based superalloy by casting and ingot processes; however, none have yet to be flown (Froes, *et al.*, 1992). This alloy can also potentially be used in applications such as low-pressure turbine blades, bearing supports, compressor castings, and high and low pressure hangars.

CHAPTER 3: DOCUMENTATION OF PUBLISHED WORK

The majority of the material in this dissertation is composed of published work. The material/contents of Chapters 4, 5, and 6 can be found in the following two journal articles:

Hernandez, J., Murr, L.E., Gaytan, S.M., Martinez, E., Medina, F., Wicker, R.B., 2012a. Microstructures For Two-Phase Gamma Titanium Aluminide Fabricated by Electron Beam Melting. *Metallogr. Microstruct. Anal.* 1, 14-27.

Hernandez, J., Murr, L.E., Amato, K.N., Martinez, E., Shindo, P.W., Terrazas, C.A., Rodriguez, E., Medina, F., Wicker, R.B., Li, S.J., Cheng, X.Y., Yang, F., 2012. Microstructures and Properties for a Superalloy Powder Mixture Processed by Electron Beam Melting. *Journal of Materials Science Research*, Vol. 1, No. 3, 124-144.

Documentation for permission to use the cited articles above in this dissertation can be found in Appendix A and B.

CHAPTER 4: MATERIAL AND METHODS

4.1 MANUFACTURING OF SPECIMENS: SOLID, RETICULATED MESH, AND STOCHASTIC FOAM

Conventional manufacturing methods, like casting, forging or powder processing, of TiAl is difficult and expensive. The difficulty of processing TiAl is mainly due to the material's low ductility and fracture toughness. The biggest issue with this material is the high manufacturing cost which is why there is limited use of TiAl today. One processing route, in particular, that is being researched today is Electron Beam Melting, which can build near net shaped components. This technology offers high precision and high quality components.

The powder used for the EBM system is gas atomized, pre-alloyed powder. During the gas atomization process, high pressure inert gas is introduced into the stream of molten metal just before it is released through the nozzle. The gas expands, breaking the melt stream and allowing the molten metal to be atomized into fine metal droplets. The droplets become spherical particles just before reaching solidification (German, *et al.*, 2005).

A schematic of an Arcam A2 EBM system is shown in Figure 4.1.1, along with two samples of fully dense components with different geometries fabricated by EBM used in this study. During the EBM process, an electron beam generated by an electron gun with an acceleration potential of 60 kV is focused by two electromagnetic coils ((1) in Figure 4.1.1). The beam is focused to the desired diameter by the first magnetic coil and deflected to the desired point on the building table by the second magnetic coil. The beam diameter can focus to as small as 0.1mm. A tungsten filament emits the electrons and the current varies from 1-50 mA and the build chamber works under a vacuum of $\sim 10^{-4}$ Torr.

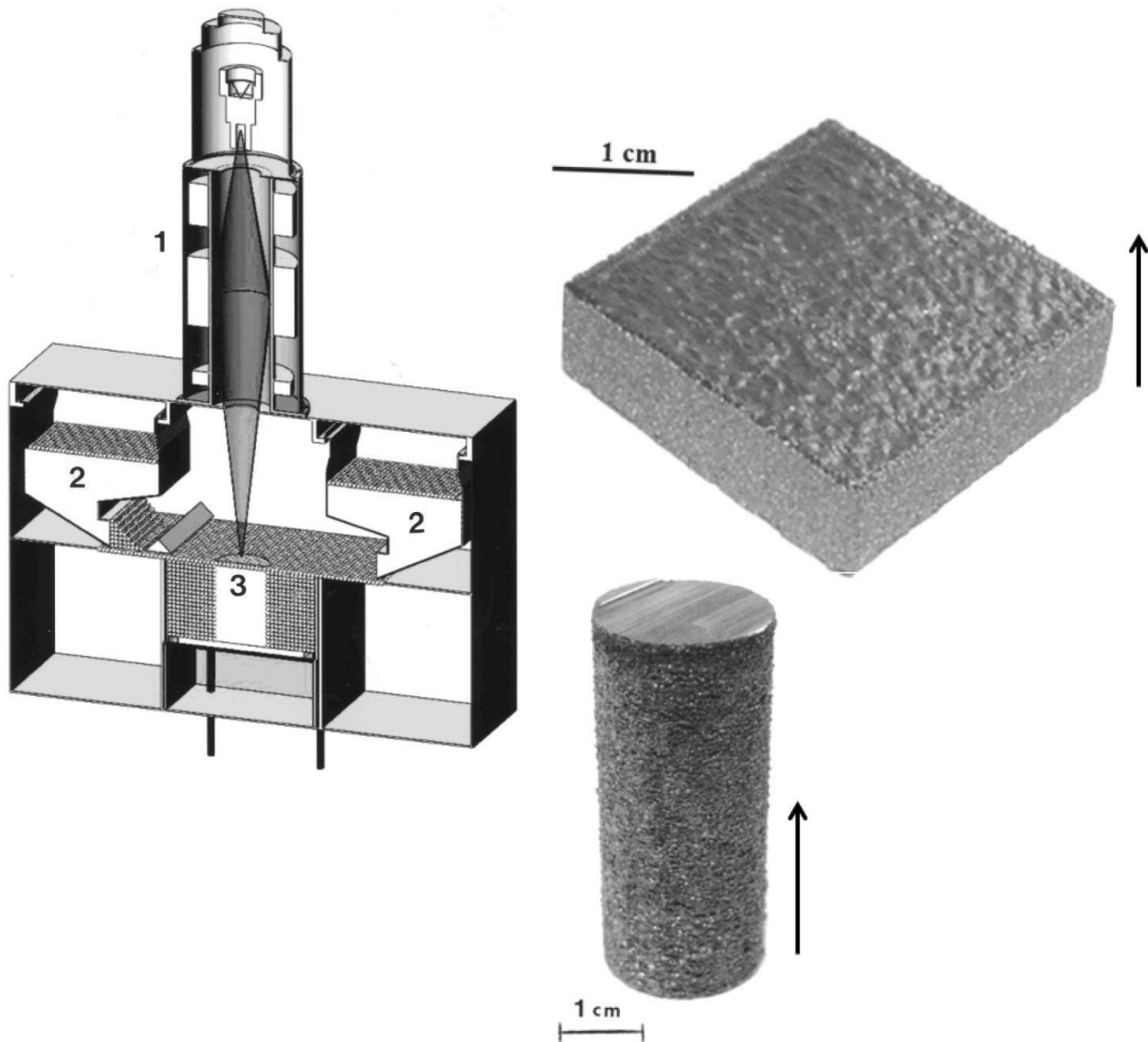


Figure 4.1.1: Schematic of an A2 EBM system and two solid components with different geometries.

The parts are built up layer-by-layer from gas atomized metal powder that is fed by gravity from cassettes ((2) in Figure 4.1.1) and raked onto the build table ((3) in Figure 4.1.1). Scan coils, directed by a three dimensional (3D) computer aided design (CAD) model, scan the beam across the powder selectively melting the powder to the exact geometry. The raked powder layer is pre-heated to a temperature of 80% that of the melting temperature, in which the beam is scanned rapidly at a higher beam current and multiple passes of the beam at a high scan rate; and, thereafter, the scan speed and current is reduced for the final melt scan (Hernandez, *et al.*, 2012a). When the layer is finished being

scanned and melted, the build table is lowered and a new layer of powder, $\sim 50\text{ }\mu\text{m}$, is raked out and the process is repeated until the entire component is completed. The maximum built size is 200x200x300 mm. The precursor powder used to build γ -TiAl components, shown in Figure 4.1.2(a), is rapidly solidified, atomized pre-alloyed powder with a composition of Ti-48at% Al-2at% Cr-2at% Nb. The particle size distribution is illustrated in Figure 4.1.2(b), as well as the average powder particle size, $\sim 52\text{ }\mu\text{m}$.

A 10:1 γ -TiAl : Alloy 625 powder mixture was used to fabricate solid, fully dense and open-cellular components, which produced blended TiAl components by EBM. A micrograph of the Alloy 625 powder is shown in Figure 4.1.3. The 2-phase TiAl powder has a melting point of $\sim 1460^\circ\text{C}$, while the Alloy 625 has a melting point of $\sim 1336^\circ\text{C}$. The EBM process allows for little waste material because there is a 95% powder recovery system that allows for the powder to be reused for subsequent building after it is sifted to use powders that are only in the proper range size.

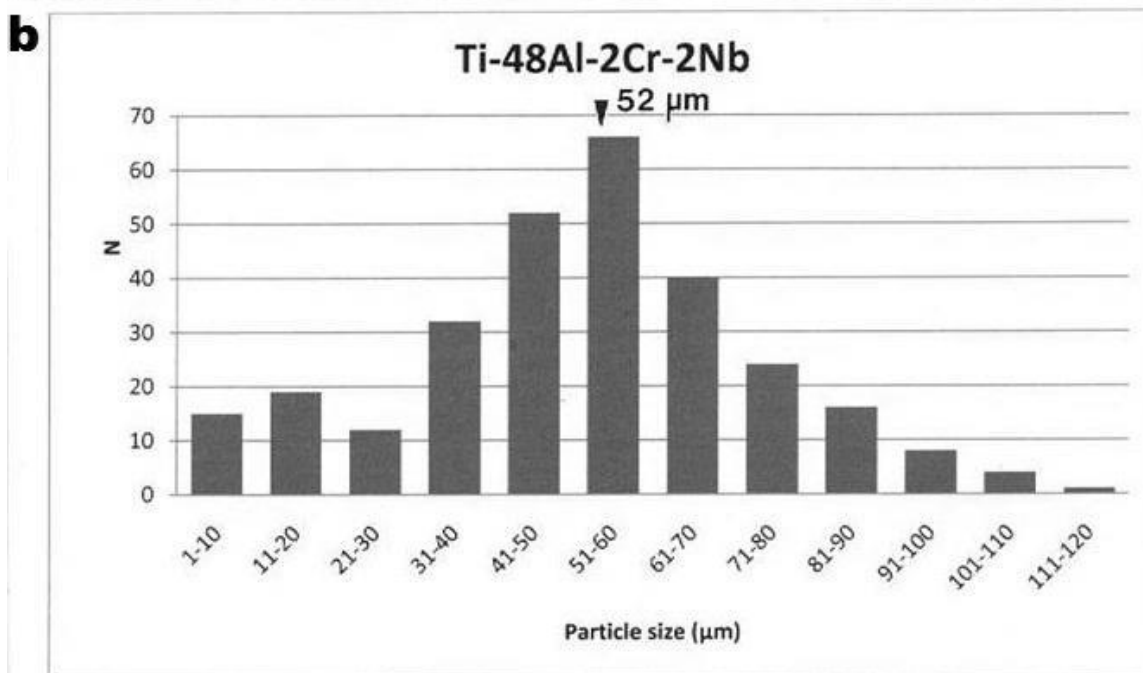
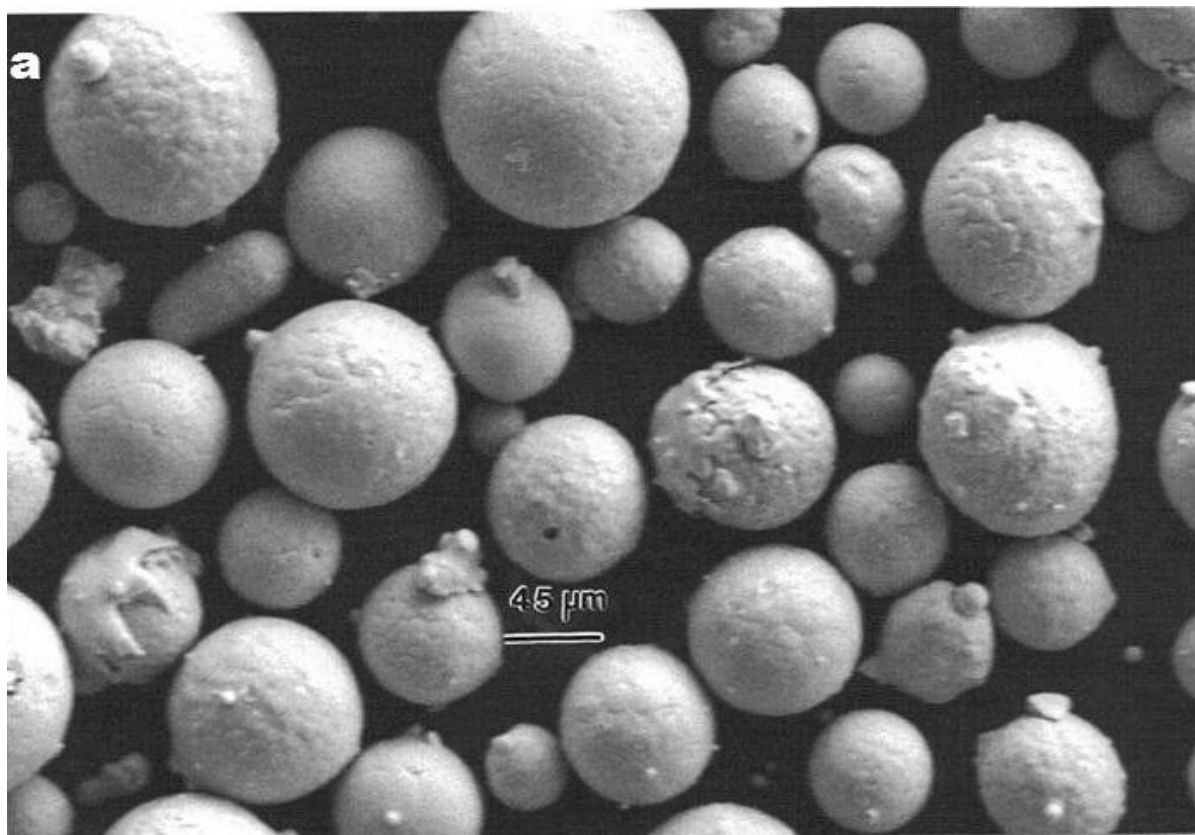


Figure 4.1.2: Pre-alloyed TiAl precursor powder particles (a) and powder particle size distribution with average particle size shown to be 52 μm (b).

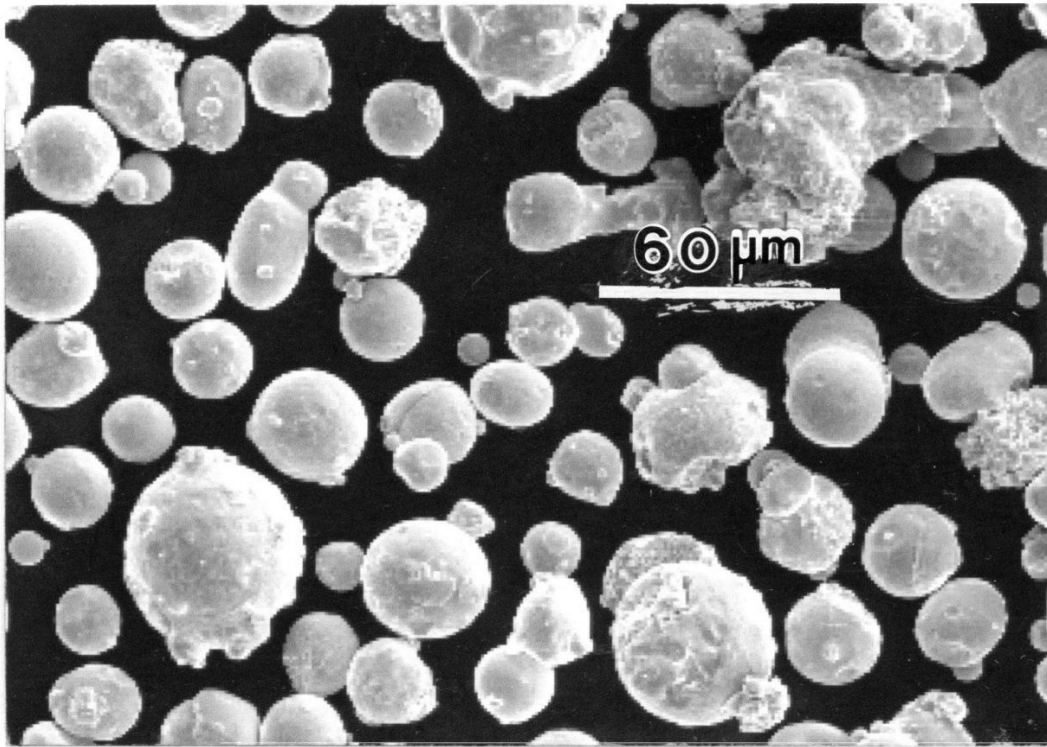


Figure 4.1.3: Pre-alloyed Inconel 625 powder particles.

4.2 MESH AND FOAM BUILDING STRATEGY

A series of dode-thin reticulated mesh components were fabricated by EBM using the same build process. However, in order to build these types of components, a so-called unit cell or lattice structure unit is obtained using dode-thin software. A 3D CAD model for a mesh array is produced by stacking one-unit layer of cells at a time, similar to growing single-crystal lattices (Murr, *et al.*, 2010a). The geometry of the mesh changes by changing the unit-cell dimension. The density of the mesh array decreases as the mesh unit-cell size increases because there is more open space or porosity. A schematic of a dode-thin unit cell, at 0° and 45°, is shown in Figure 4.2.1, along with a software model view of a mesh array.

The foam components are developed by the same building process, but first a CT scan of conventional aluminum foams is obtained (Murr, *et al.*, 2010b). Figure 4.2.1 shows the process from CT scan to Bitmap file to file-model representation of a unit cell. The digital layer data of the CT scan is converted into bitmap files with specific pixel dimensions representing image or model slices. A file-model is created which can be altered dimensionally to create pore size variations or ligament dimension

variations. This, in turn, allows for the fabrication of components with different densities (Murr, *et al.*, 2010b).

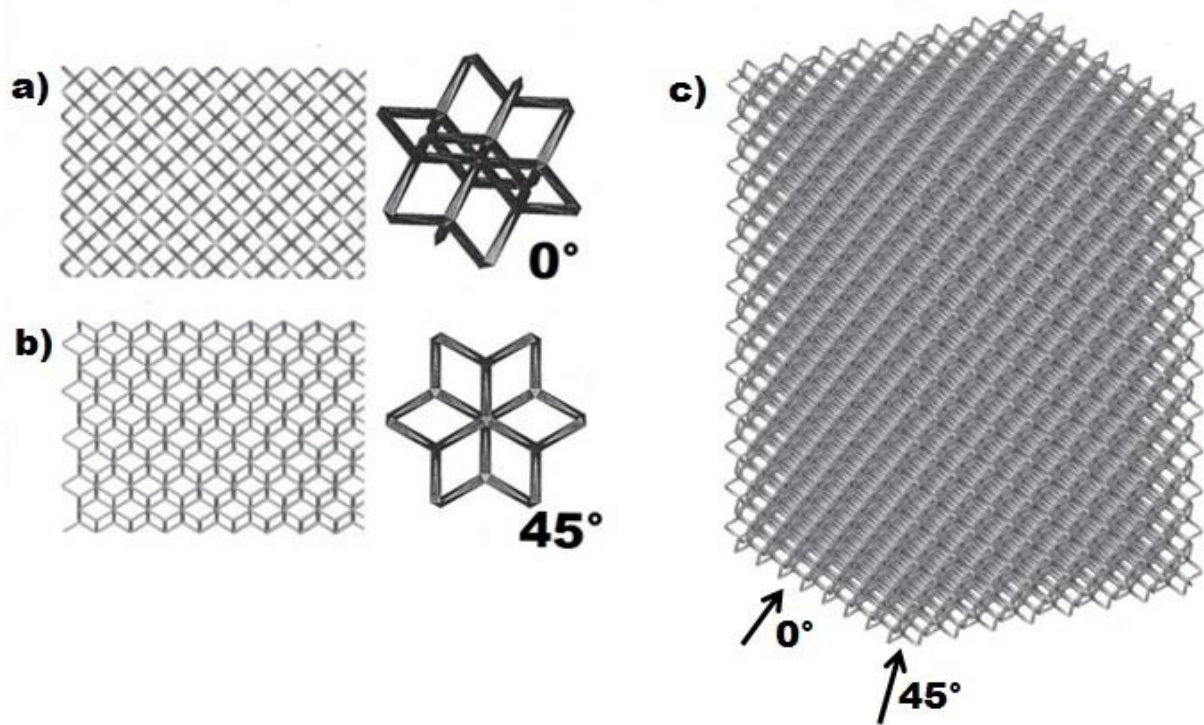


Figure 4.2.1: Software model views using dode-thin software element; dode-thin element orientations at 0° (a) and 45° (b) with corresponding unit-cell representation and software model view of mesh array (c) (Murr, 2010).

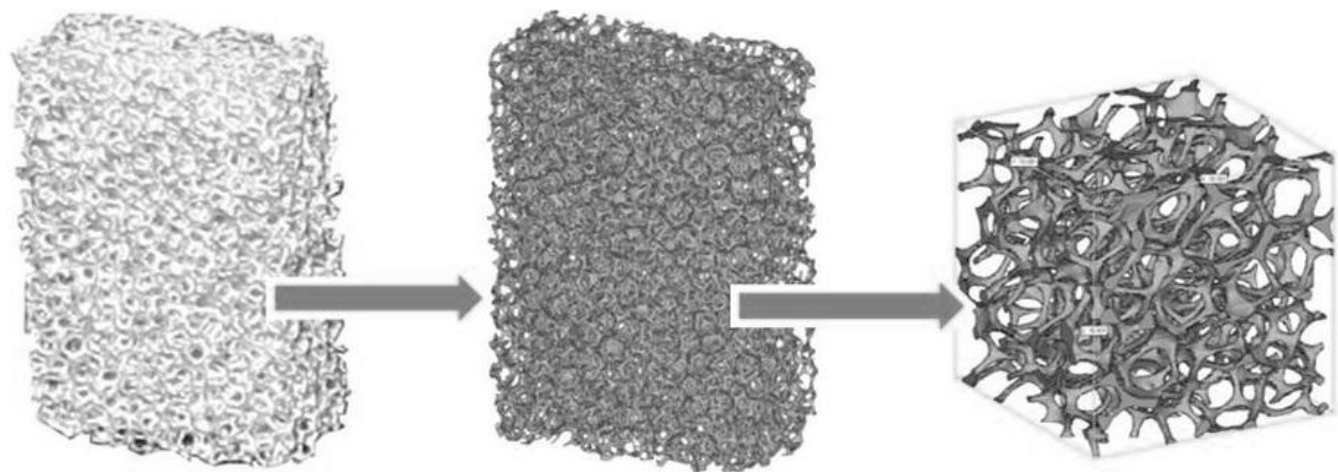


Figure 4.2.2: Chronological representation of the process to manufacture foam components by additive manufacturing.

4.3 SAMPLE PREPARATION

The solid, fully dense samples were cut both parallel, vertical plane, and perpendicular, horizontal plane, to the build direction to obtain smaller specimens to characterize the samples. The precursor powder, solid, mesh, and foam specimens were then mounted, area to be examined face down in plastic mount mold, using a mixture of 1:1 of Koldmount[®] specimen mounting material powder and self-curing liquid. The mounted specimens were polished on a polishing machine using SiC grit paper ranging from 80 (coarsest) to 4000 (finest) while water is running on the wheel to avoid the sample from heating. The sample must be rotated 90° after each grit paper is used. They were then polished on a soft polishing pad to a mirror finish using alumina solution from 1µm – 0.05µm and then rinsed in ethyl alcohol. The samples are ready to be etched when, to the naked eye, there are no visible scratches on the surface of the polished sample. TEM coupons were obtained by cutting samples from the solid components in the horizontal and vertical planes and grinding them down, using grit paper, to a thickness less than ~200 µm and punched into 3mm discs.

4.4 MICROSCOPY

4.4.1 Optical Microscopy (OM)

The pre-cursor powders, solid, mesh, and foam components fabricated by EBM were observed by optical metallography using a digital imaging Reichert MEF4/AM metallograph with an AMScope Microscope MD600 digital camera photographing the microstructure. In order to reveal the microstructure, the samples were etched utilizing a solution of 5 mL of HNO₃, 10 mL of HF, and 300 mL of H₂O. The etchant was washed away after ~1s under running water and the sample was rinsed with ethyl alcohol to remove any etchant that may be left on the sample.

4.4.2 Scanning Electron Microscopy (SEM)

The precursor powder, mesh and foam samples were also observed in a Hitachi S4800 field-emission scanning electron microscope (SEM) operated at 20kV utilizing secondary electron imaging. This helped in measuring various powder sizes in order to plot the particle size distribution and obtain the average particle size. An EDAX-EDS system fitted onto the SEM was used to perform chemical analysis and elemental mapping of the components.

4.4.3 Transmission Electron Microscopy (TEM)

For TEM analysis, a Hitachi H-9500 high resolution transmission electron microscope was used and operated at 300 kV. A fitted goniometer-tilt stage was included, as well as a digital imaging camera and an EDAX-EDS elemental (X-Ray) mapping analysis attachment (EDAX r-TEMTM detector). The 3mm discs were electropolished using a Struers Tenupol-5 dual-jet system operating at a temperature of -30°C and voltage of 15V in an electrolytic solution containing 950 mL of methanol and 50 mL of perchloric acid. Both bright-field and dark-field images were taken.

4.5 X-RAY DIFFRACTION

A Brucker AXS-D8 (Discover) X-Ray Diffraction system was used to examine all EBM fabricated components, solid and open-cellular, as well as the precursor powder used in this study. This is used to determine the phases and chemical composition present in the material, as well as the crystal structure and preferred orientation.

4.6 HARDNESS

Microindentation (Vickers) hardness (HV) measurements were taken for the mounted, polished and etched powder, solid, and foam EBM fabricated components. Measurements were taken in both the horizontal and vertical planes of the solid and foam components. A Vickers diamond indenter was used to measure the hardness in a Struers-Doramin A-300 digital instrumental system applying a 100 gf (1N) load with a dwell time of 10s. Macroindentation hardness testing was also performed on the solid components, both vertical and horizontal planes, utilizing a Rockwell tester with a C-scale indenter (HRC) and a load of 1.5 kN. A minimum of 10 measurements were taken for both testing methods for each specimen.

4.7 DYNAMIC STIFFNESS

An IMCE-HTVP-1750-C resonant frequency (fr) analyzer was used to measure the dynamic stiffness (or Young's modulus, E) for the open-cellular blended TiAl EBM components, where $E \propto fr^2$ (Hernandez, *et al.*, 2012b). In order to satisfy the requirements for metal foams and obtain these results, 2.5x2.5x5 cm rectangular specimens were designed and produced by EBM.

4.8 THERMAL POST-PROCESSING TREATMENT

The 2-phase TiAl EBM solid, fully dense components were thermally processed using two different schedules. One sample was annealed at a temperature of 1150°C for 5 hours in purified argon (and furnace cooled) and another sample at a temperature of 1380°C for 1 hour in argon (furnace cooled). The purpose of “annealing” treatments is to alter the microstructure and achieve improved mechanical properties, such as increased hardness and improved ductility, creep resistance, and fracture toughness.

CHAPTER 5: RESULTS

5.1 MICROSTRUCTURES FOR TWO-PHASE GAMMA TITANIUM ALUMINIDE FABRICATED BY ELECTRON BEAM MELTING

In this study we examined the microstructures in fully dense γ (TiAl) components fabricated by additive manufacturing (AM) using electron beam melting (EBM) of pre-alloyed, atomized powder using light optical metallography (LOM) and transmission electron microscopy (TEM). Preliminary open-cellular (foam) components were also fabricated for a range of densities (ρ), and the foam-ligament microstructures also observed by LOM.

5.1.1 As-Fabricated EBM Components

Figures 5.1.1 and 5.1.2 illustrate the powder microstructure to be an equiaxed, microdendritic (cellular) grain structure ($\sim 2 \mu\text{m}$) exhibiting a duplex α_2/γ crystal structure ($\alpha_2/\gamma = 0.5$) as illustrated in the XRD spectra of Figure 5.1.3. In comparison, Figures 5.1.4 and 5.1.5 show 3D composite LOM views of the solid, rectangular and cylindrical EBM component (Figure 4.1.1) microstructures to consist of a duplex (α_2/γ), equiaxed grain structure ($\sim 15 \mu\text{m}$ grain size) composed of colony-lamellar substructures; primarily γ (TiAl). The measured density for the solid components averaged 3.85 g/cm^3 . XRD spectra corresponding to the horizontal and vertical reference plane section for Figures 5.1.4 and 5.1.5 are shown in Figures 5.1.6 and 5.1.7, respectively, where $\alpha_2/\gamma \cong 0.05$. Figure 5.1.8 shows an LOM (lower magnification) view of the vertical plane section corresponding to Figure 5.1.5 (cylindrical component) illustrating etching contrast delineating successive layering, representative of layer thicknesses of $\sim 100 \mu\text{m}$.

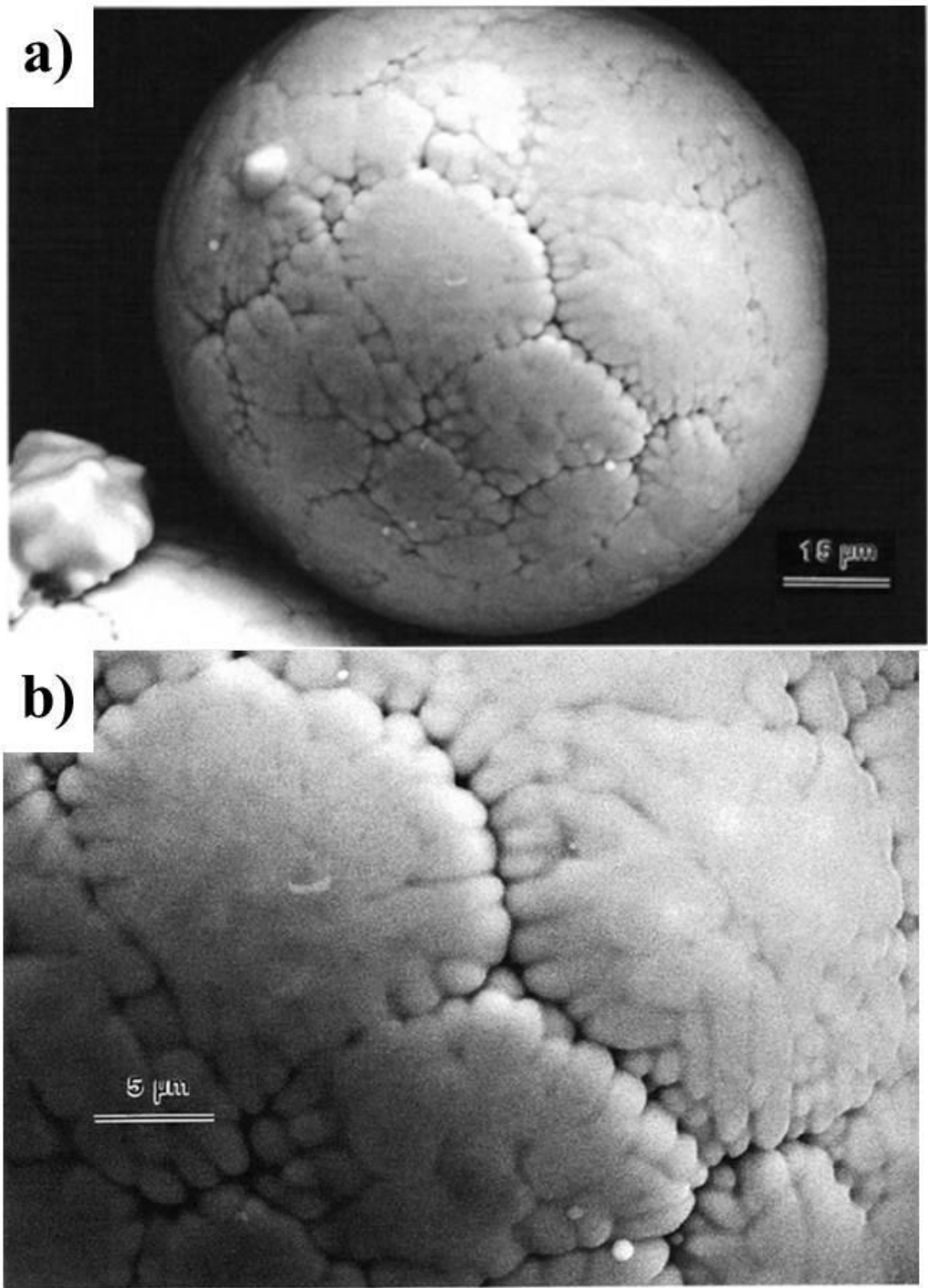


Figure 5.1.1: Magnified views for the precursor Ti-48Al-2Cr-2Nb powder in Figure 4.1.2.

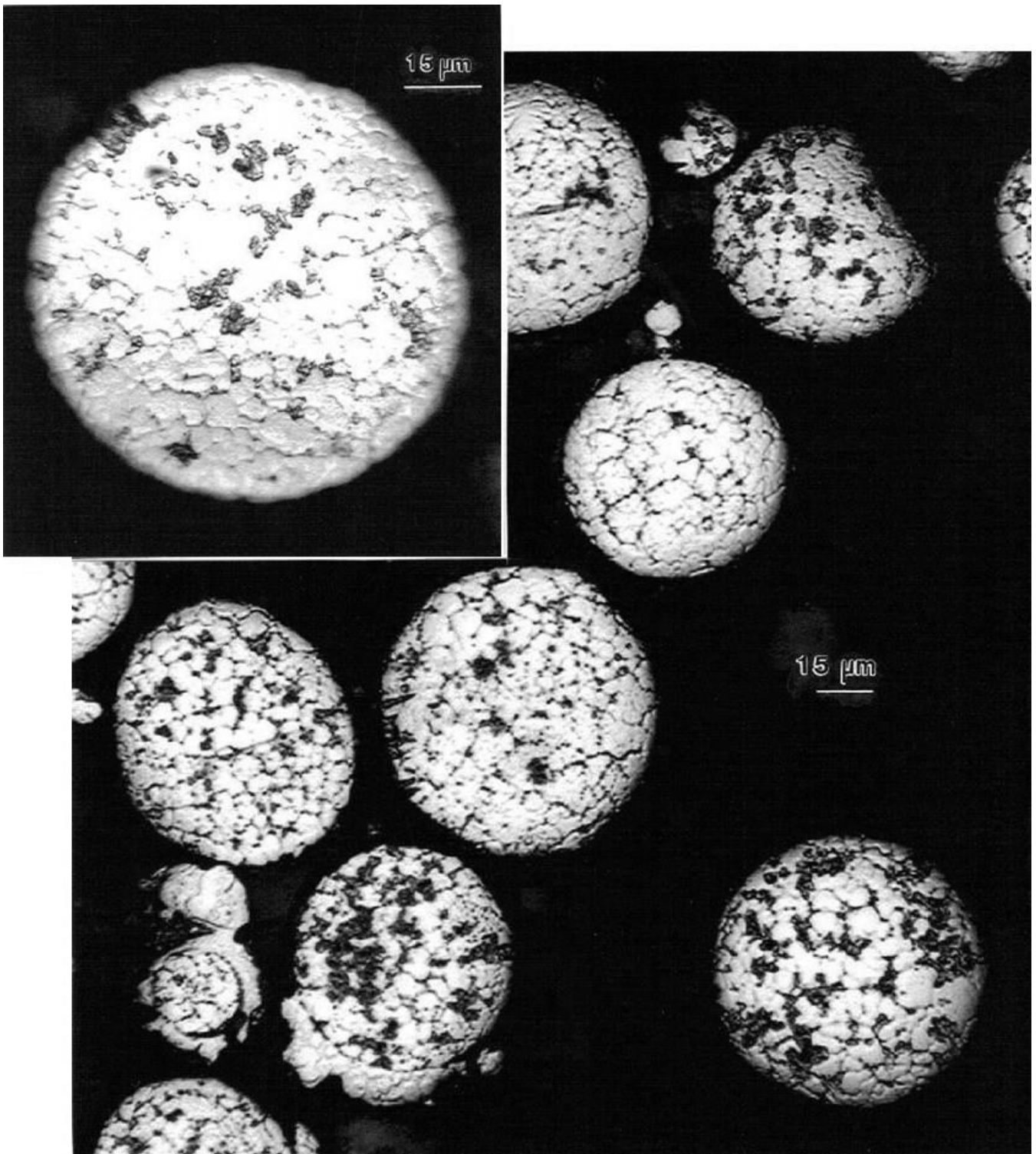


Figure 5.1.2: LOM section views showing internal, equiaxed, dendritic grain structure ($\sim 2 \mu\text{m}$) of the pre-alloyed powder.

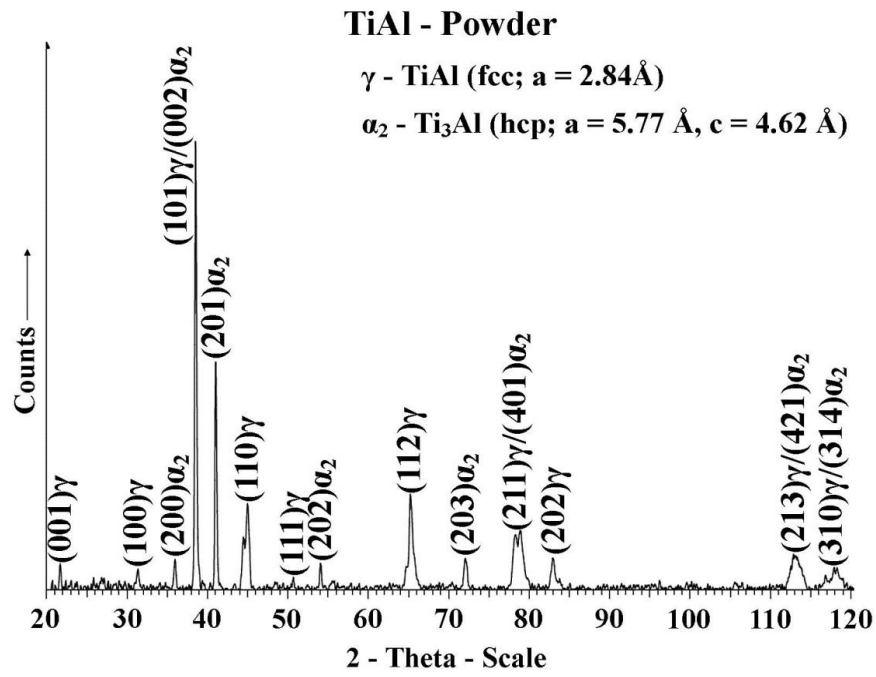


Figure 5.1.3: XRD spectra for the Ti-48Al-2Cr-2Nb precursor powder in Figure 4.1.2(a).

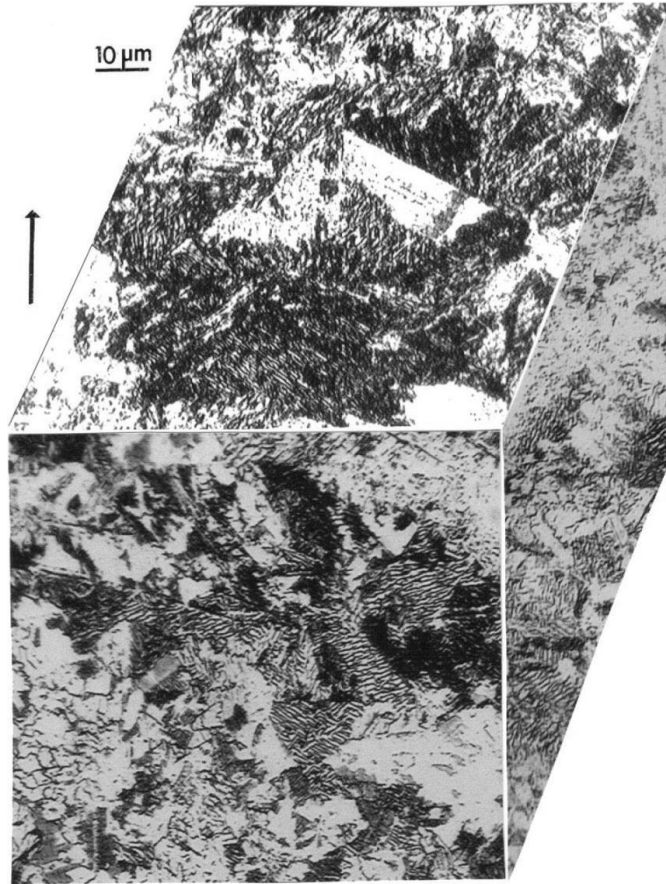


Figure 5.1.4: 3D-LOM composite view for dual-phase γ -TiAl microstructure representative of the EBM fabricated rectangular solid (Figure 4.1.1). Build direction is indicated by arrow (left).



Figure 5.1.5: 3D-LOM composite view for dual-phase γ -TiAl microstructure representative of the EBM fabricated cylindrical solid (Figure 4.1.1). Build direction is indicated by arrow (left).

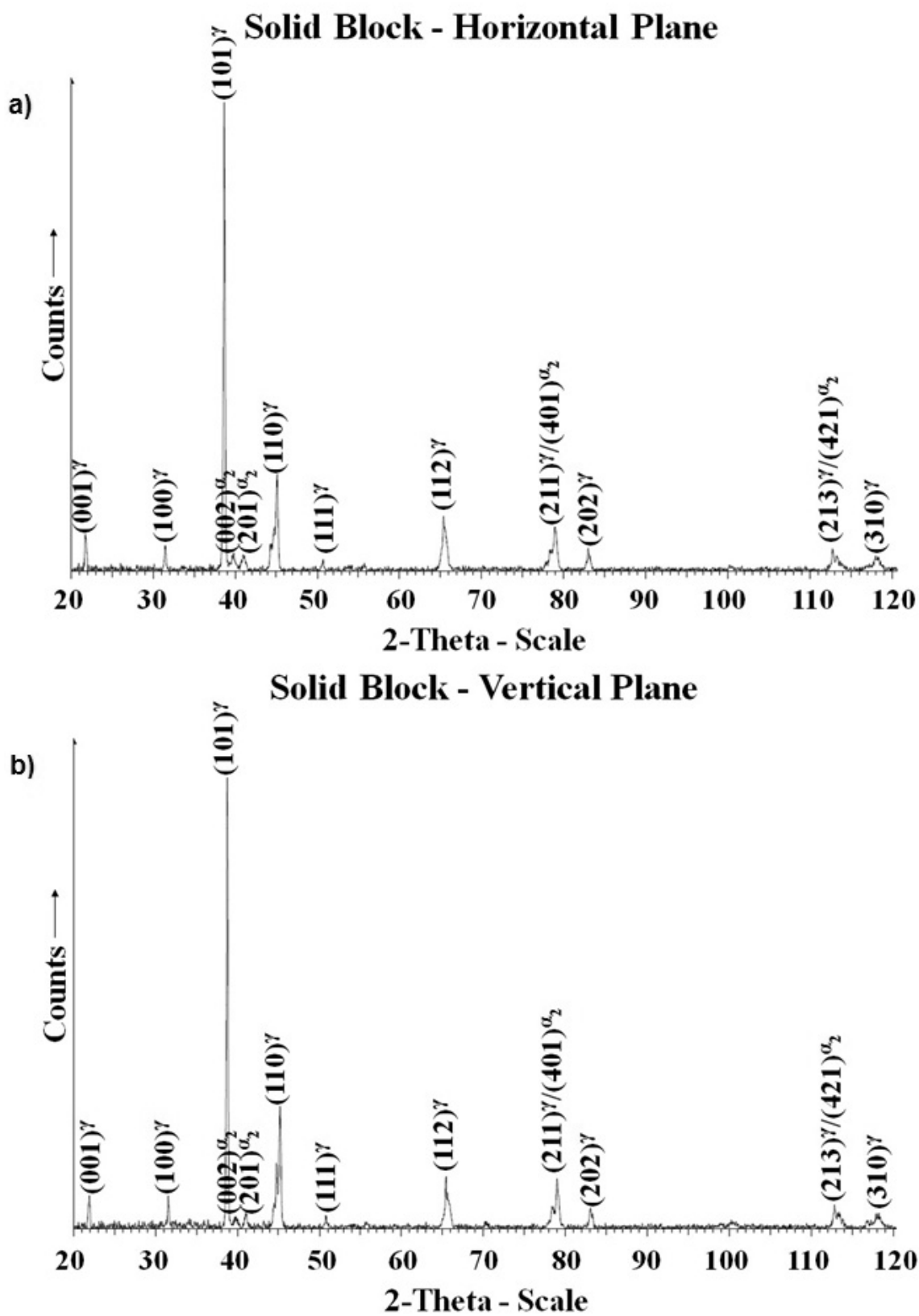


Figure 5.1.6: XRD spectra corresponding to the horizontal (a) and vertical (b) reference planes for a rectangular EBM-fabricated block (represented by Figure 5.1.4).

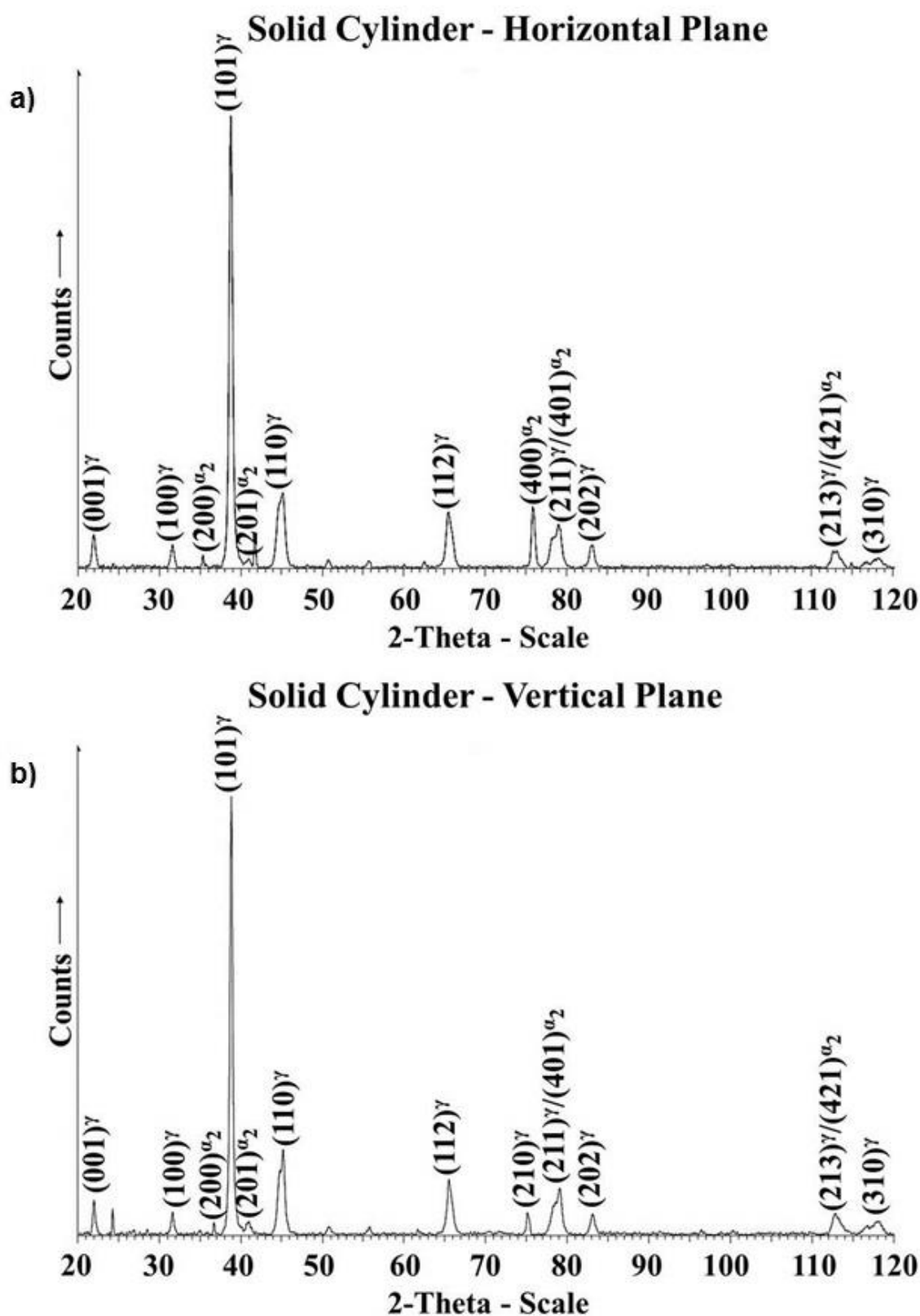


Figure 5.1.7: XRD spectra corresponding to the horizontal (a) and vertical (b) reference planes for a cylindrical EBM-fabricated component (represented by Figure 5.1.5).

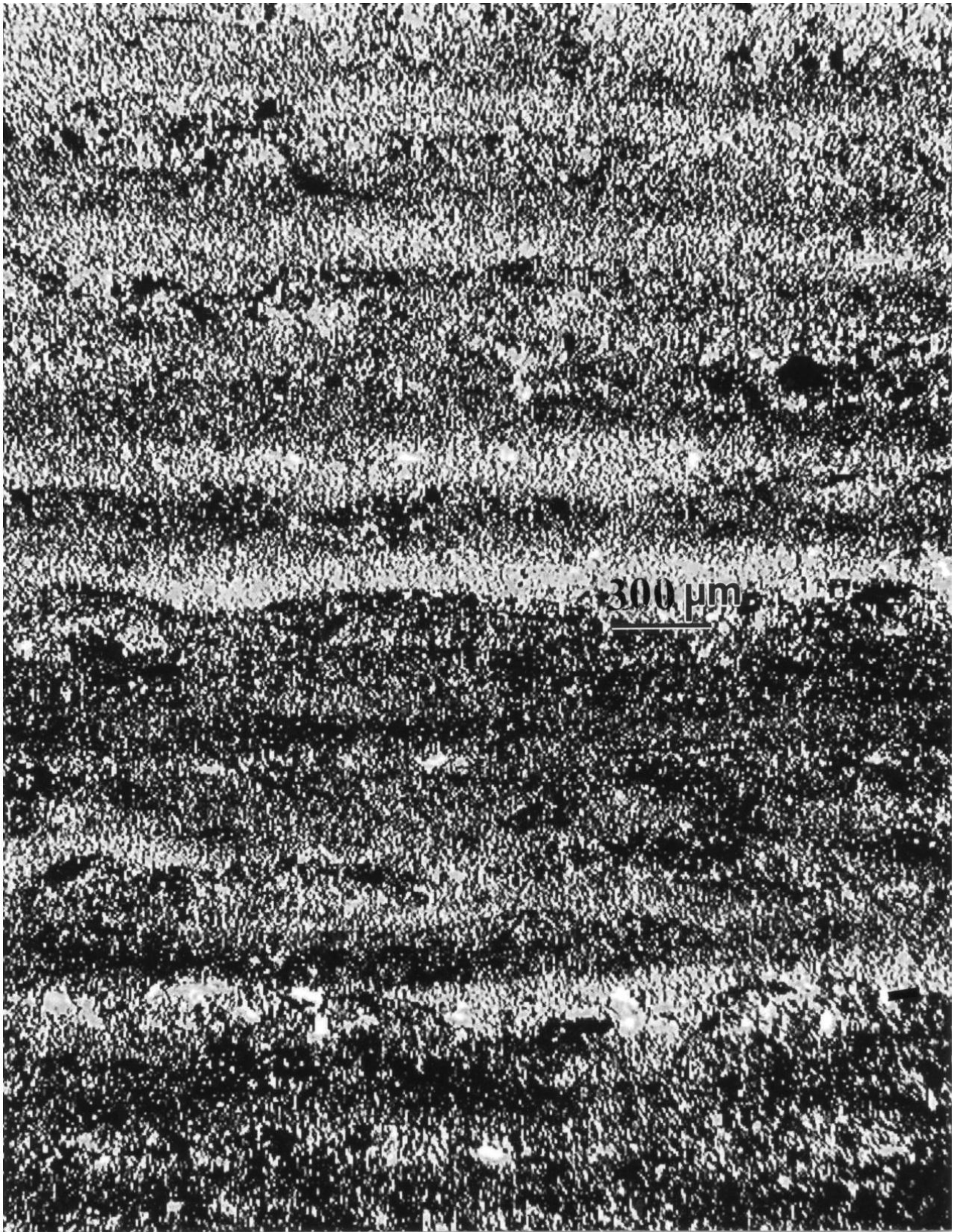


Figure 5.1.8: Low-magnification LOM image showing additive-layer structures in the vertical reference plane for a cylindrical EBM-fabricated component (represented by Figure 5.1.5).

Figure 5.1.9 shows foam prototype components representing a range of densities, indicated. The SEM view in Figure 5.1.10, typical for the ligaments, shows the partially melted/sintered powder particles characterizing the surface structure. Figure 5.1.11 shows a typical LOM view of the ligament microstructure which corresponds to those shown in Figures 5.1.4 and 5.1.5 for the solid components: exhibiting a generally equiaxed duplex grain structure $\sim 15\mu\text{m}$ grain diameter. The XRD spectra characteristic of the foam - ligaments is shown in Figure 5.1.12. In contrast to the corresponding, solid component XRD spectra shown in Figures 5.1.6 and 5.1.7, the foam exhibits slightly less α_2 ($\alpha_2/\gamma \leq 0.05$).

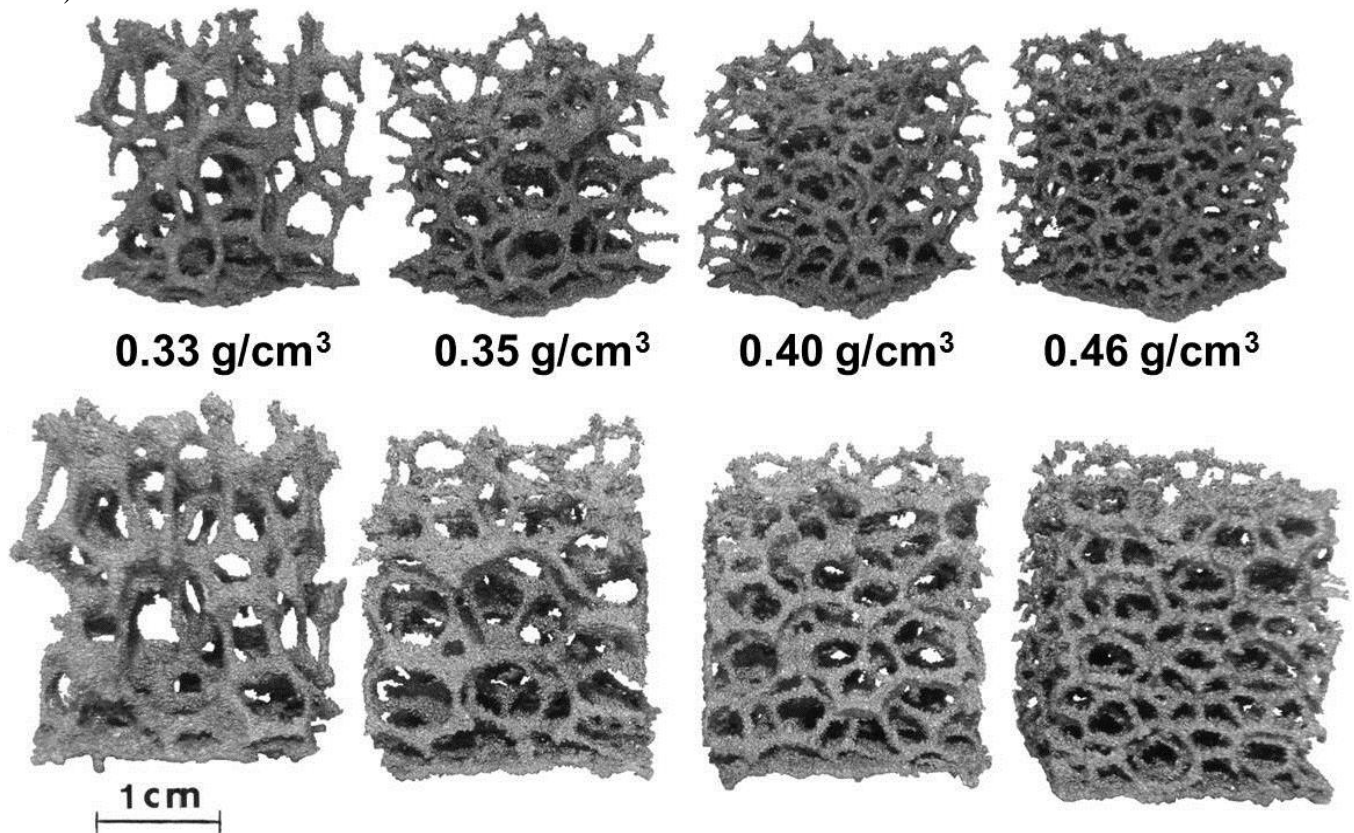


Figure 5.1.9: Ti-48Al-2Cr-2Nb foam prototypes fabricated by EBM. Top row shows edge orientations while bottom row shows face orientations at slight larger magnifications. Measured densities are indicated.

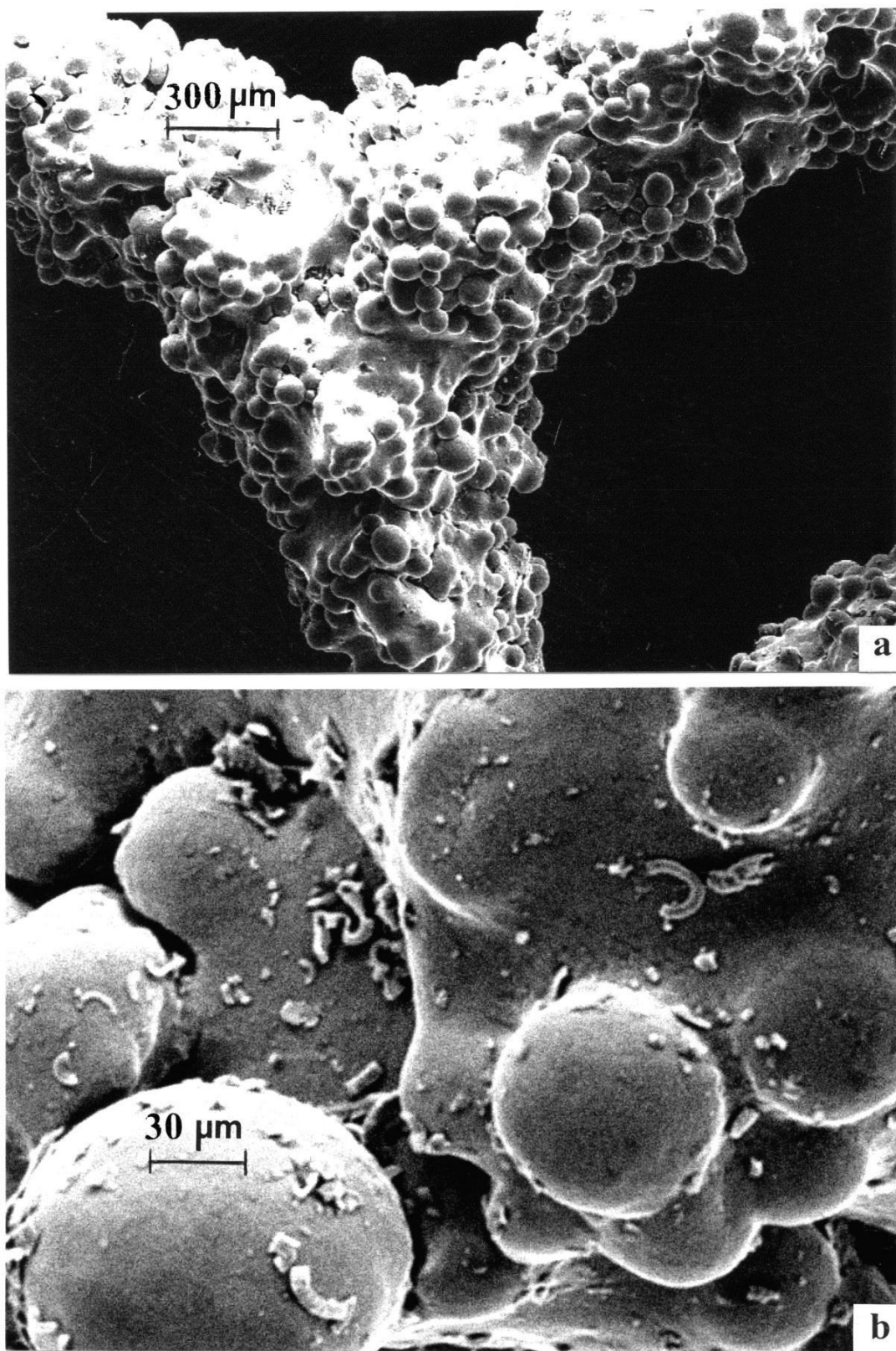


Figure 5.1.10: SEM views for ligament structure of foam sample ($\rho = 0.33 \text{ g/cm}^3$) showing partially sintered powder particles. (a) Low-magnification SEM image. (b) High-magnification view showing partially sintered powder particles.

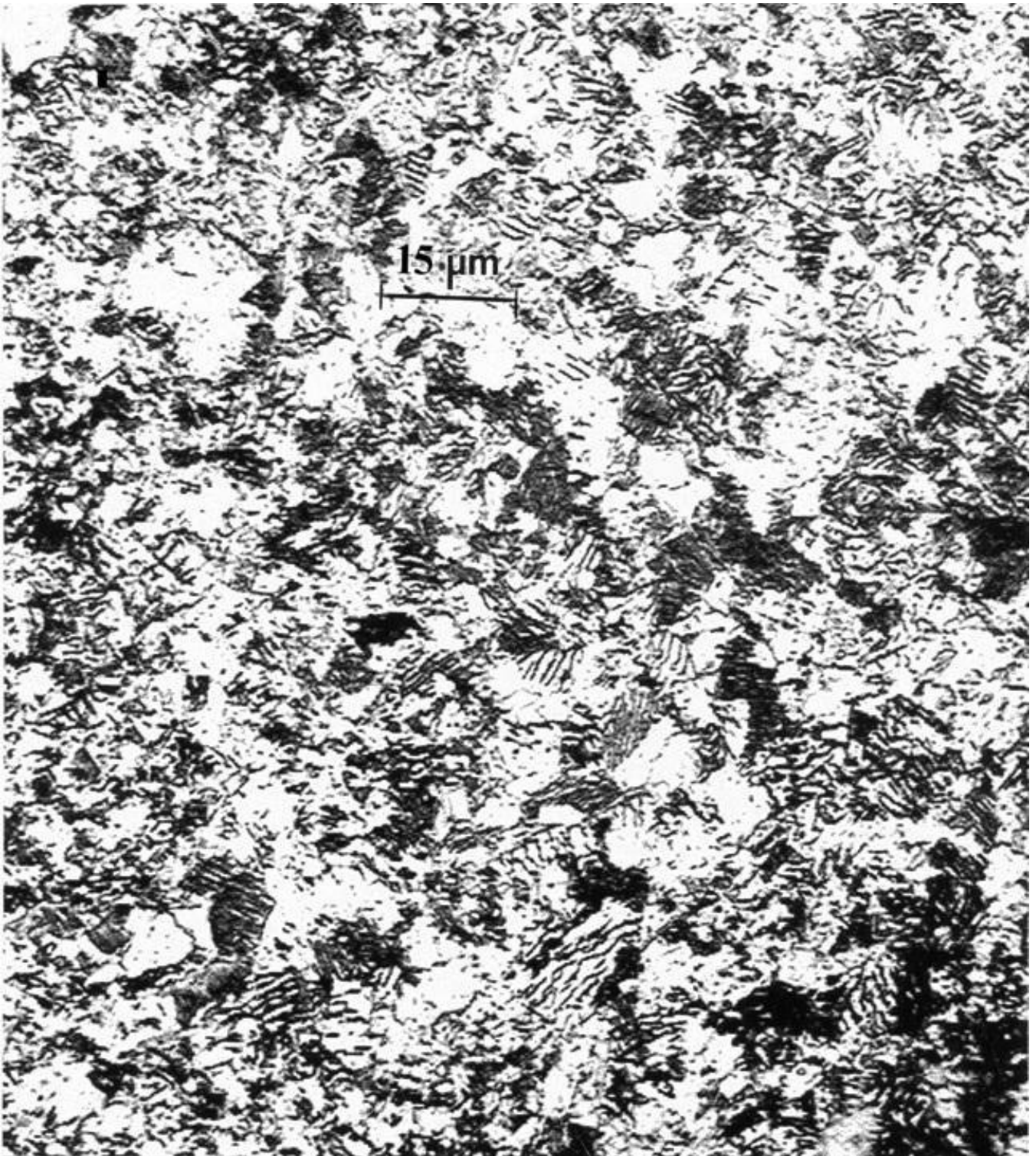


Figure 5.1.11: Foam ligament microstructure: OM image showing duplex (two-phase) structure.

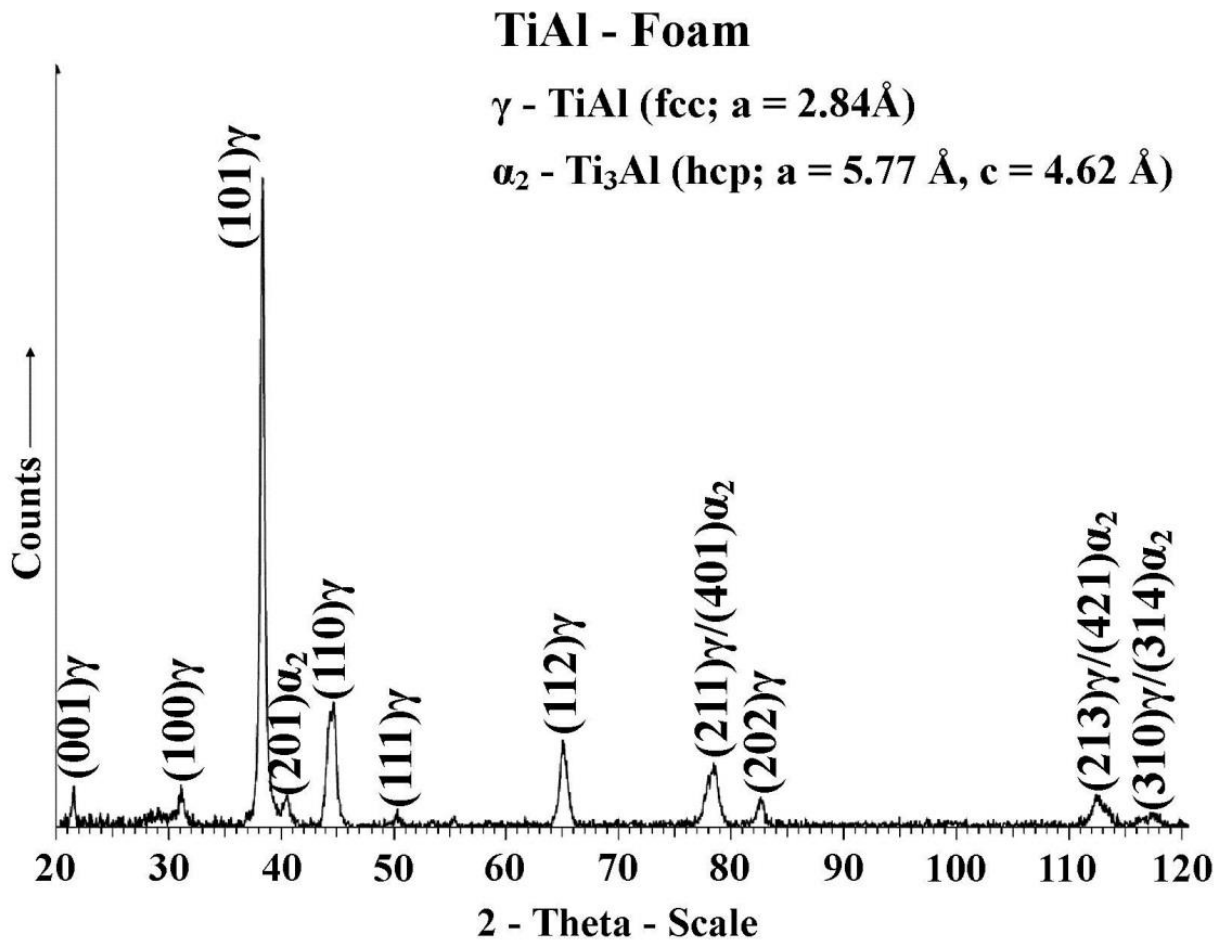


Figure 5.1.12: XRD spectra for the foam components.

Figure 5.1.13 compares typical horizontal and vertical reference plane TEM images characterizing microstructures illustrated in the LOM-3D composition in Figure 5.1.4. These images show relatively equiaxed γ (TiAl) grains with and without α_2/γ lamellar microstructures. Figures 5.1.14 to 5.1.16 show the details of the lamellar α_2/γ microstructures in the horizontal reference plane of a rectangular (block) component (Figure 4.1.1) specimen. Figure 5.1.14 shows a large, lamellar-containing grain separated from smaller, generally equiaxed γ (TiAl) grains. Figure 5.1.15 shows the details of the thin α_2 (hcp) coincident plates $(11\bar{1})_\gamma \parallel (0001)\alpha_2$ which are perpendicular to the (123) fcc (γ (TiAl)) surface orientation as indicated in the selected-area electron diffraction (SAED) pattern insert showing γ (TiAl) and α_2 - Ti_3Al diffraction spots along $[11\bar{1}]_\gamma$ (arrow in Figure 5.1.15 SAED pattern insert); perpendicular to the $(11\bar{1})$ plane which is perpendicular to the (123) surface plane or indicated previously. These α_2 platelets are roughly only 20 nm thick, while in some cases both the α_2 and γ

regions have similar thicknesses as illustrated in the bright-field/dark field TEM sequence shown in Figure 5.1.16 (a) and (b), respectively where only small γ (TiAl) platelets reverse contrast in dark-field (Figure 5.1.16(b)).

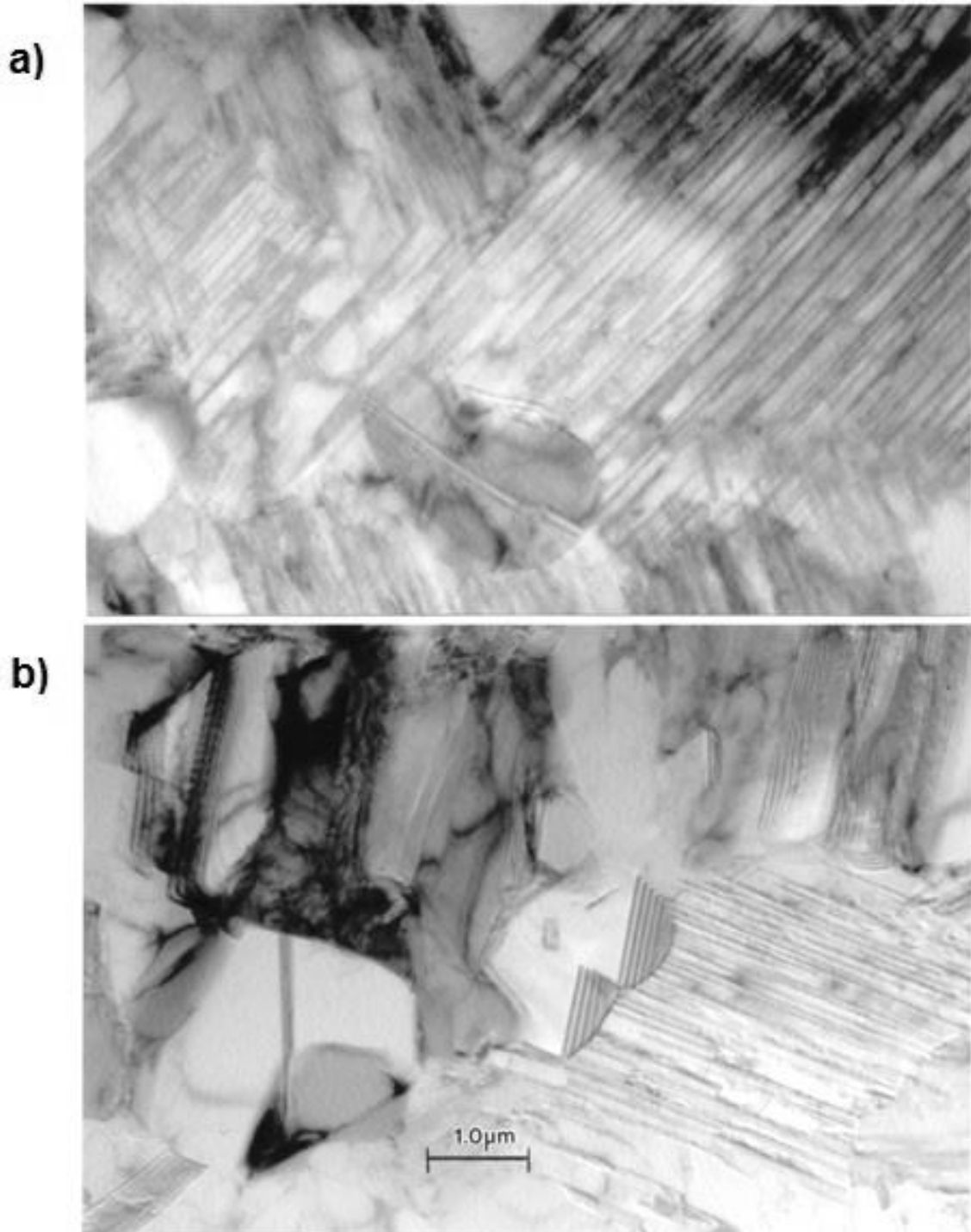


Figure 5.1.13: Comparative TEM images for two-phase microstructures in EBM-fabricated γ -TiAl cylindrical component. (a) Horizontal reference plane. (b) Vertical reference plane (Figure 5.1.4)

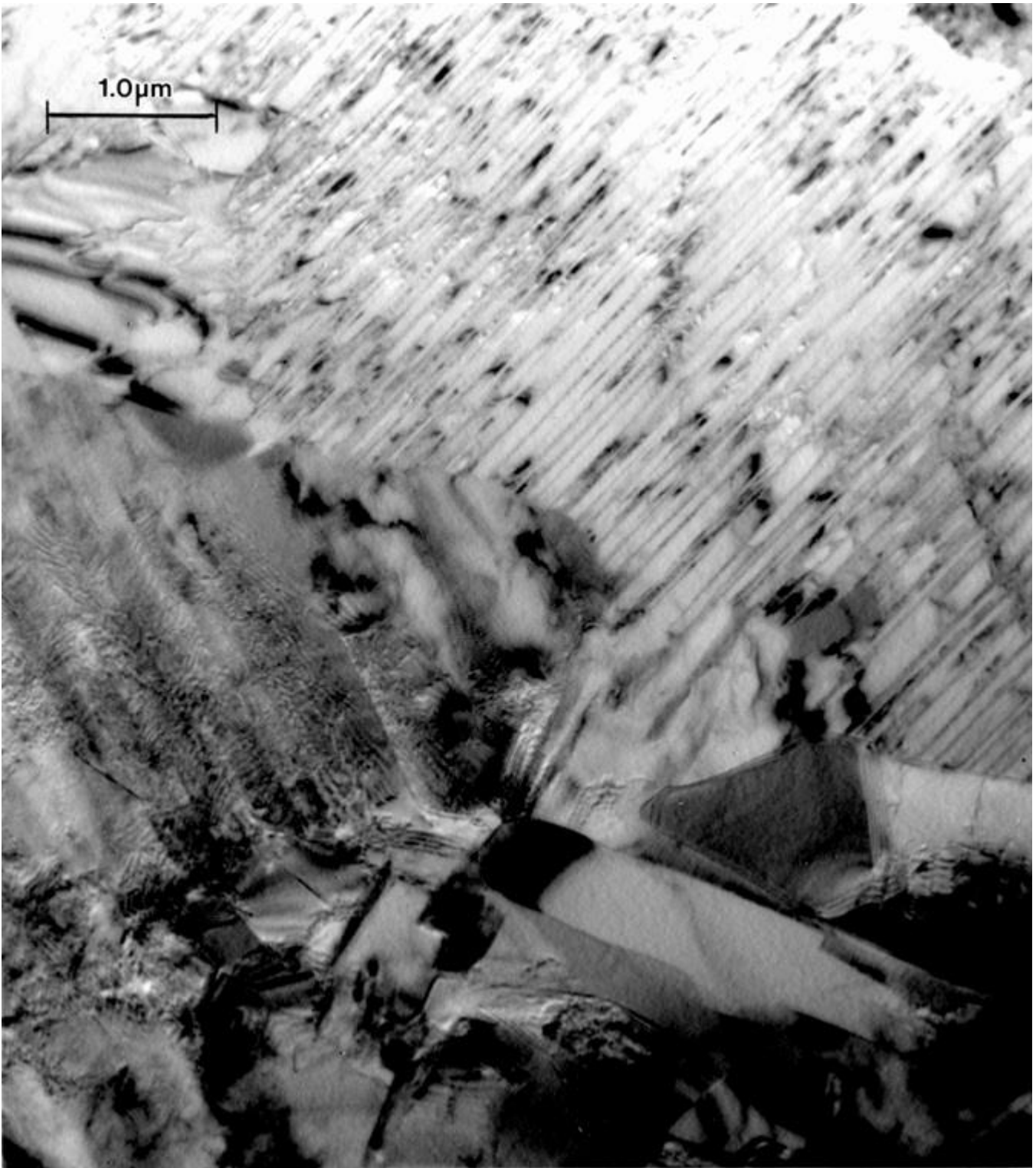


Figure 5.1.14: TEM bright-field image showing lamellar (α_2/γ) filled grain (top) and primarily γ -TiAl grains (bottom).

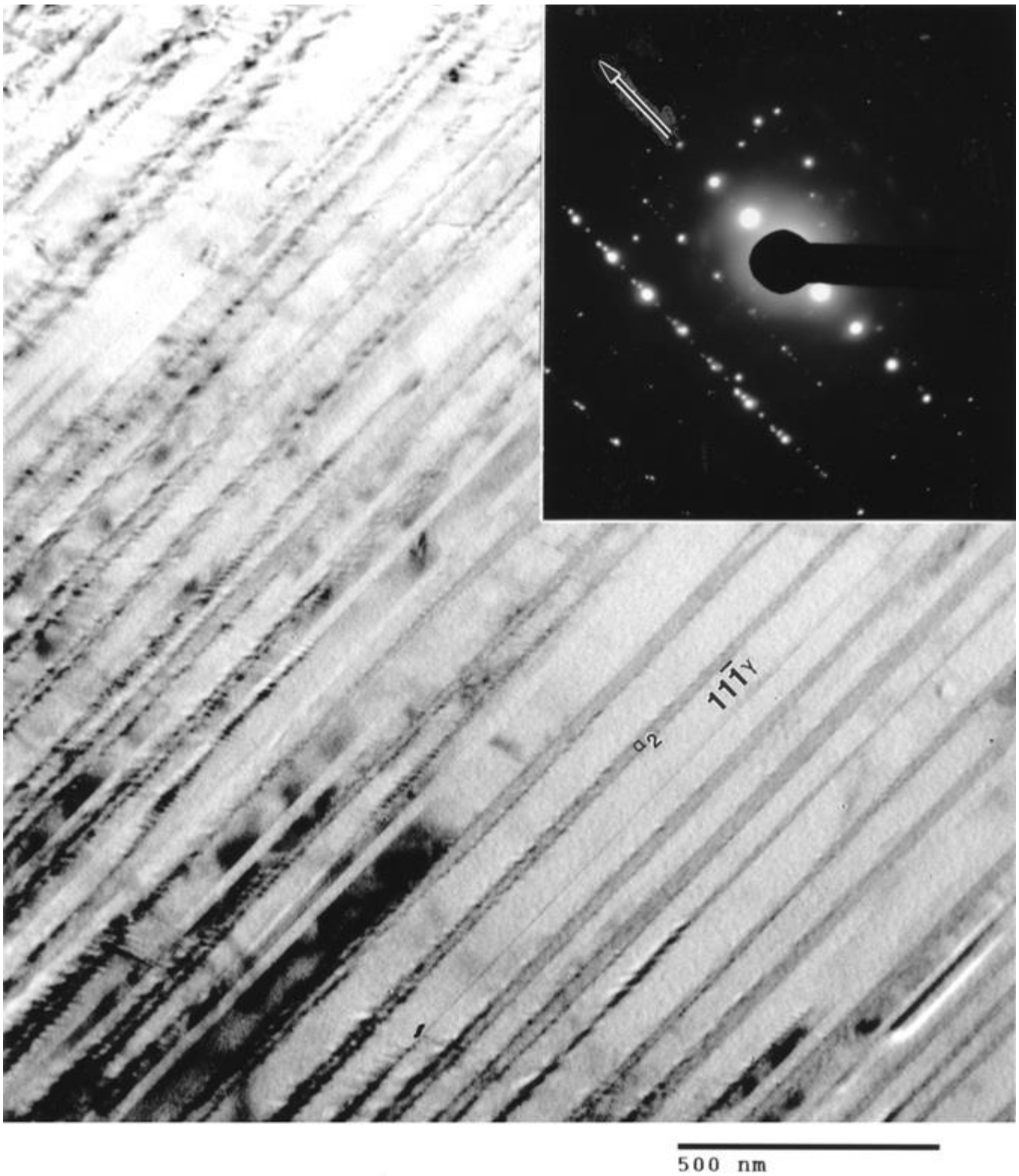


Figure 5.1.15: Magnified TEM bright-field image showing thin α_2 -Ti₃Al plates in γ -TiAl. The SAED pattern inset shows rows of γ and α_2 diffraction spots. These rows are in the $[11\bar{1}]_\gamma$ direction (arrow). The grain surface orientation is (123).

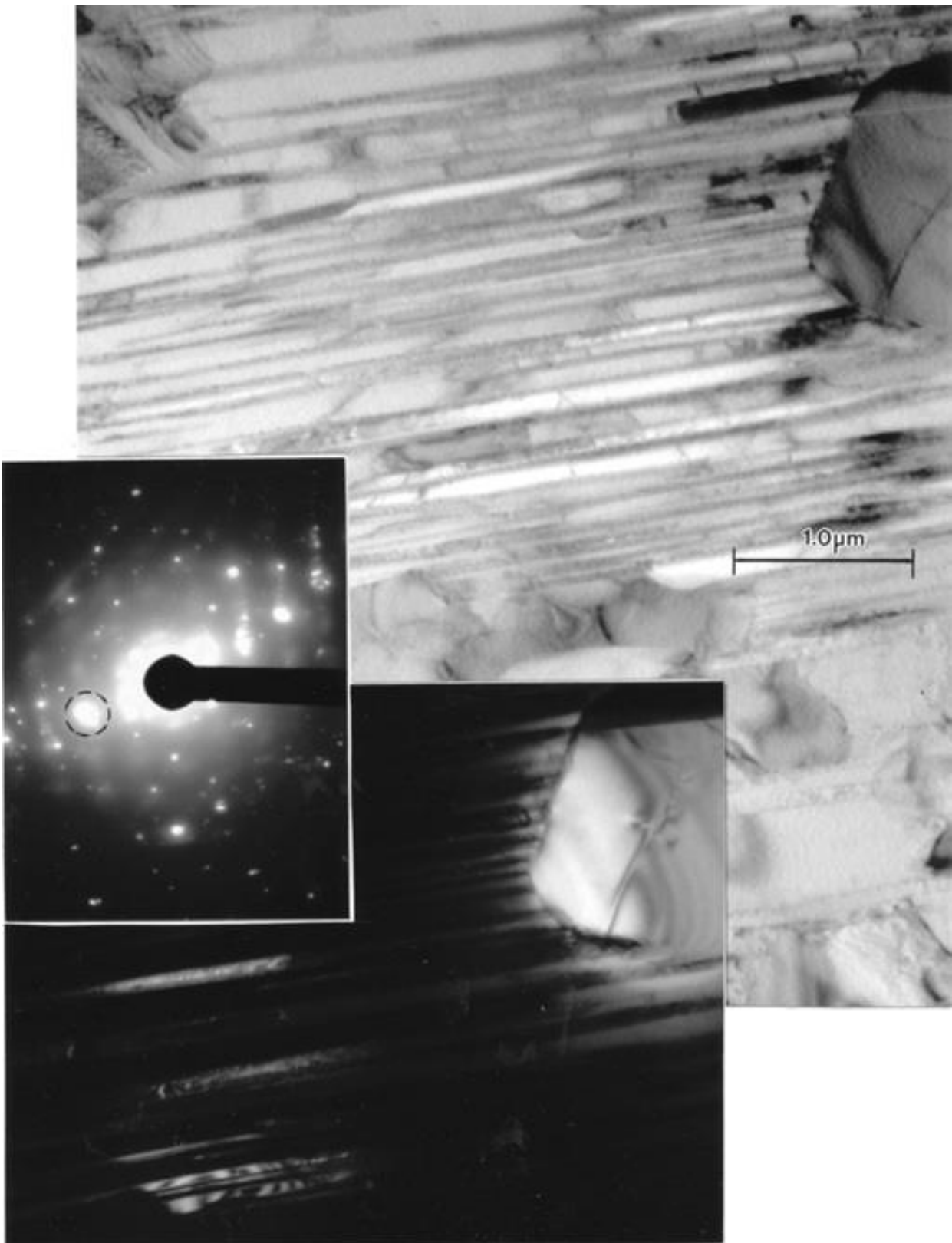


Figure 5.1.16: TEM bright-field (a) dark-field (b) sequence for α_2/γ lamellar microstructure. The DF image in (b) utilized the apertured γ diffraction spot shown circled in the SAED pattern inset. Only small fraction of the γ -phase regions are imaged.

While the solid, cylindrical EBM components (Figure 4.1.1) exhibited microstructures essentially the same as those shown for comparison in Figures 5.1.4 and 5.1.5, and the TEM images illustrated in Figures 5.1.13 - 5.1.16, the TEM images shown in Figures 5.1.17 to 5.1.20 illustrate similar and related microstructures which characterize the solid components overall. Figure 5.1.17 shows a horizontal section view for a cylindrical sample containing some α_2 platelets within the γ (TiAl) as well as a relatively high density of dislocation structures. Correspondingly, Figure 5.1.18 illustrates a large array of dislocation dipoles in a similar specimen section. There are strain contrast regions along α_2/γ interfaces to the left in Figure 5.1.18 (arrow). These may be ledge structures illustrated in previous work of Appel, *et al.* (2000). Figure 5.1.19 shows a γ (TiAl) grain containing thin α_2 platelets having the same orientation/crystallographic relationships noted for Figure 5.1.15. The arrow in Figure 5.1.19 is identical to the arrow in the SAED pattern insert in Figure 5.1.15, and represents the $[11\bar{1}]$ direction characterizing the arrays of diffraction spots in the SAED pattern insert in Figure 5.1.19. Figure 5.1.20, in contrast to Figure 5.1.16, illustrates a bright-field/dark-field sequence showing contrast reversal for large segments of α_2 platelets, utilizing the operating reflection shown circled in the SAED pattern insert in Figure 5.1.20.

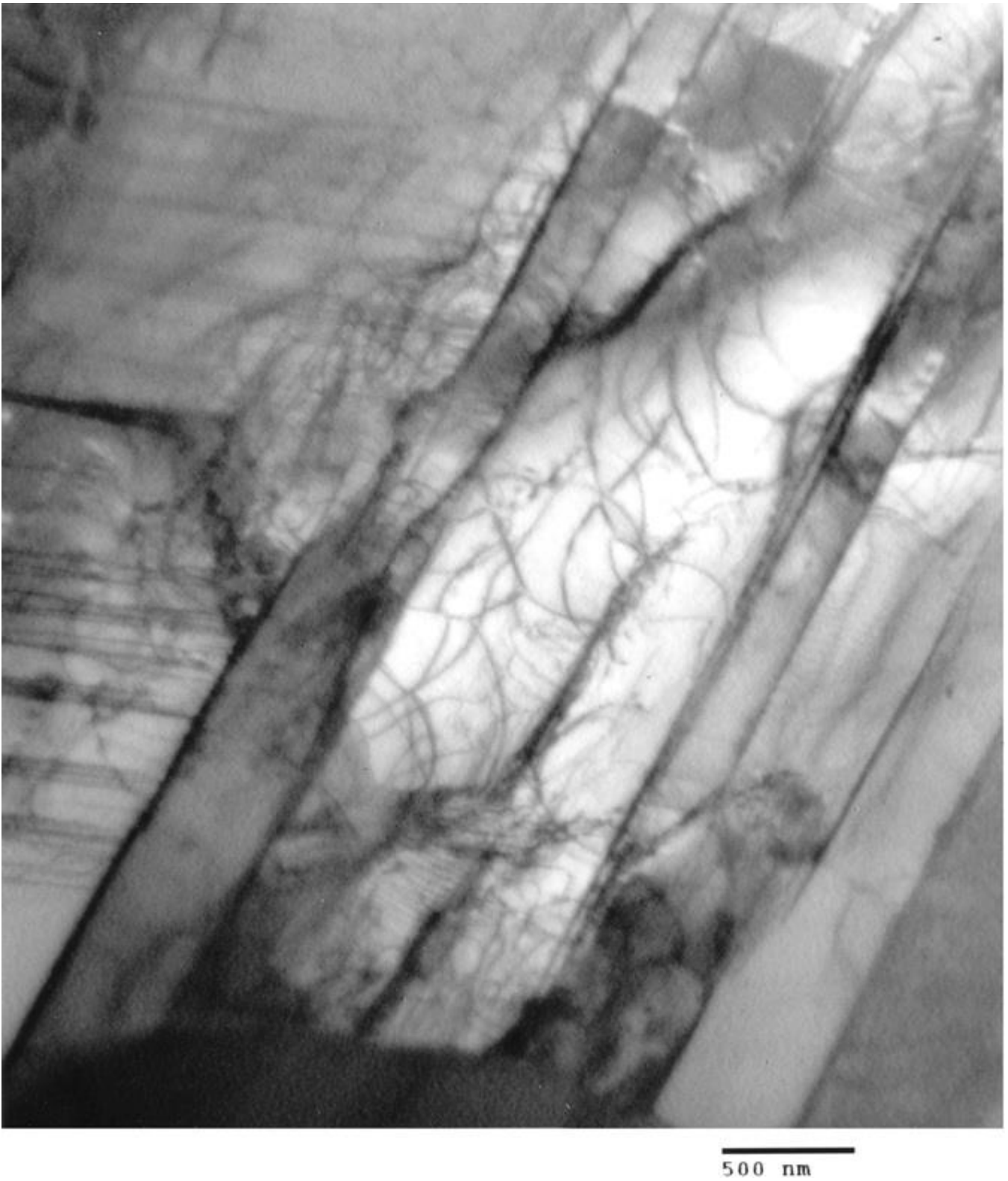


Figure 5.1.17: TEM bright-field image for dislocation and lamellar microstructures observed in the horizontal reference plane for an EBM-fabricated cylindrical component (Figure 4.1.1).

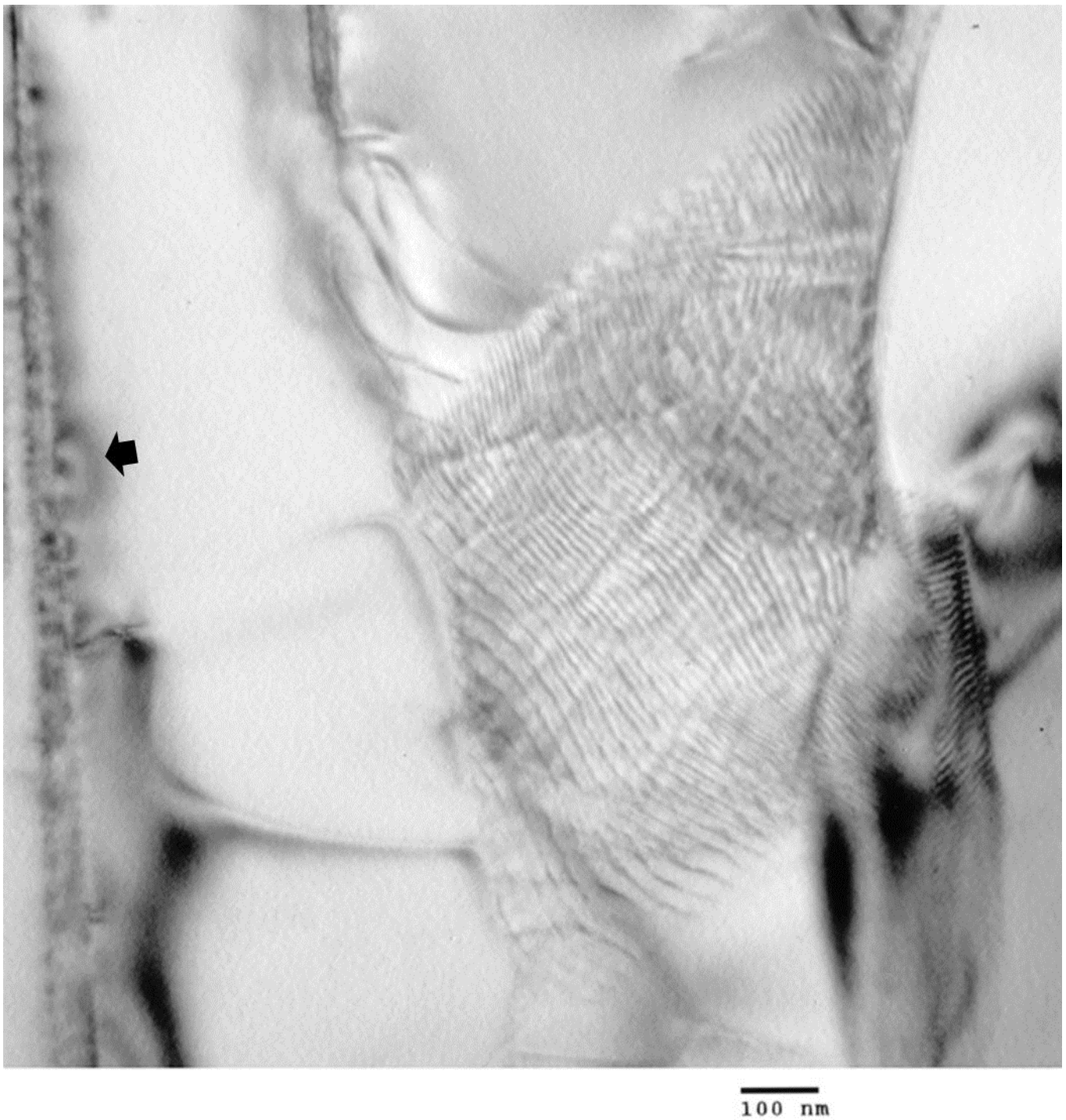


Figure 5.1.18: TEM image showing a large area composed of dislocation dipoles in a sample similar to Figure 5.1.17. The α_2 lamellae at the extreme left of the micrograph exhibit strain-field contrast features (arrow) which may arise from interfacial steps or ledges.

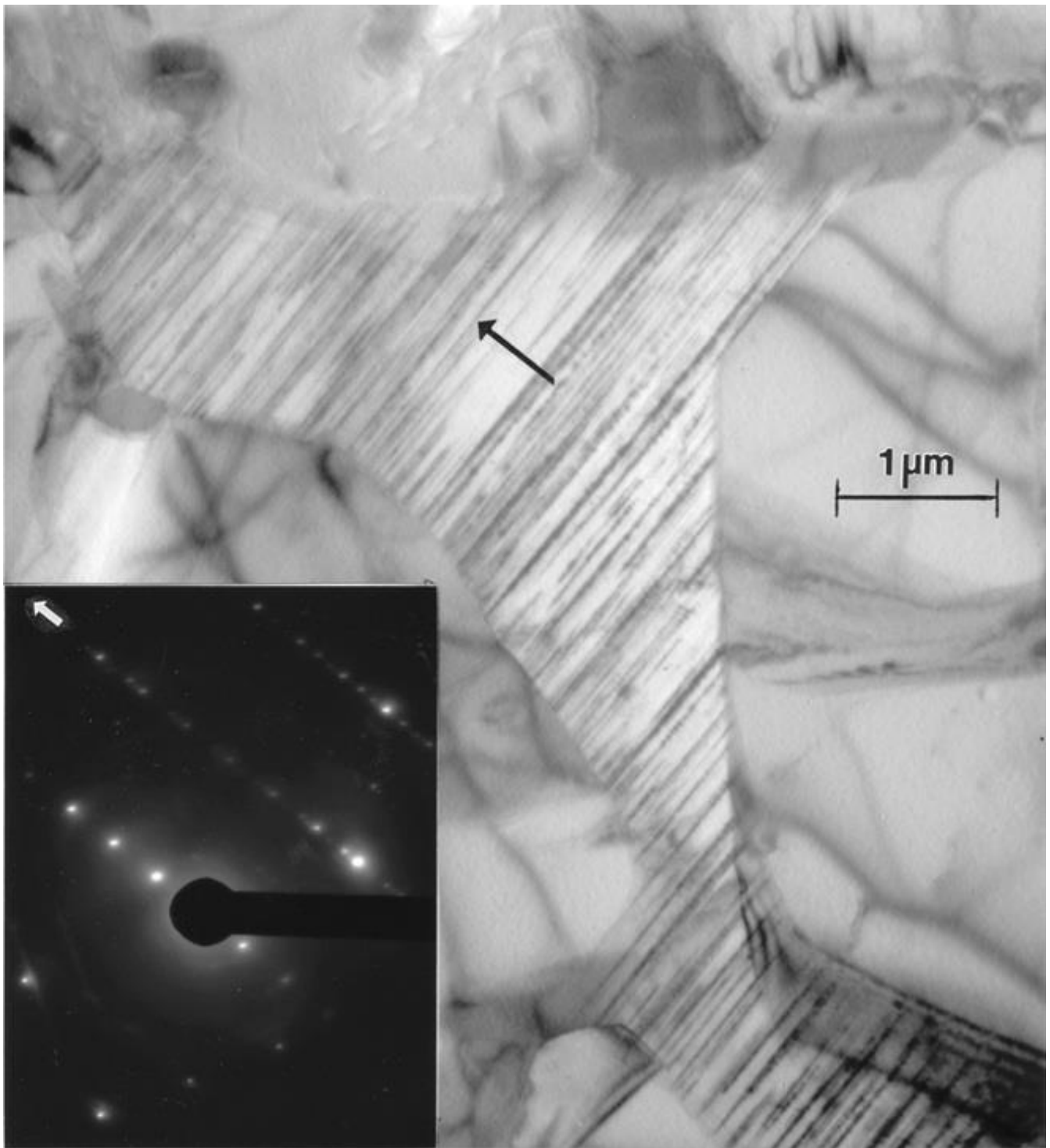


Figure 5.1.19: TEM showing lamellar microstructures in the vertical reference plane for an EBM-fabricated cylindrical component. The SAED pattern inset is the same as that in Figure 5.1.15. The arrow (black in the image and white in the SAED pattern) represent the $[11\bar{1}]_{\gamma}$ direction. The surface orientation is (123).

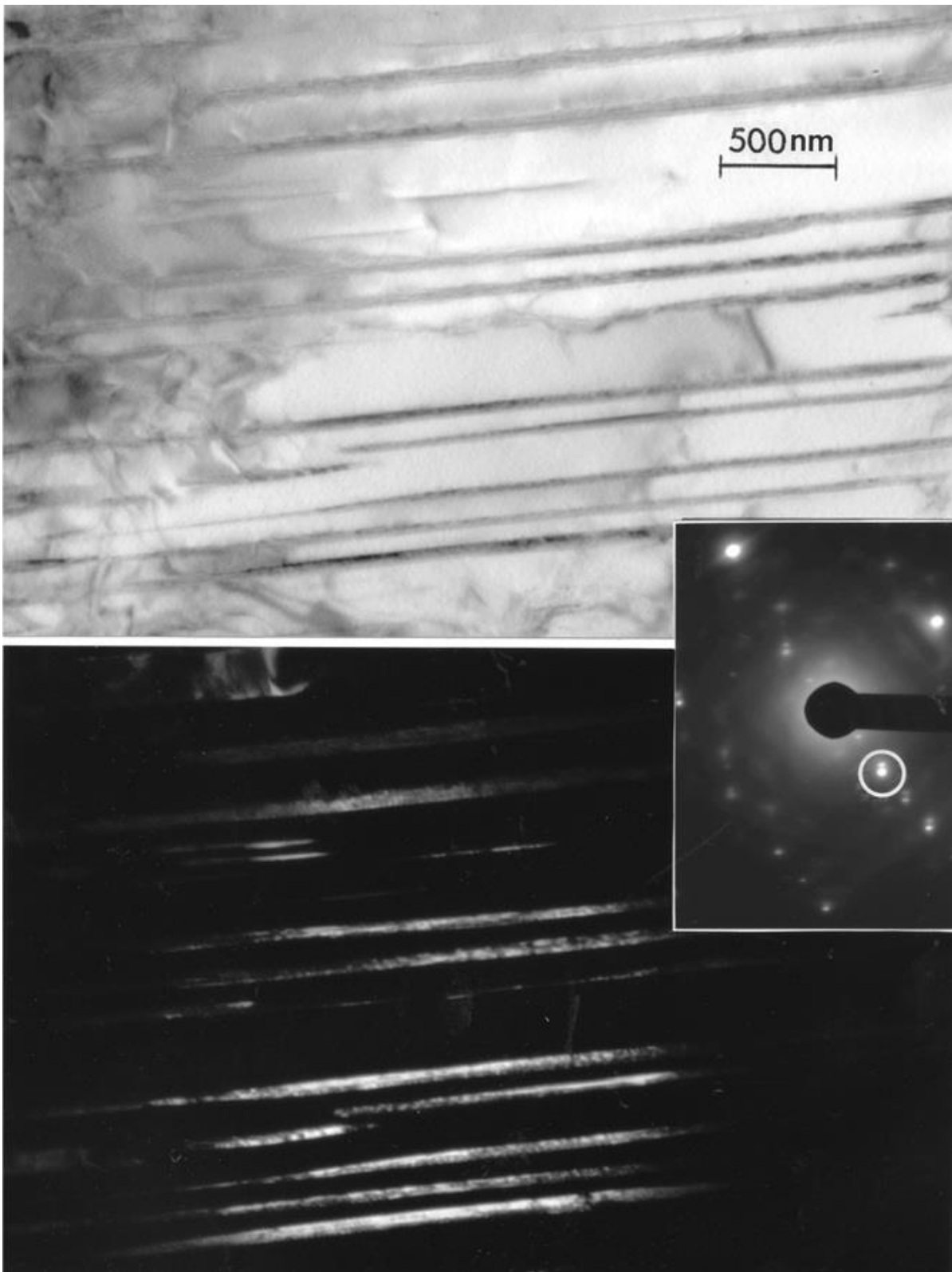


Figure 5.1.20: Bright-field (a) dark-field (b) TEM image sequence of α_2/γ lamellar microstructure in an EBM-fabricated cylindrical component (in the vertical reference plane). The DF image in (b) corresponds to the circled α_2 diffraction spot in the SAED pattern inset. The DF images in (b) represent portions of α_2 plates.

5.1.2 Thermal Post-Processing

In the conventional processing of titanium aluminides, including ingot metallurgy (Koeppel, *et al.*, 1993), investment casting (Kim, *et al.*, 1995) and powder metallurgy (Wagner, *et al.*, 1975), duplex microstructures following HIP (after investment casting) at temperatures around 1200°C appear similar to those shown in Figures 5.1.4 and 5.1.5 and Figure 5.1.11 for solid and foam components, respectively. Near γ (globular) microstructures consisting of very fine, equiaxed grains ($\sim 10\ \mu\text{m}$) have been observed after two-step isothermal forging at 1220°C, while fully-lamellar microstructure occurs with additional heat treatment at 1370°C/1h \rightarrow 900°C/6h \rightarrow 20°C which produces an equiaxed grain structure with average grain sizes $>300\ \mu\text{m}$ (Appel, *et al.*, 2000). The duplex microstructure yields the highest elongation ($\sim 2\%$) with poor toughness (Appel, *et al.*, 1998 and London, *et al.*, 1993), while the fully lamellar grain structures exhibit improved creep strength and fracture toughness, with reduced elongation in contrast to the fine-grain, duplex structures (Appel, *et al.*, 1998 and Kim, *et al.*, 1994).

In this research program, we emulated these contemporary microstructures by annealing the EBM-fabricated, rectangular block specimens shown in Figure 4.1.1 using two schedules: 1.) specimens were annealed at 1150°C for 5h in purified argon (and furnace cooled); 2.) specimens were annealed at 1380°C for 1h in argon (and furnace cooled). For schedule 1.), a single-step annealing process, equiaxed fine grains ($\sim 3\ \mu\text{m}$) occurred with some remanent larger-grain, occluded clusters. For schedule 2.) or anneal 2.), a large equiaxed, fully lamellar grain structure was observed having an average grain size of $550\ \mu\text{m}$. Figure 5.1.21 compares these two anneal schedule microstructures observed by LOM. Figure 5.1.22 shows some examples of the Anneal 1.) microstructures/substructures observed in the TEM, where in contrast to the TEM images shown in Figures 5.1.13 and 5.1.14 for the EBM-fabricated, solid block specimens, there is no corresponding lamellar microstructure, and irregular α_2 platelets are intermixed with γ -TiAl $\{111\}$ twins. This is particularly notable in Figure 5.1.22(b) which shows a slightly magnified (123)-oriented grain with $(\bar{1}\bar{1}1)$ and $(1\bar{1}1)$ coincident lamellae. Correspondingly, Figure 5.1.23 shows a bright-field/dark-field TEM sequence showing thin, γ -TiAl $(11\bar{1})$ twins intermixed with thin lamellar α_2 (Ti_3Al). The SAED pattern insert shows the $[11\bar{1}]$ direction (arrow) normal to the $(11\bar{1})$ planes which are correspondingly normal to the (123) grain surface. These orientation and crystallographic features emulate those shown previously in Figures 5.1.15 and 5.1.16.

In contrast to the EBM-fabricated block and cylindrical solids, the annealed microstructures shown in Figures 5.1.21 to 5.1.23 exhibit somewhat limited α_2 (Ti_3Al) coincident phase. This is particularly evident on comparing the SAED patterns in Figures 5.1.15 and 5.1.16 with Figure 5.1.23.

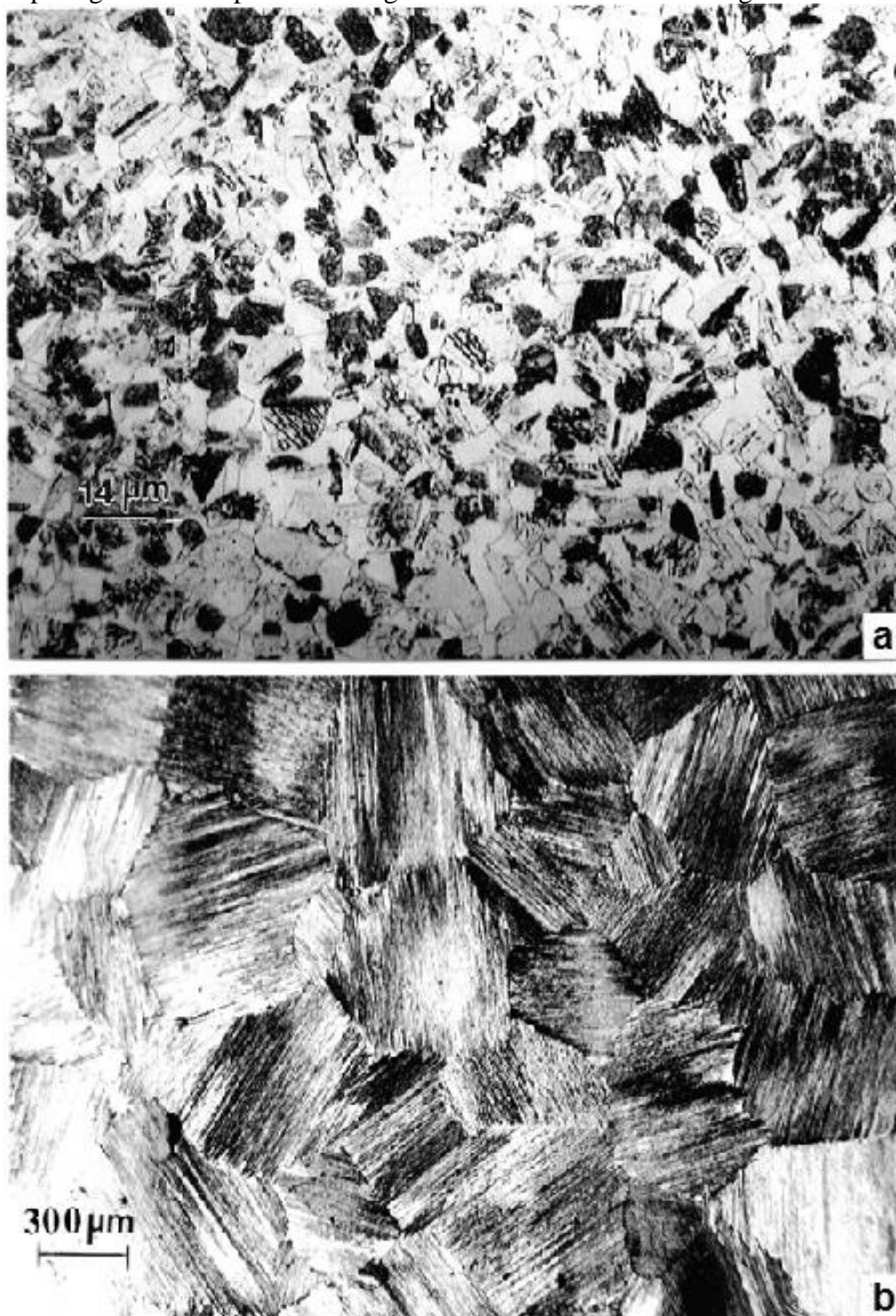


Figure 5.1.21: LOM views for annealed EBM-built blocks in the vertical reference plane (parallel to the build direction). (a) Anneal 1.): 1150°C at 5 h. (b) Anneal 2.): 1380°C at 1 h.

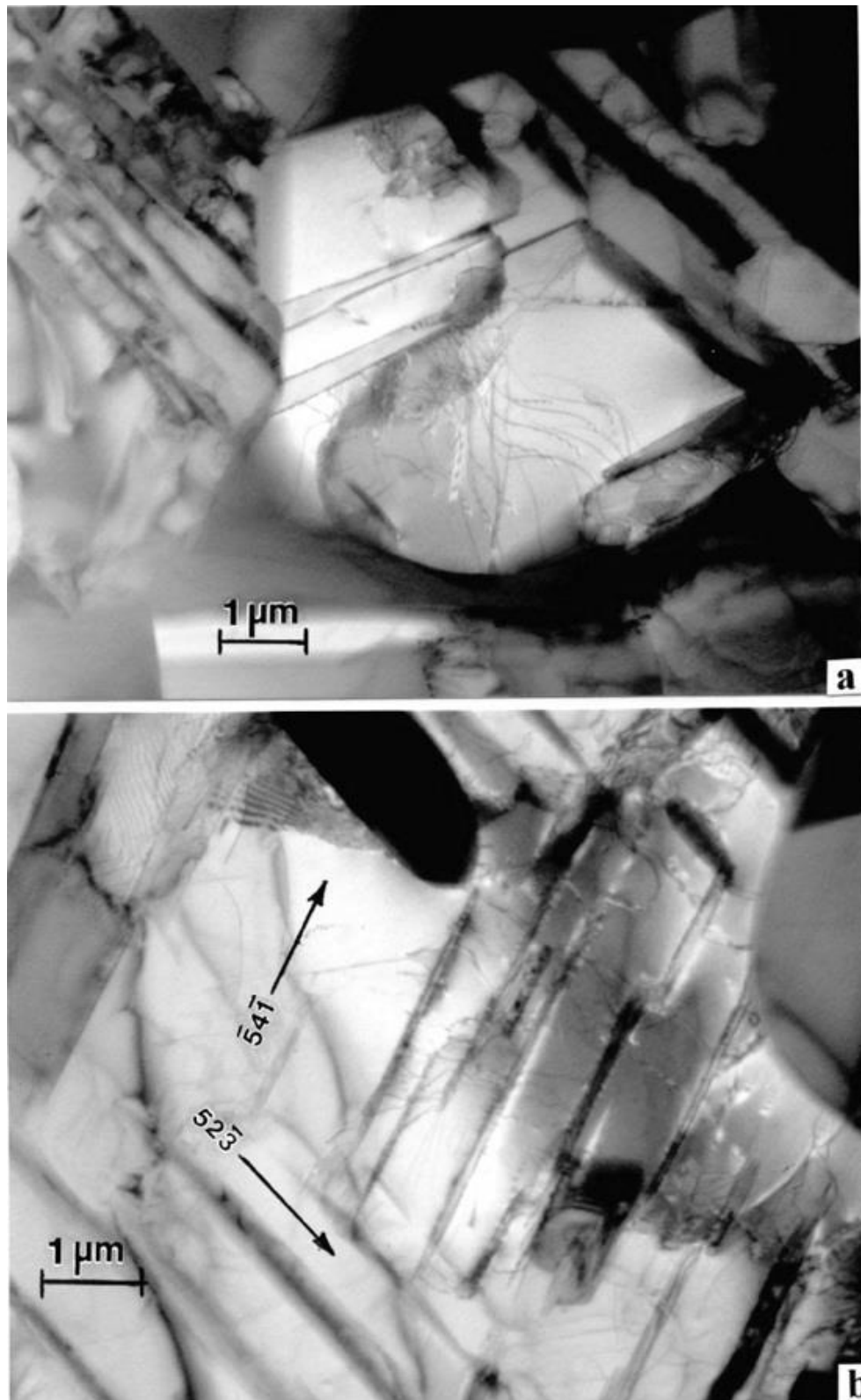


Figure 5.1.22: Bright-field TEM images representing Anneal 1.) (1150°C at 5 h.); corresponding to the LOM image in Figure 5.1.21(a). (a) Mixture of fine α_2 and γ -twins. (b) Similar features for a larger grain with a (123) surface orientation. Corresponding γ -{111} trace direction are noted.

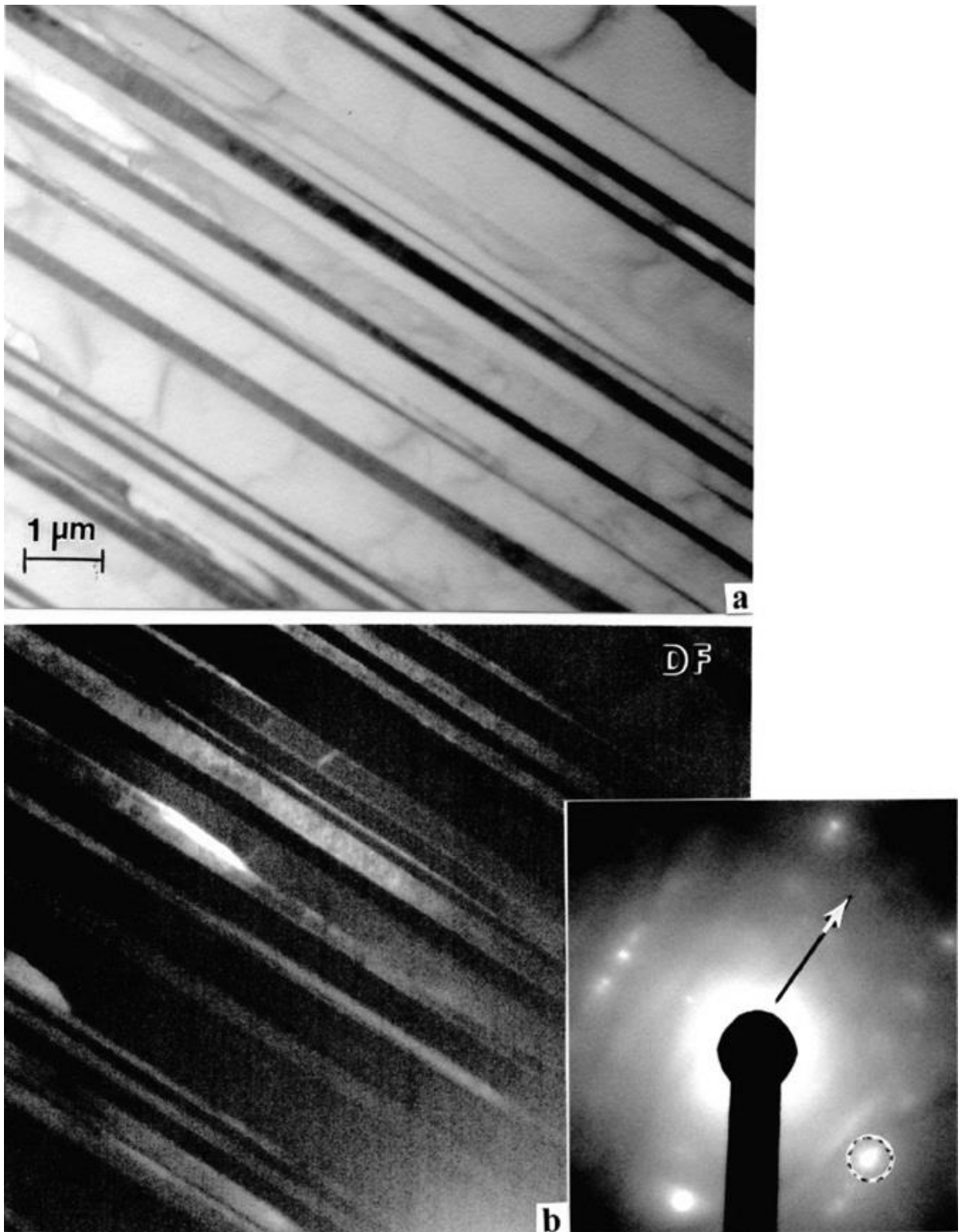
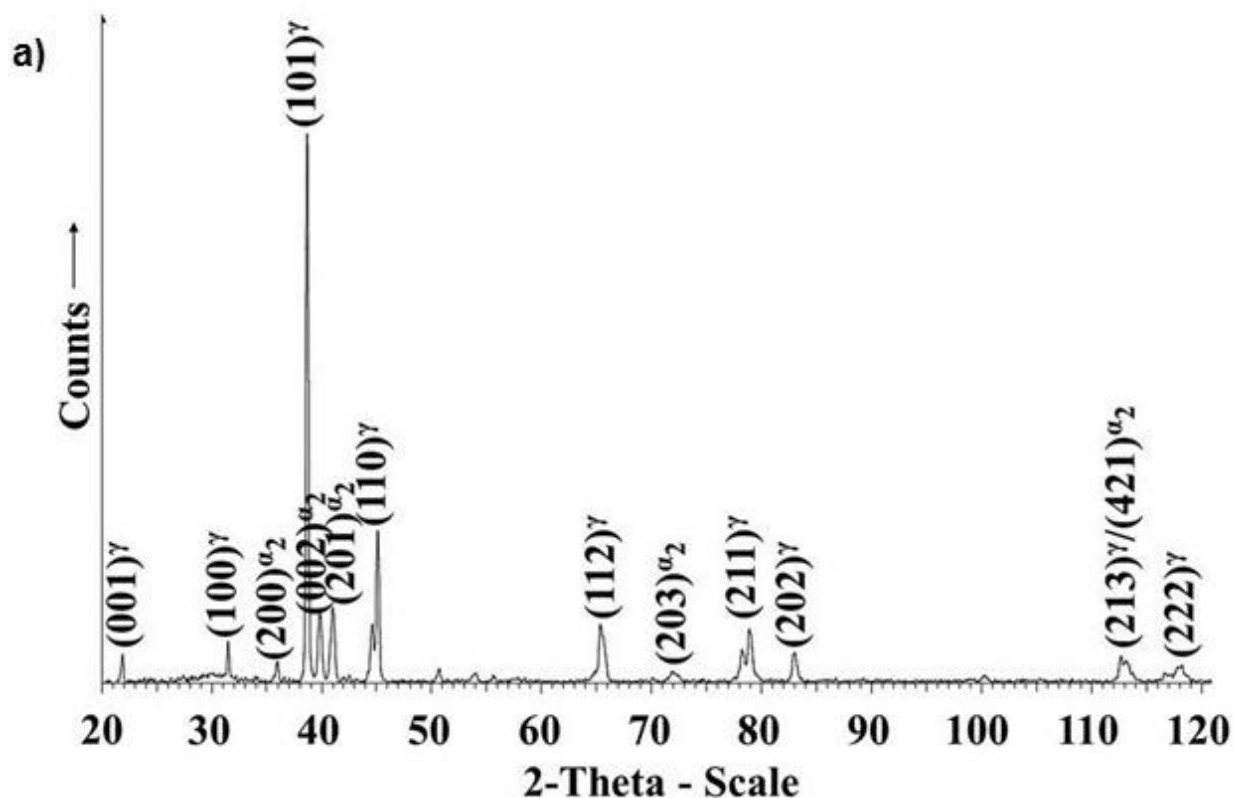


Figure 5.1.23: TEM bright-field (a) dark-field (b) image sequence utilizing the combined α_2/γ diffraction spots shown circled in the SAED pattern inset in (b). The TEM image sequence corresponds to Anneal 2.) (1380°C at 1 h.) in the vertical reference plane, characteristic of the LOM image in Figure 5.1.21(b). The arrow in the SAED pattern inset corresponds to $[11\bar{1}]$ for a (123) grain surface orientation.

The reduced α_2 -phase is also evident from the corresponding XRD spectra as represented for the vertical reference planes for the two anneal schedules as shown in Figure 5.1.24. The α_2 (002) and (201) peaks prominent in the 1150°C anneal (top in Figure 5.1.24) are absent in the 1380°C anneal (bottom in Figure 5.1.24). The α_2 (200) peak is small but unchanged for the two anneals. This is somewhat consistent with the TEM results shown in Figures 5.1.22 and 5.1.23, respectively. Taken together, Figures 5.1.21(b), 5.1.23, and the bottom XRD spectra in Figure 5.1.24 are indicative of a lack of α_2 (Ti_3Al) phase. TEM bright and dark-field analyses for the 1380°C anneal samples indicated a significant fraction of the lamellar “plates” to be γ -twins. This is illustrated typically in the bright-field/dark-field TEM images represented in Figure 5.1.25, where the grain surface orientation is (122), and the operating reflection for the twins coincided with the $(02\bar{2})$ diffraction spot. The average “lamellar” plate spacing was measured to be $\sim 0.9 \mu\text{m}$ from TEM images. This is also the twin width as illustrated in the dark-field image insert in Figure 5.1.25. Twin planes along $[41\bar{3}]$ in Figure 5.1.25 are coincident with $(1\bar{1}1)$ planes, inclined $\sim 79^\circ$ to the (122) grain surface plane.

Annealed at 1150°C for 5 hours – Vertical Plane



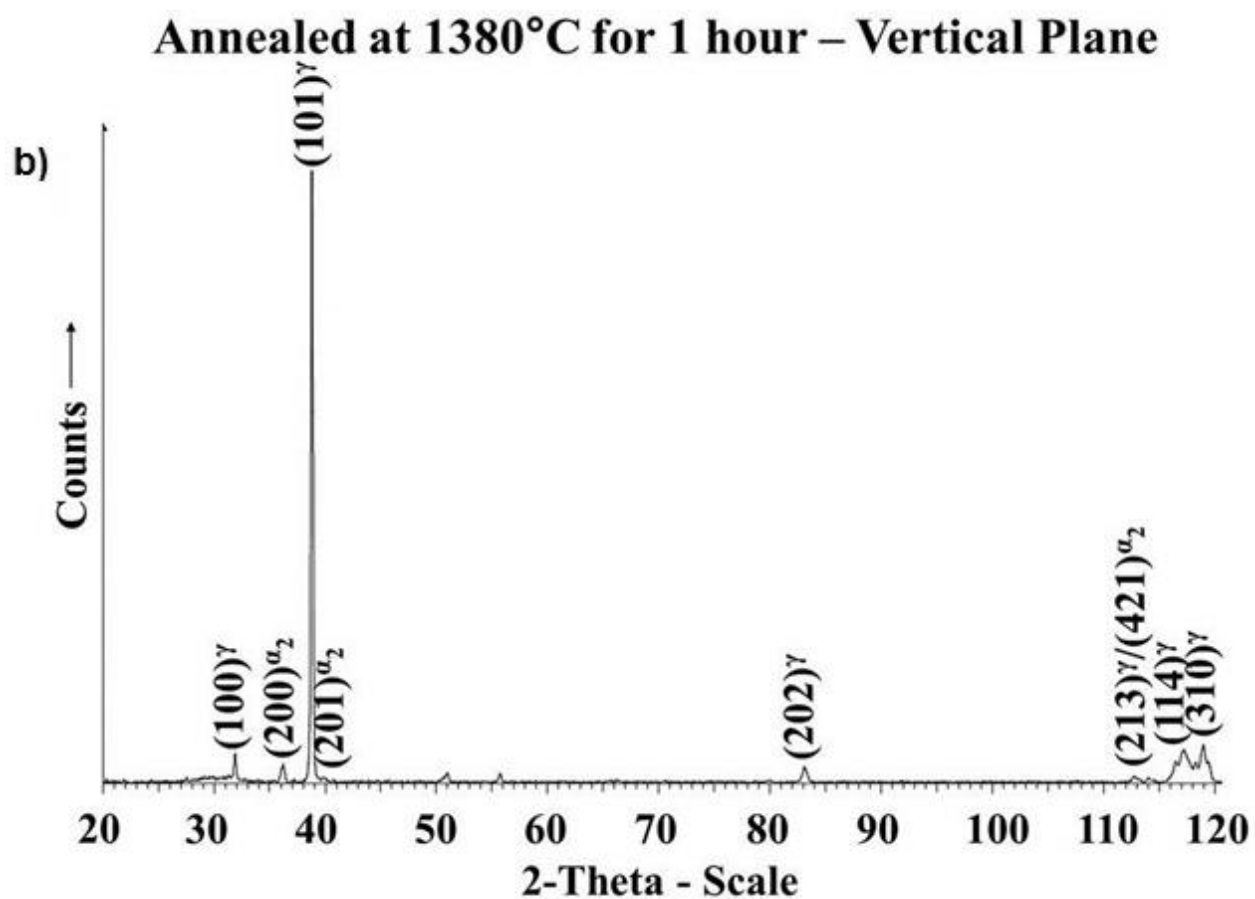


Figure 5.1.24: XRD spectra corresponding to the vertical reference planes represented in Figure 5.1.21(a) and (b), respectively, for annealed 1.) (a) and 2.) (b) EBM-fabricated components.

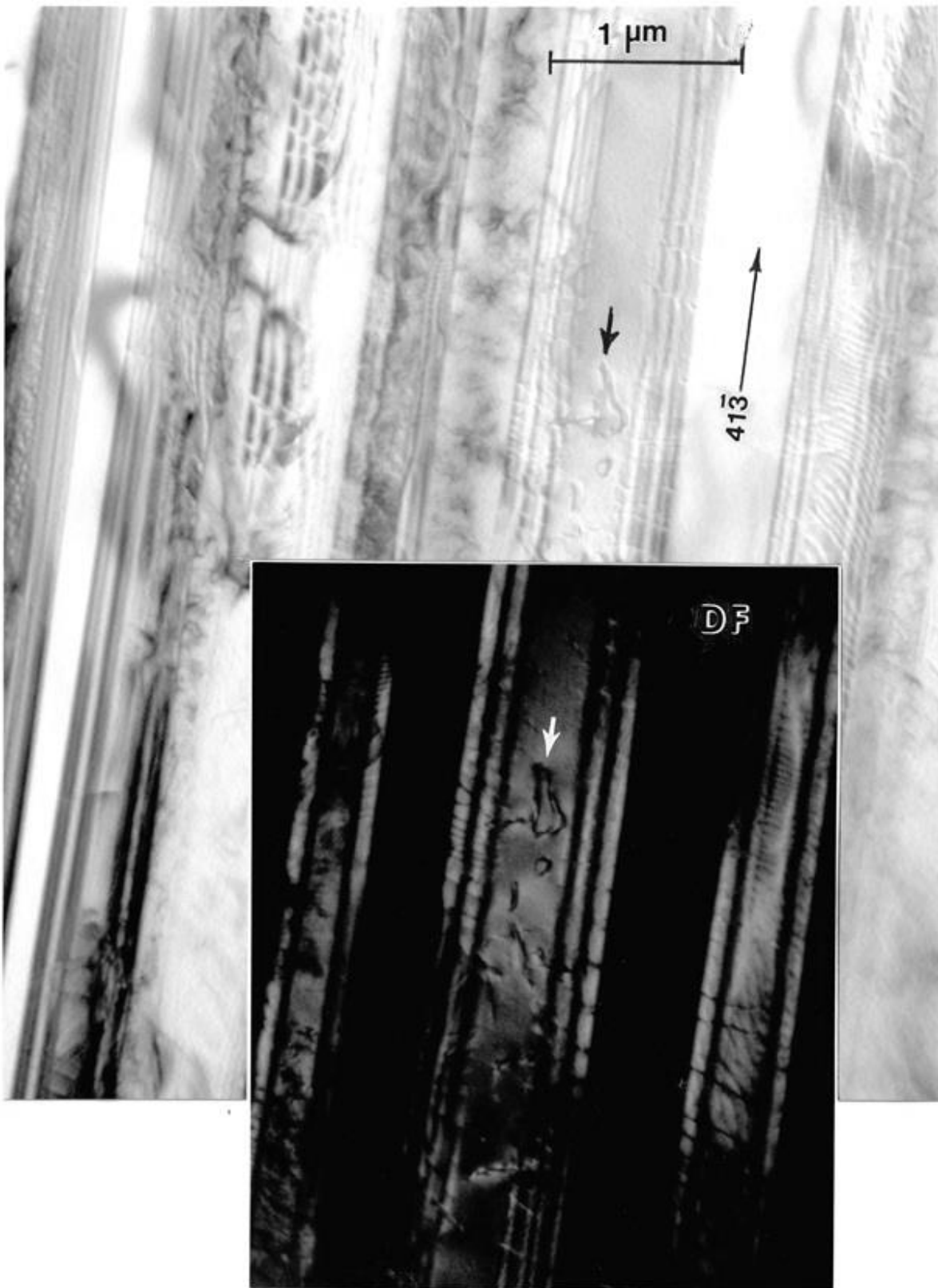


Figure 5.1.25: TEM bright-field image for γ -twins with (111) in a γ -TiAl (222) grain surface orientation. A DF image portion is inserted and corresponds to the twinned regions referenced by the arrow(s).

5.1.3 Discussion

Figure 5.1.21, in retrospect, represents a primarily γ -twinned (coherent $\{111\}$ boundaries) microstructure with twins (and some coincident α_2 -Ti₃Al phase platelets) forming a singular crystallographic ($\{111\}$) lamellar microstructure in the large, equiaxed grains. While the mechanism of twin formation is not fully understood, γ -twin boundary energies are certainly a fraction of the grain boundary energies, and their formation during anneal (at 1380°C), from a simple thermodynamic point of view, is consistent with a reduction in the total free energy; especially the interfacial free energy contribution (Murr, *et al.*, 1975). This energy reduction is further optimized by the growth of twin lamellae and the elimination of the coincident α_2 (-Ti₃Al) phase.

The lamellar γ -(TiAl) twin structures which dominate the 1380°C anneal (Figure 5.1.21(b)) are reminiscent of nanoscale growth twin lamellae observed by Lu, *et al.* (2005) in nano-grained copper synthesized by using a pulsed electrodeposition technique which allowed for the nano-twin spacings to be varied from ~100 nm to ~15 nm, and dramatically enhancing mechanical properties (as much as a ten-fold increase in tensile strength in contrast to commercial, bulk copper) (Lu, *et al.*, 2009). It is intriguing to speculate about the prospects for producing much smaller lamellar twin spacings in EBM-fabricated and selectively annealed γ -TiAl in order to enhance mechanical properties in a similar fashion, but not necessarily at the low-nano scale.

Some indication of prospects for manipulating the mechanical properties for EBM-fabricated γ -TiAl products is provided in Figure 5.1.26 which compares the Vickers microindentation hardness (HV) and the Rockwell C-scale (macroindentation) hardness (HRC) for the variety of EBM-fabricated products in this research program. Considering first the HV values (averaged in the horizontal and vertical reference planes for the solid block and cylindrical components and the block anneal schedules (Anneal 1.) and 2.)), there is a significant increment between the precursor (pre-alloyed) γ -TiAl powder and the foam ligaments. This is an indication of the α_2 (Ti₃Al) hardness representing a micro-dendritic structure in contrast to an equiaxed, α_2/γ grain structure in the foam ligaments. Correspondingly, the HV averages for all of the solid components (including the annealed block) vary only by a few percent. This is particularly notable on comparing the EBM-fabricate block (with an equiaxed grain size of ~15 μ m (containing) lamellar α_2/γ spaced ~100 nm)) with the 1380°C anneal (Anneal 2.)) where the

equiaxed grain size was 550 μm with a “lamellar” spacing of $\sim 0.9 \mu\text{m}$. Correspondingly the HV average increased slightly from 4.3 GPa to 4.5 GPa. In contrast, the HRC averages (Figure 5.1.26) declined for the EBM-fabricated block when annealed at 1380°C: from HRC 42 to HRC 35; a 17% decrease. This is probably due primarily to the increased grain size for the 1380°C anneal (Anneal 2.)). Certainly, optimizing the anneal schedule to reduce the grain size while simultaneously reducing the lamellar twin (or α_2 -phase) thickness (and spacing) could raise the strength significantly. This prospect for interfacial microstructural engineering could lead to significant advances for γ -TiAl applications for components fabricated by EBM, especially prospects for annealed foam components as illustrated in Figure 5.1.9.

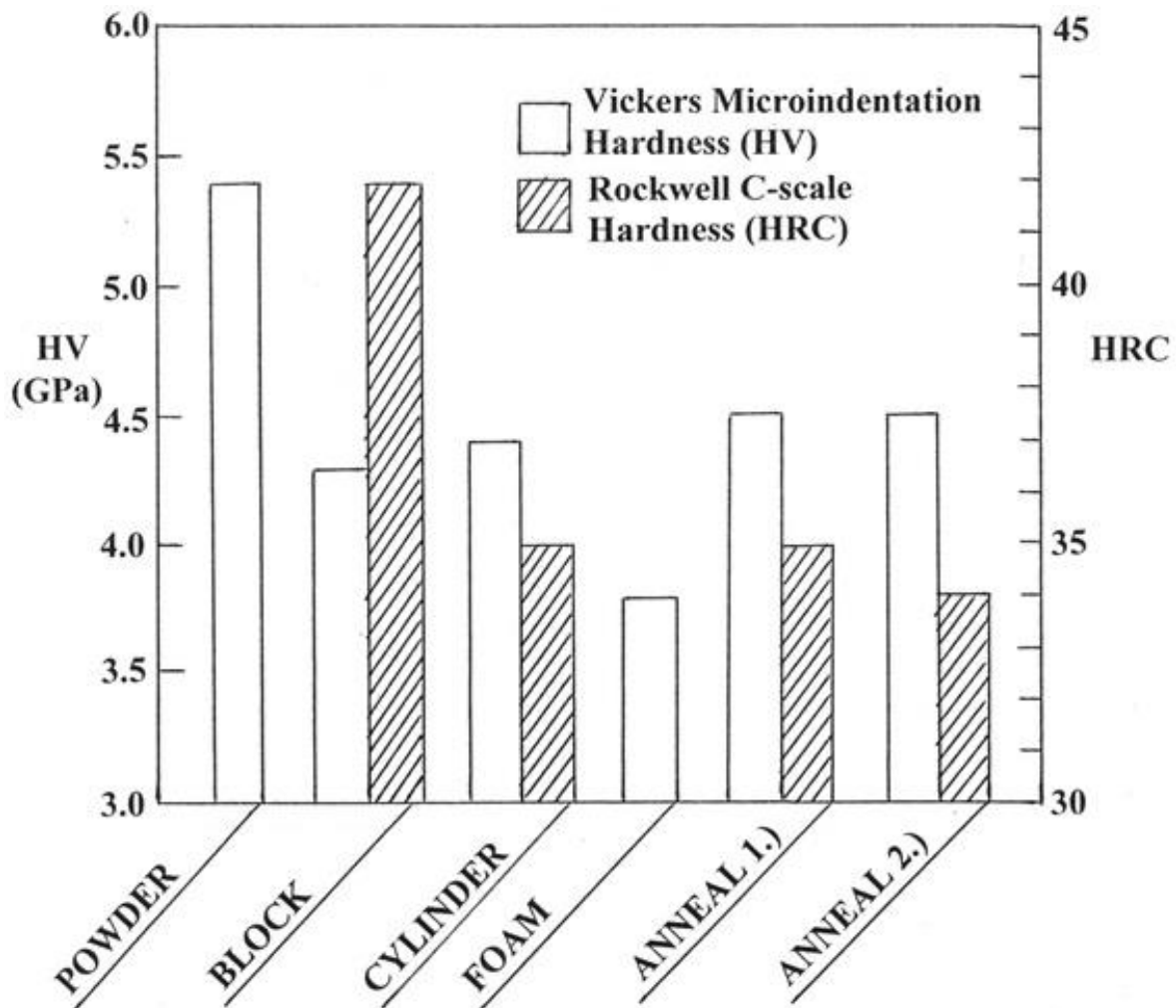


Figure 5.1.26: Comparison of Vickers microindentation hardness averages (HV) and Rockwell C-scale hardness averages (HRC) for experimental specimens noted. The block, cylinder, Anneal 1.), and Anneal 2.) specimens averaged measurements made in the horizontal and vertical reference planes.

In this context, it is interesting to note that the specific yield strength for γ (TiAl) has been shown to be a maximum of $\sim 150 \text{ MPa/g/cm}^3$ (Appel, 1998). However, assuming as a simple rule-of-thumb that the yield strength is equal to one-third of the Vickers microindentation hardness (Murr, *et al.*, 1975), the solid EBM-fabricated components exhibit a specific strength of 312 MPa/g/cm^3 while the lowest density foam (Figure 5.1.9) would have a corresponding specific strength of 3333 MPa/g/cm^3 (with reference to Figure 5.1.26). This foam strength corresponds to an ideal specific yield strength nearly 200 times the conventional γ -(TiAl) specific strength (Appel, *et al.*, 1998).

5.1.4 Summary

EBM fabrication of rectangular, solid blocks and cylinders (with nominal density of 3.85 g/cm^3) from pre-alloyed (Ti-48Al-2Cr-2Nb) powders has been examined by LOM and TEM. The microstructures exhibit a generally equiaxed, γ -TiAl grain structure with α_2/γ colonies exhibiting lamellar α_2/γ platelets. Grain sizes averaged $\sim 15 \text{ }\mu\text{m}$. This is in contrast to interdendritic spacings for mostly α_2 (Ti₃Al) in the precursor powder of $\sim 2 \text{ }\mu\text{m}$. XRD spectra for the solid components allowed α_2/γ to be estimated as 0.05 in contrast to ~ 0.5 for the precursor powder. Prototype foam components, ranging in density from 0.33 g/cm^3 to 0.46 g/cm^3 exhibited a ligament grain structure/duplex microstructure essentially the same as the solid components; including $\alpha_2/\gamma \cong 0.05$.

TEM bright and dark-field sequences for the solid block and cylinder EBM fabricated components confirmed the α_2/γ lamellar, duplex microstructures to be the same as those characterized earlier for more conventionally processed γ -TiAl: investment casting and powder metallurgy-produced ingots. This included the $(111)_\gamma \parallel (0001)\alpha_2$ orientation relationship.

Simple anneal schedules for the solid block EBM fabricated components included 1150°C @5h and 1380°C @1h. These produced a fine, equiaxed duplex grain structure ($\sim 3 \text{ }\mu\text{m}$) with $\alpha_2/\gamma < 0.05$, and a very large, equiaxed grain structure ($\sim 550 \text{ }\mu\text{m}$) with a fully lamellar microstructure, respectively. TEM bright and dark-field image sequencing along with XRD spectral data indicated that $\alpha_2/\gamma \ll 0.05$, and the lamellar structure to be mostly coherent $\{111\}$ γ -TiAl twins. This lamellar twin structure averaged twin widths and spacings of $\sim 0.9 \text{ }\mu\text{m}$ in contrast to lamellar α_2 (Ti₃Al) widths of $\sim 20 \text{ nm}$ and spacings of $\sim 0.1 \text{ }\mu\text{m}$ in the as-fabricated components.

Both annealed components (1150°C and 1380°C) exhibited Vickers microindentation hardnesses similar to the EBM-fabricated components, suggesting that optimizing the grain size and reducing the lamellar coherent twin spacings through selective annealing could allow for superior mechanical properties for a range of applications of EBM-fabricated γ -TiAl products.

5.2 MICROSTRUCTURES AND PROPERTIES FOR A SUPERALLOY POWDER MIXTURE PROCESSED BY ELECTRON BEAM MELTING

In this paper we explore the effect of selective mixing/blending a pre-alloyed TiAl-based powder with a pre-alloyed Ni-base (Alloy 625) powder on the development of solid and complex (open-cellular) components by electron beam melting (EBM). Of particular interest in this study was the comparison of residual microstructures and properties for 2-phase TiAl and alloy 625 (Inconel 625) components processed by EBM from pre-alloyed powders, with solid and open-cellular components produced by EBM from a 10:1 mixture of TiAl: alloy 625 powders. We also fabricated open-cellular (mesh and foam) components and measured the dynamic Young's modulus or stiffness for varying densities. The relative stiffness versus relative density for these open-cellular components was also compared with other metals and alloys.

The starting powders included a 2-phase Ti-48Al-2Cr-2Nb (atomic percent) pre-alloyed powder illustrated in Figure 5.2.1(a), having an average powder diameter of 52 μm , and a 65Ni-26Cr-6Mo-3Nb (atomic percent) pre-alloyed powder illustrated in Figure 5.2.1(b); having an average powder diameter of 22 μm . Table 5.2.1 shows comparative energy-dispersive X-ray spectrometer (EDS) analysis for the pre-alloyed powders in both weight percent and atomic percent along with the corresponding analysis for EBM-fabricated solid products. The 2-phase TiAl powder shown in Figure 5.2.1(a) had an equiaxed grain structure while the Alloy 625 powder shown in Figure 5.2.1(b) had a microdendritic structure. Figure 5.2.2 compares the X-ray diffraction (XRD) spectra for the two powders. Figure 5.2.2(a) shows a 2-phase α_2/γ mixture: γ -TiAl (fcc; $a = 2.84 \text{ \AA}$) and α_2 -Ti₃Al (hcp; $a = 5.77 \text{ \AA}$, $c = 4.62 \text{ \AA}$). Figure 5.2.2(b) shows the NiCr (fcc; $a = 3.59 \text{ \AA}$) matrix structure with a strong (111) texture for the Alloy 625 powder.

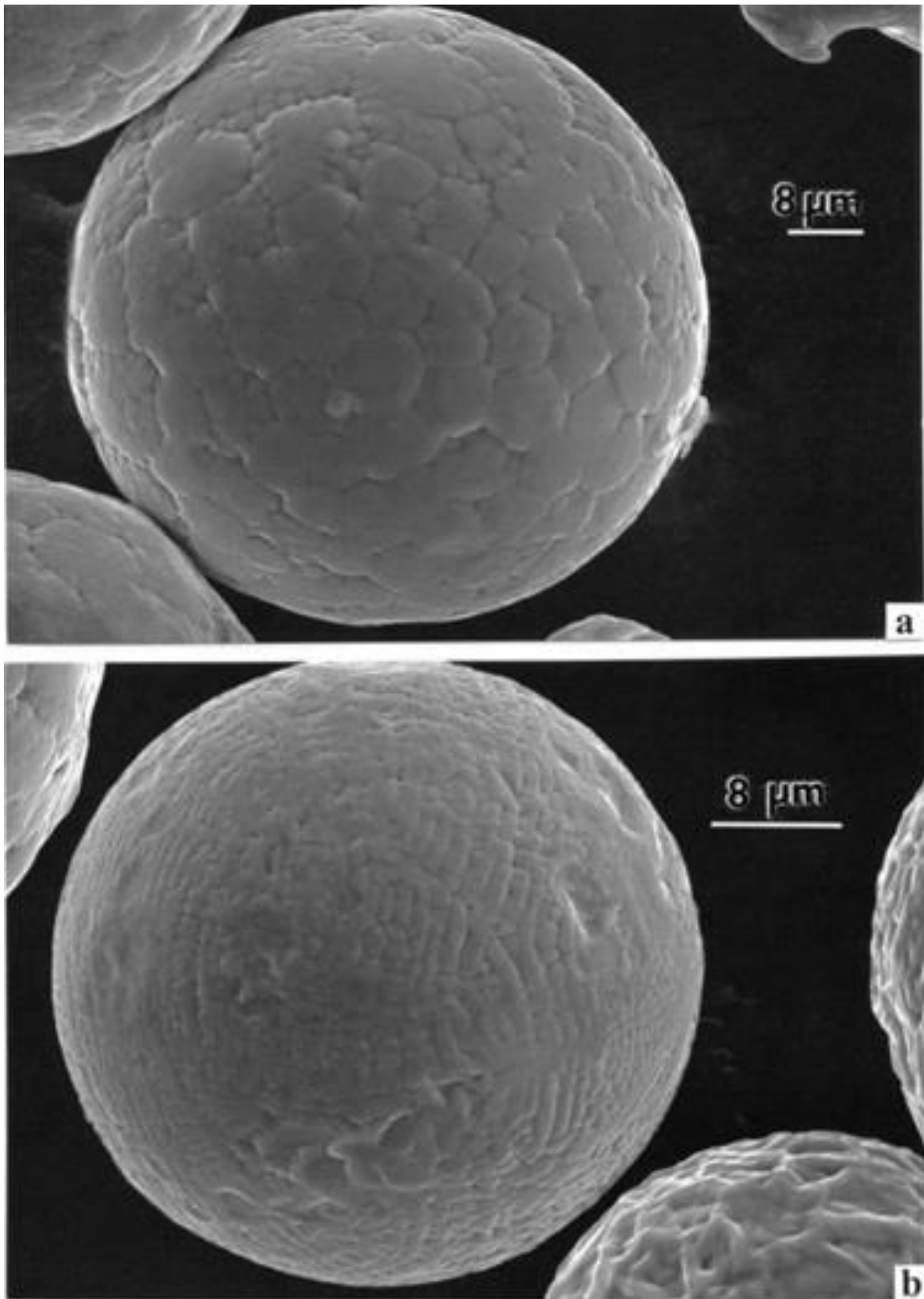


Figure 5.2.1: SEM views of pre-alloyed powder microstructure. (a) Gamma TiAl. (b) Inconel 625.

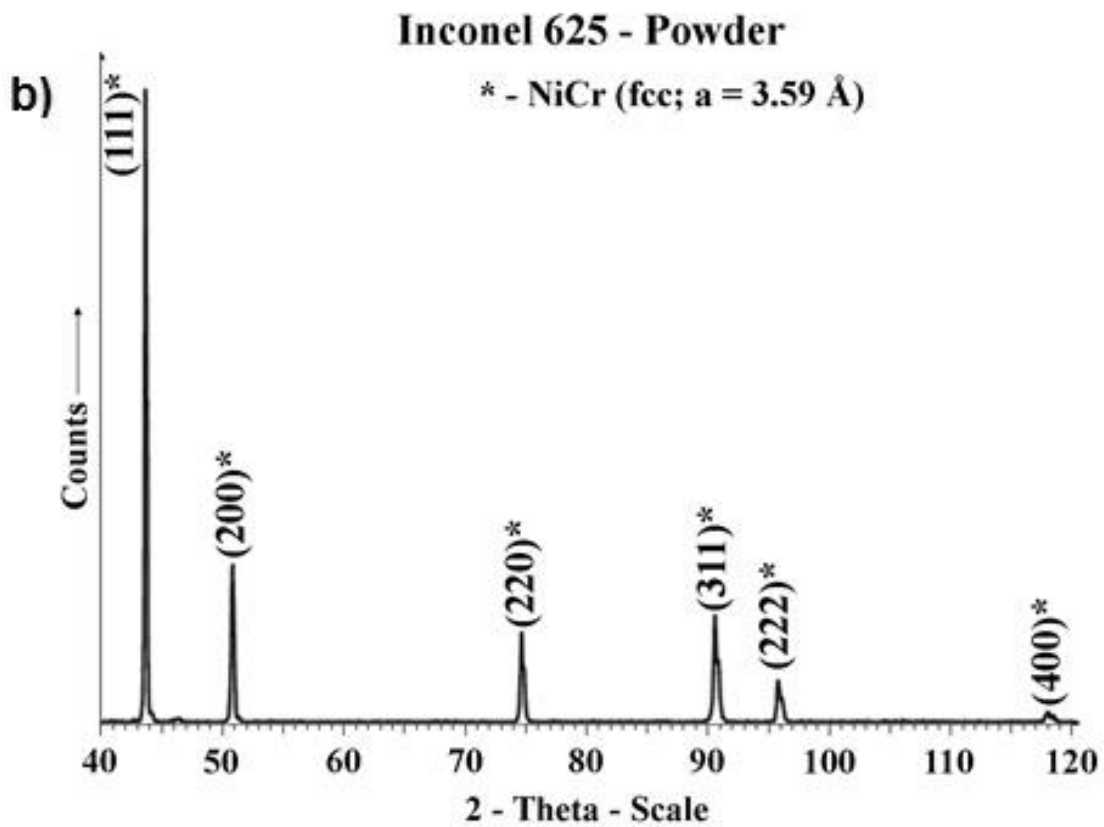
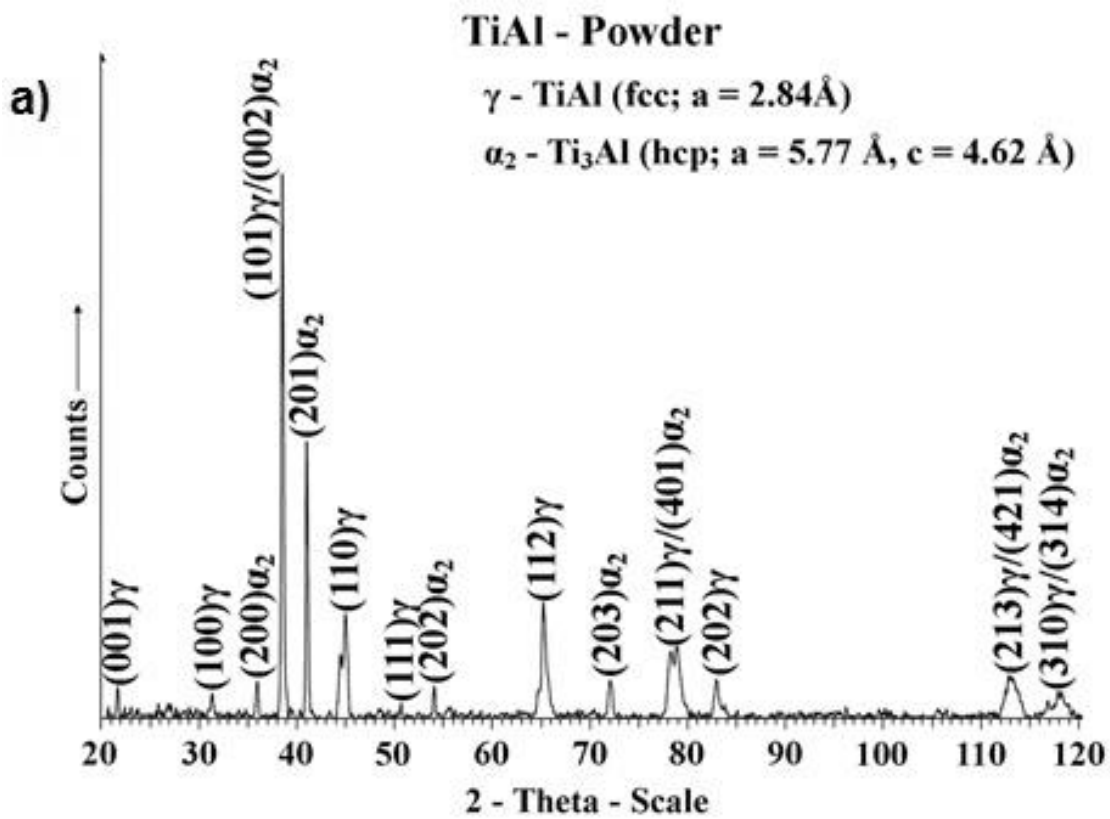


Figure 5.2.2: XRD spectra for pre-alloyed powders. (a) Gamma TiAl. (b) Inconel 625.

Table 5.2.1: Chemical Composition for Pre-Alloyed Powders and EBM Fabricated Solid Components.

Inconel 625 Powder – EDS Data*		
Element	Wt. %	At. %
Al	—	—
Nb	3.0	2.0
Ti	—	—
Cr	18.8	24.3
Ni	59.1	68.3
Mo	7.6	5.4
Total	88.5	100

Inconel 625 Solid Cylinder Component – EDS Data*		
Element	Wt. %	At. %
Al	—	—
Nb	4.7	3.2
Ti	—	—
Cr	19.2	23.9
Ni	61.1	67.1
Mo	8.8	5.8
Total	88	100

TiAl Powder – EDS Data*		
Element	Wt. %	At. %
Al	33.80	48.53
Nb	4.92	2.05
Ti	58.74	47.53
Cr	2.54	1.89
Total	100	100

TiAl Solid Component – EDS Data*		
Element	Wt. %	At. %
Al	31.52	45.99
Nb	5.36	2.28
Ti	60.46	49.22
Cr	2.66	2.02
Total	100	99.51

***20 kV accelerating potential**

5.2.1 Comparative Microstructures for Solid Alloy 625, 2-Phase TiAl, and Blended TiAl

Figure 5.2.3 shows a 3D-OM composition for an alloy 625 solid cylindrical component fabricated by EBM. The 3D image shows 2 μm -spaced, columnar arrays of γ'' Ni_3Nb lenticular-like precipitates (bct: $a = 3.62 \text{ \AA}$, $c = 7.41 \text{ \AA}$) coincident with the NiCr (fcc: $a = 3.59 \text{ \AA}$) matrix $\{111\}$ planes. The 2 μm cellular-like arrays observed in the horizontal reference section also show low-angle grain boundaries (GB) characterizing columnar, oriented (and textured) grains. While these microstructural issues have been described in more detail in previous work (Murr, *et al.*, 2011a; Amato, *et al.*, 2012), Figure 5.2.4 shows a TEM bright-field image for the γ'' coincident precipitates approximating a vertical reference plane section shown circled at the arrow to the left in the 3D image of Figure 5.2.3. Precipitates along $\langle 112 \rangle$ directions in the (110) surface orientation shown in Figure 5.2.4 (at 2 and 3) are at 90° to the (110) specimen surface plane, and therefore represent the precipitate thickness which is observed to approximate 50 nm. Precipitates in the $[\bar{1}10]$ direction shown by (1) in Figure 5.2.4 are coincident with (111) planes inclined 35° to the (110) specimen surface, and allow their microstructure to be observed in the projected image profile. Figure 5.2.5 shows XRD spectra corresponding to the horizontal and vertical reference planes, respectively, corresponding to the 3D image composition in Figure 5.2.3. The prominent (220) or (110) texture illustrated in the vertical reference plane in Figure 5.2.5(b) corresponds to the (110) image view shown in Figure 5.2.4.

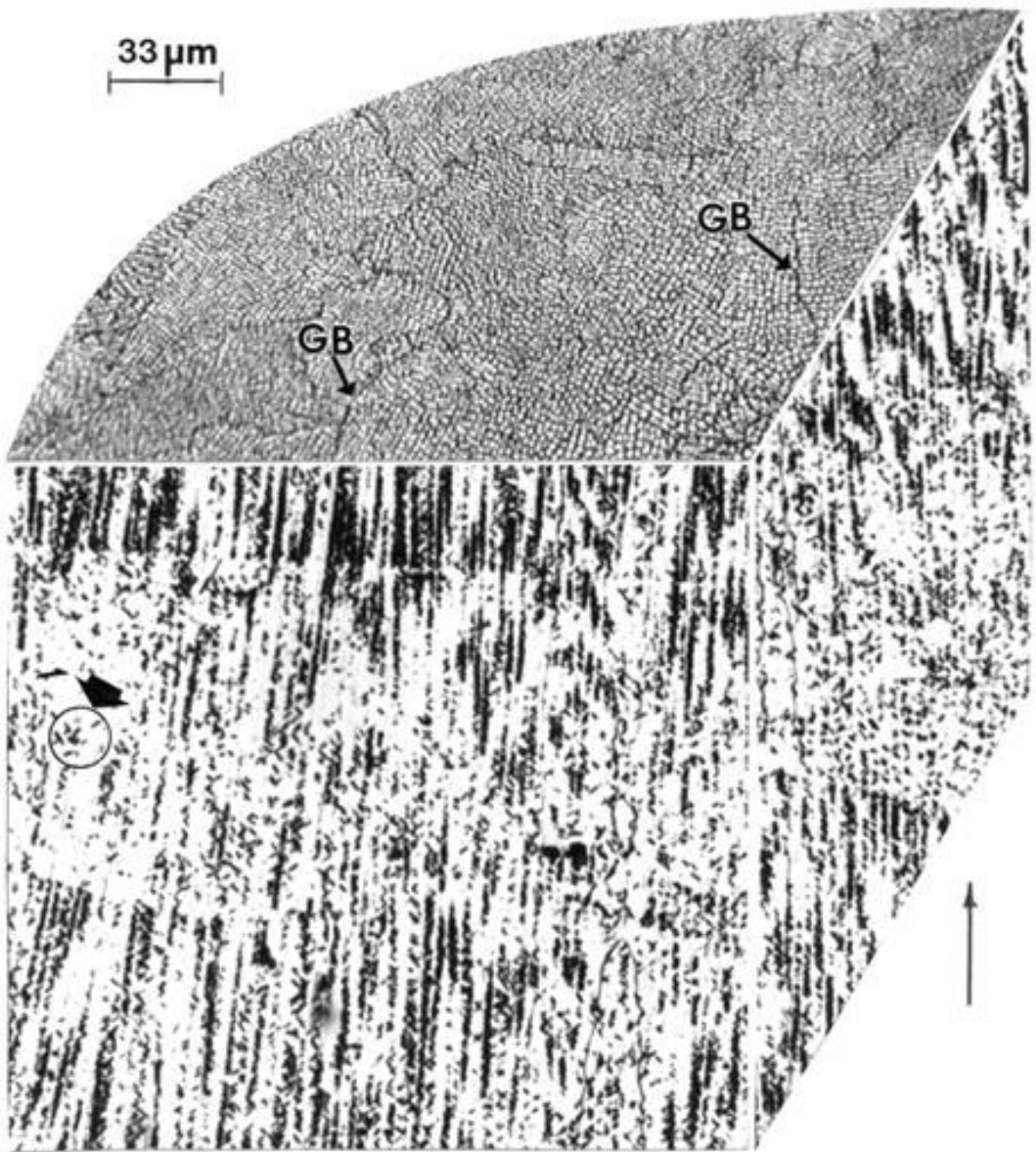


Figure 5.2.3: 3D OM composite section for an EBM fabricated Alloy 625 component. The build direction is shown by the lower right arrow. Grain boundaries are denoted by GB.

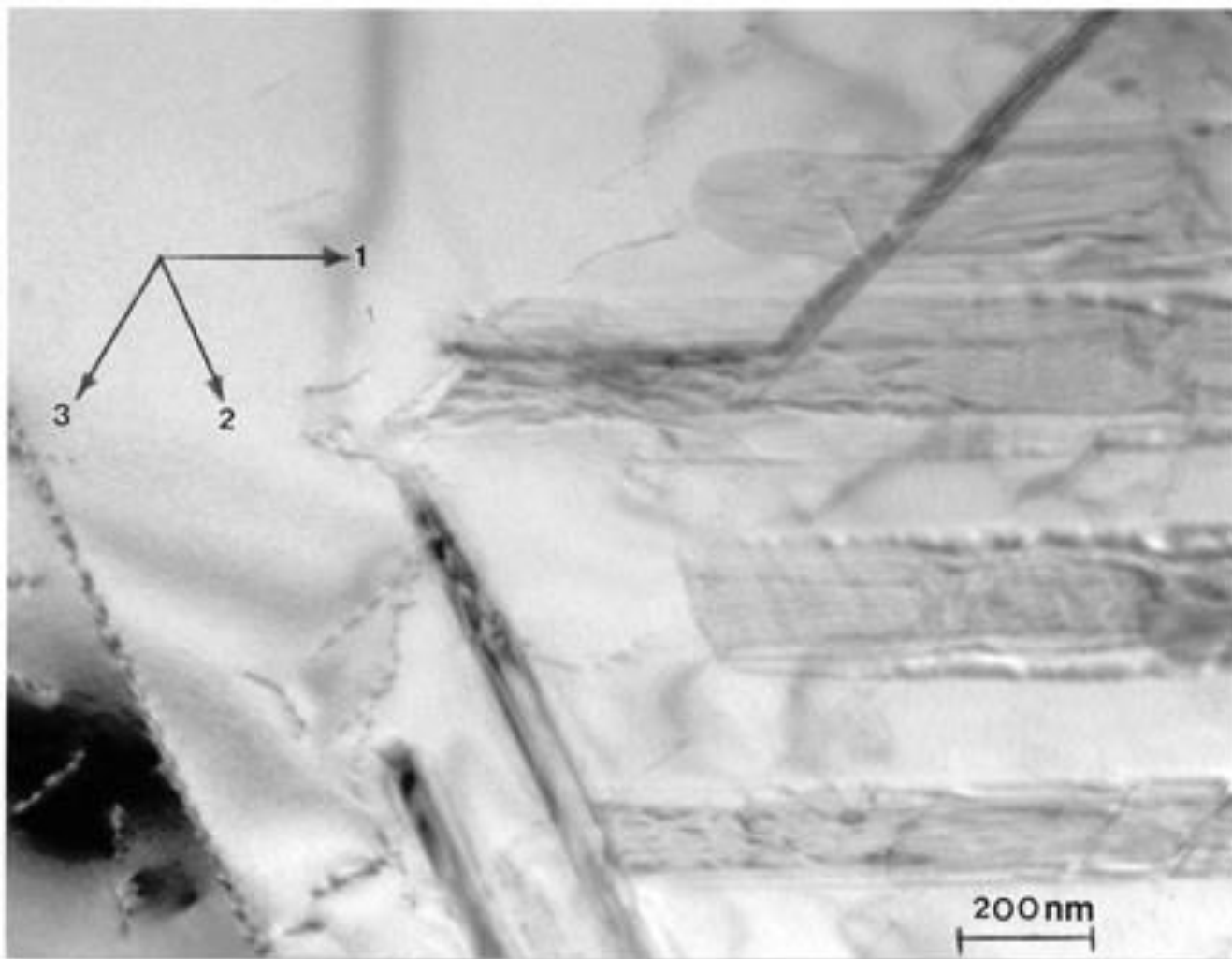


Figure 5.2.4: TEM vertical plane section view (parallel to the build direction in Figure 5.2.3; characteristic of the circled zone (arrow)). The grain surface orientation is (110). The trace directions shown correspond to $[1\bar{1}0]$ (1); $[1\bar{1}2]$ (2); $[\bar{1}12]$ (3).

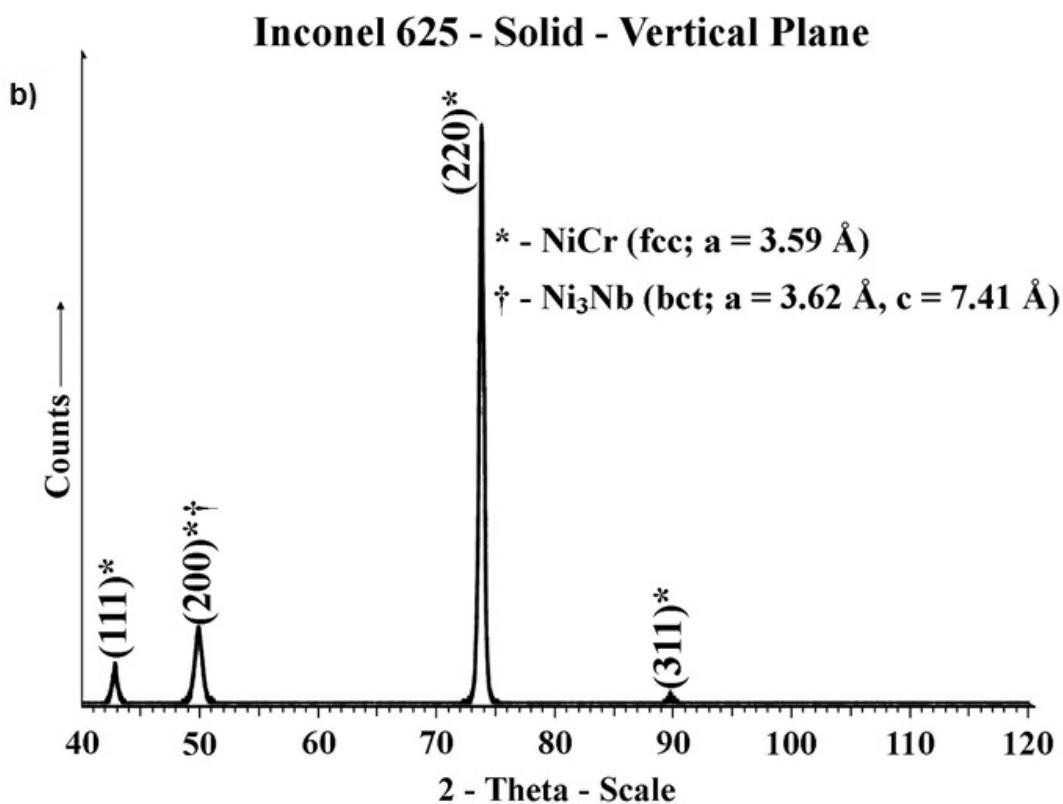
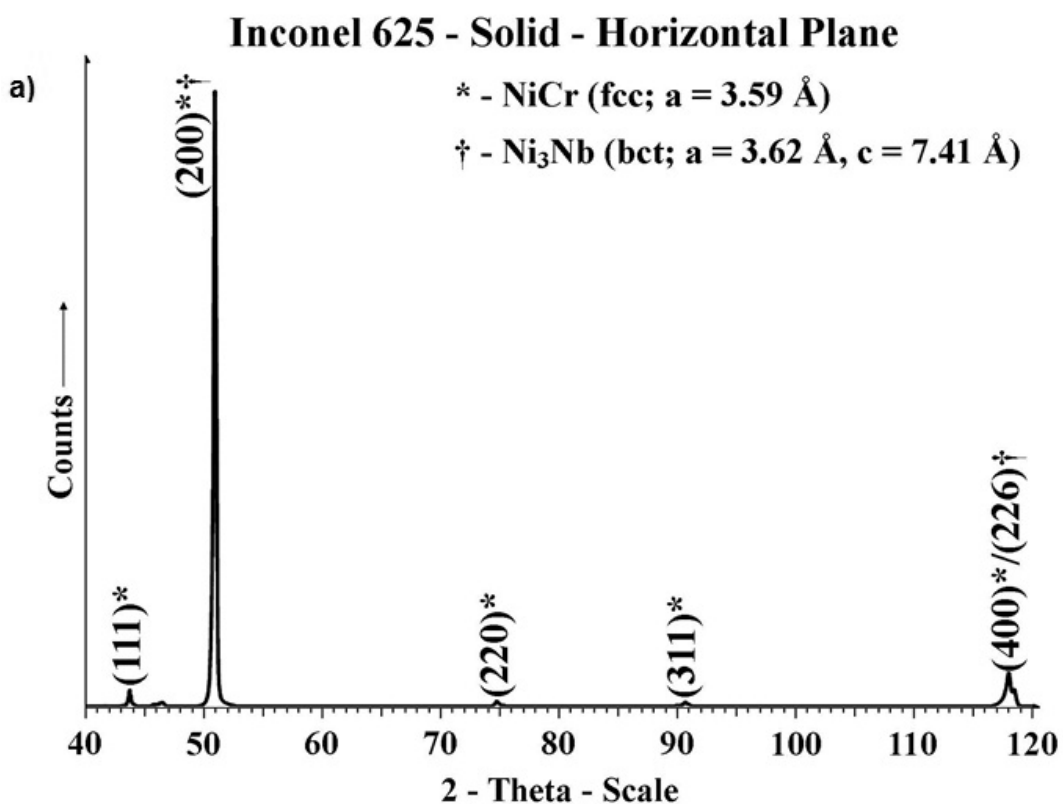


Figure 5.2.5: XRD spectra corresponding to the horizontal (a) and vertical (b) reference plane for an Inconel 625 EBM-fabricated cylindrical component (Figure 5.2.3).

Figures 5.2.6 and 5.2.7 show corresponding 3D OM image compositions for the EBM fabricated solid blocks and cylinders of 2-phase TiAl and the blended TiAl powders, respectively. Figure 5.2.6 illustrates the dual-phase (duplex) α_2/γ , equiaxed grain structure composed of colony-lamellar substructures discussed in detail by (Froes, *et al.*, 1992; Appel *et al.*, 2000; Hernandez, *et al.*, 2012). Figure 5.2.7 shows, for comparison, the multi-phase, blended TiAl microstructure.

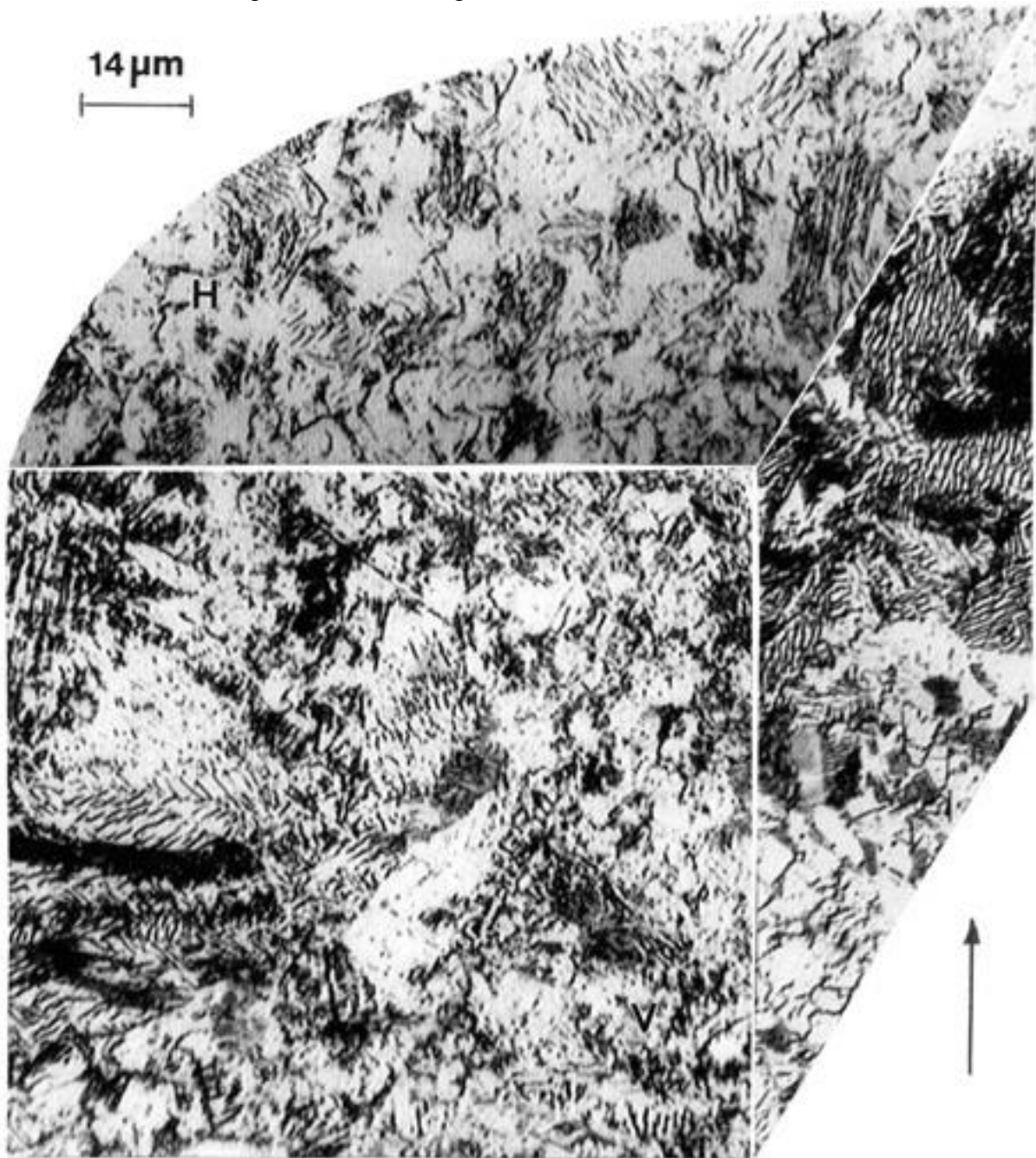


Figure 5.2.6: 3D OM image composite section for an EBM-fabricated 2-phase TiAl component. The build direction is shown by the arrow (lower right).

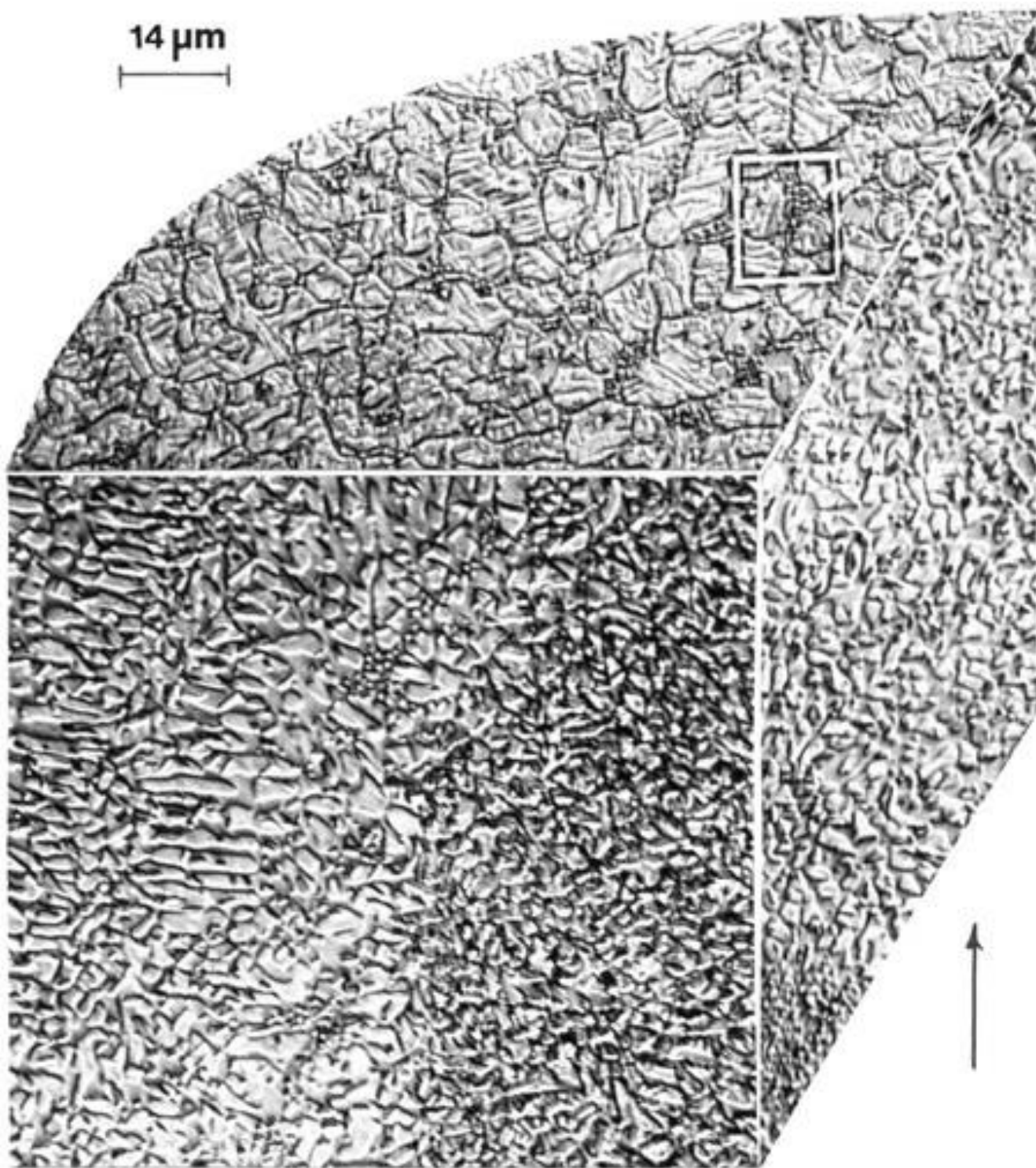
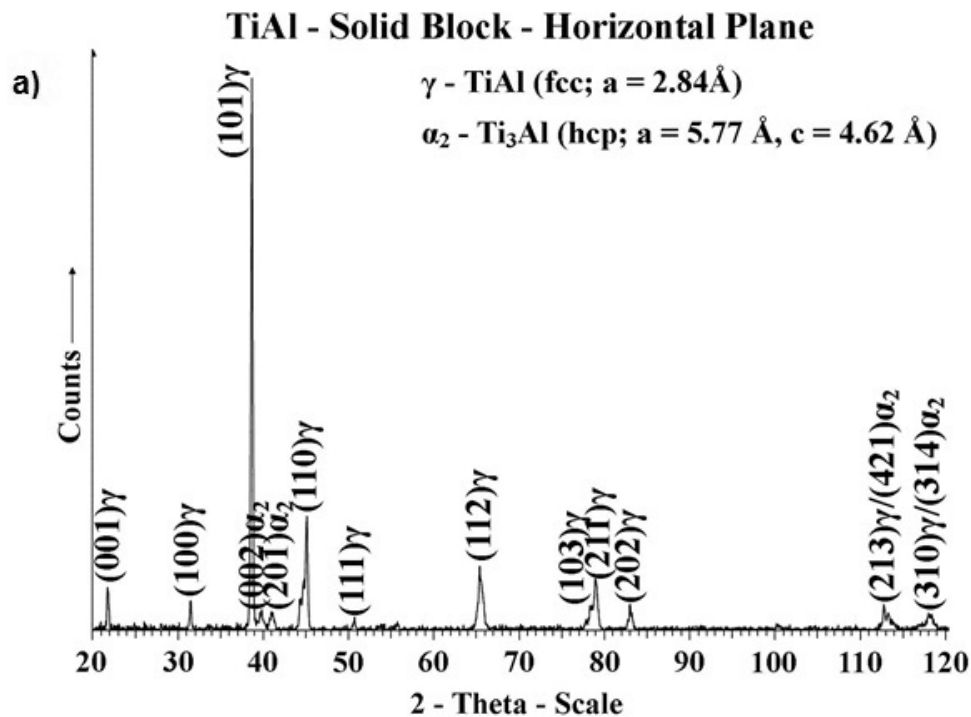


Figure 5.2.7: 3D OM image composite section for an EBM-fabricated blended TiAl component. The build direction is shown by the arrow (lower right).

The comparative XRD spectra representing the horizontal and vertical reference planes of the 3D OM image compositions in Figures 5.2.6 and 5.2.7 are shown in Figures 5.2.9 and 5.2.10. The XRD spectra for the duplex TiAl components shown in Figure 5.2.9 illustrates a generally (101) γ texture for the equiaxed grain structure containing lamellar α_2 as shown in Figure 5.2.8(a). Correspondingly, the XRD spectra for the blended TiAl components shown in Figure 5.2.10 illustrate the complex, multiphase microstructure with peaks representing γ -TiAl, α_2 -Ti₃Al, NbCr₂ (laves phase), MoNb (bcc) phase, and Ni₃Al eutectic. The NbCr₂ laves phase was observed for EBM-fabricated and hipped alloy 625 (Murr, *et al.*, 2011a) and has been observed in welded Inconel 718 by Radakrishna, *et al.* (1995). In addition, MoNb precipitates were prominently observed in selective laser melted (SLM) and hipped alloy 625 (Amato, *et al.*, 2012).



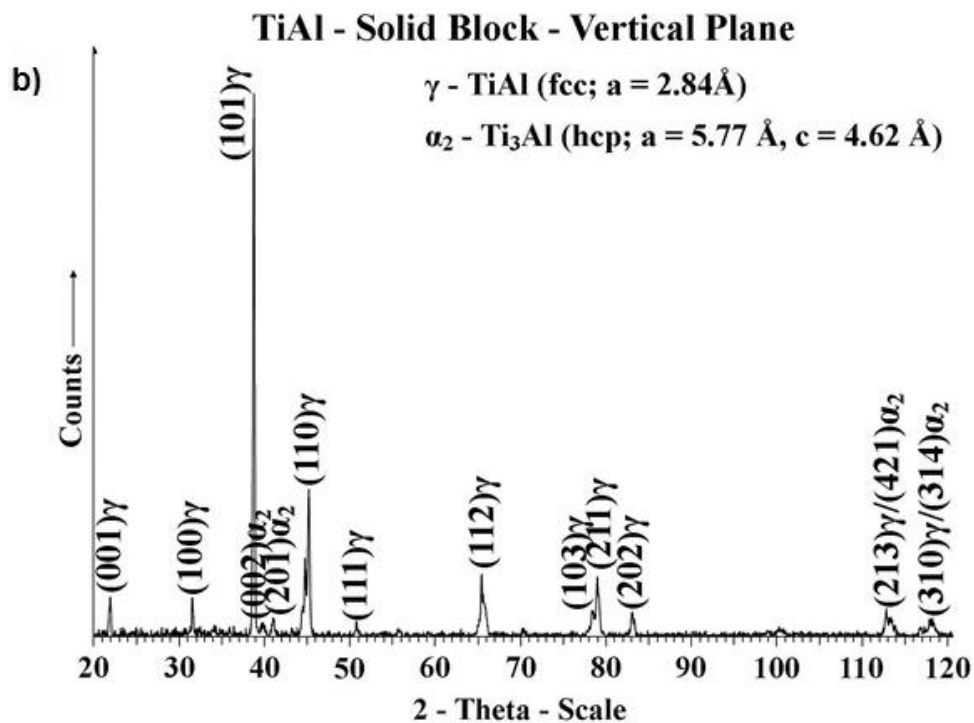
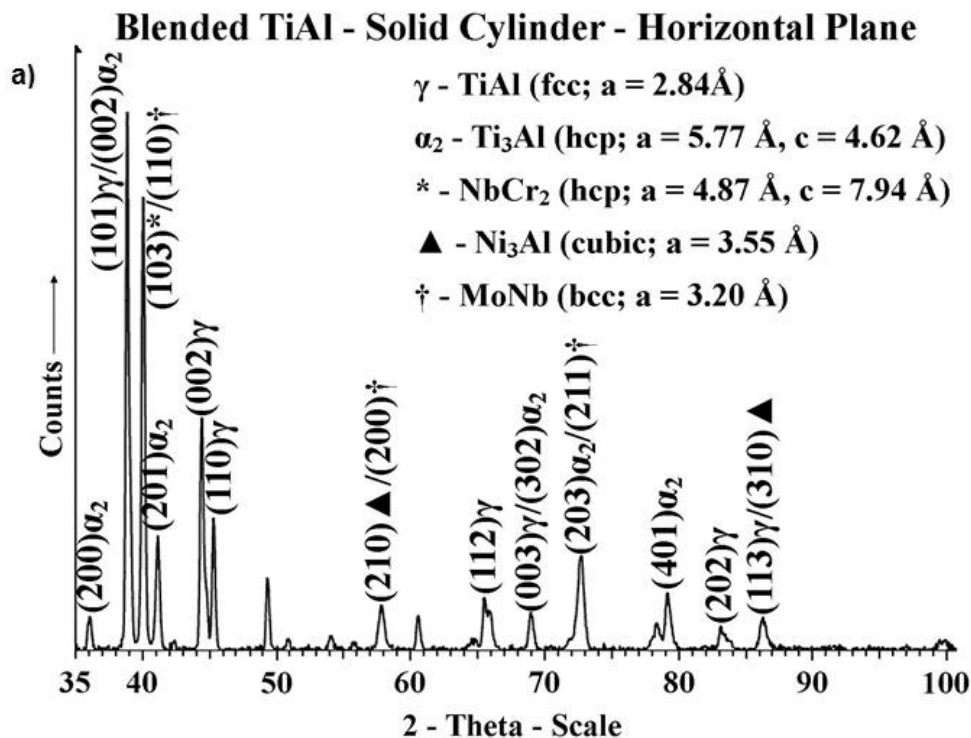


Figure 5.2.9: XRD spectra corresponding to the horizontal reference plane (a) and vertical reference plane (b) for a 2-phase TiAl EBM-fabricated component.



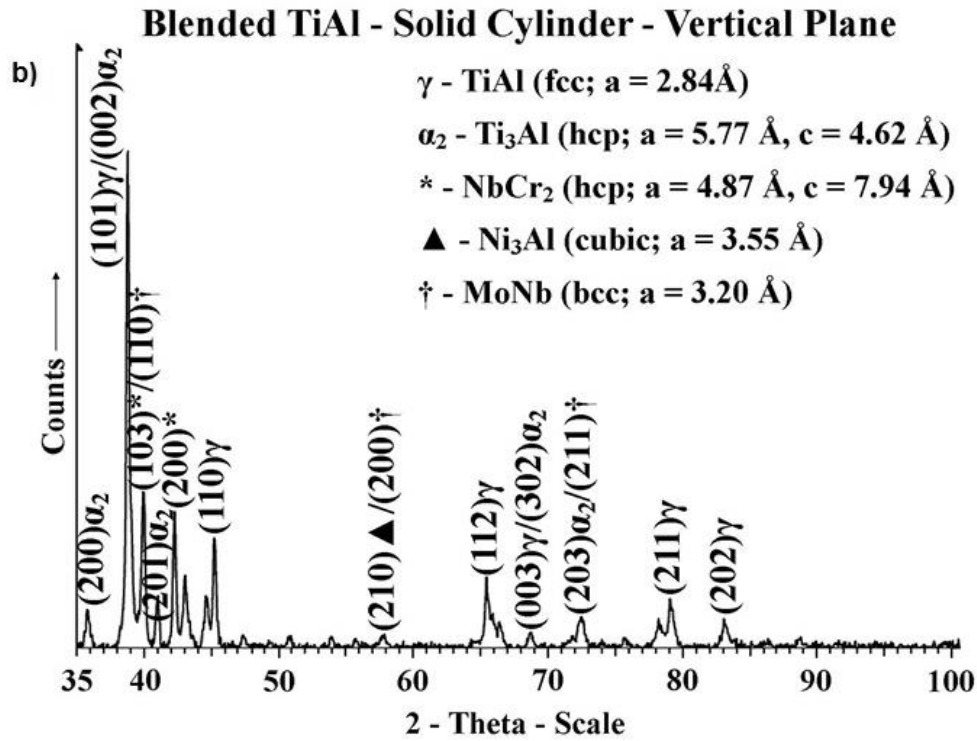


Figure 5.2.10: XRD spectra corresponding to the horizontal reference plane (a) and vertical reference plane (b) for a blended TiAl EBM-fabricated component.

Table 5.2.2 shows the quantitative EDS elemental analysis corresponding to a blended TiAl section shown typically in Figure 5.2.7 along with comparative analysis for EBM-fabricated mesh and foam components to be described in detail later. In contrast to Table 5.2.1, corresponding to an accelerating voltage of 20 kV in the SEM, Table 5.2.2 shows elemental quantitation for 30 kV which is well above the excitation potential ($\sim 16\text{-}18$ kV) for Mo and Nb. In addition, it should be noted that Mo and Nb L-line radiation peaks closely overlap in the EDS spectrum, while $K\alpha$ -spectra are more distinguishable at 30 kV.

Table 5.2.2: Chemical Composition for Blended TiAl Components Fabricated by EBM.

Blended TiAl Solid Cylinder Component – EDS Data – 30kV		
Element	Wt. %	At. %
Al	23.70	38.49
Nb	8.34	3.94
Ti	48.57	44.43
Cr	4.50	3.79
Ni	8.74	6.53
Mo	3.84	2.82
Total	97.69	100

Blended TiAl Mesh Component – EDS Data – 30kV		
Element	Wt. %	At. %
Al	23.42	37.94
Nb	9.84	4.64
Ti	53.78	49.08
Cr	3.24	2.72
Ni	4.12	3.29
Mo	5.60	2.56
Total	100.01	100.23

Blended TiAl Foam Component – EDS Data – 30kV		
Element	Wt. %	At. %
Al	22.48	37.03
Nb	10.06	4.82
Ti	51.83	48.10
Cr	3.37	2.88
Ni	5.08	3.85
Mo	7.18	3.33
Total	100	100.01

Detailed X-ray mapping and quantitative elemental analysis was conducted for secondary electron (SE) and backscatter electron (BE) images for the blended TiAl components represented typically in Figure 5.2.7. Figure 5.2.11 illustrates an example of this analysis. Figure 5.2.11(a) shows a BE image for a horizontal reference plane section represented conceptually by the enclosure (box) in Figure 5.2.7. A larger phase region, representing the equiaxed “grains” in Figure 5.2.7, is shown at A in Figure 5.2.11(a). This region is bounded by another phase regime indicated by B, while within the A phase there are sub-phase regions marked C and D. D, shown in the circled region in Figure 5.2.11(a), shows dark-contrast nanophases or precipitates. There are essentially 4 shades shown by A, B, C, and D in Figure 5.2.11(a) representing essentially 4 different atomic number (Z) contrast regimes. Figure 5.2.11(b) to (d) illustrate elemental maps for Ti, Ni, and Mo, respectively corresponding to Figure 5.2.11(a); especially regions designated A and B. Region A is observed to be Ti-rich while region B is Ni-rich. Slightly more Mo is observed in region A, and the corresponding Nb map was observed to be identical to that for Mo in Figure 5.2.11(d). Al and Cr were observed to be distributed homogeneously, with the Cr concentration only roughly 20% of the Al concentration. While there is little Ni in phase region A in Figure 5.2.11(a), there is some Ti in region B. More detailed analysis of phases indicated by C in Figure 5.2.11(a) showed Ti_3Al plus a few atomic percent Nb and Mo while the darkest regions shown designated D in Figure 5.2.11(a) contained mostly Ti and Al; $\text{TiAl} \cong 1:1$ (in atomic percent). These regions contained about 3 atomic percent each of Nb, Mo, and Cr. Region A in general contained a Ti:Al ratio of 2:1 (atomic percent) and an Nb:Cr ratio of 1:2 (atomic percent). Region B in Figure 5.2.11(a) was dominated by a nominal 35Ti-45Al-14Ni composition.

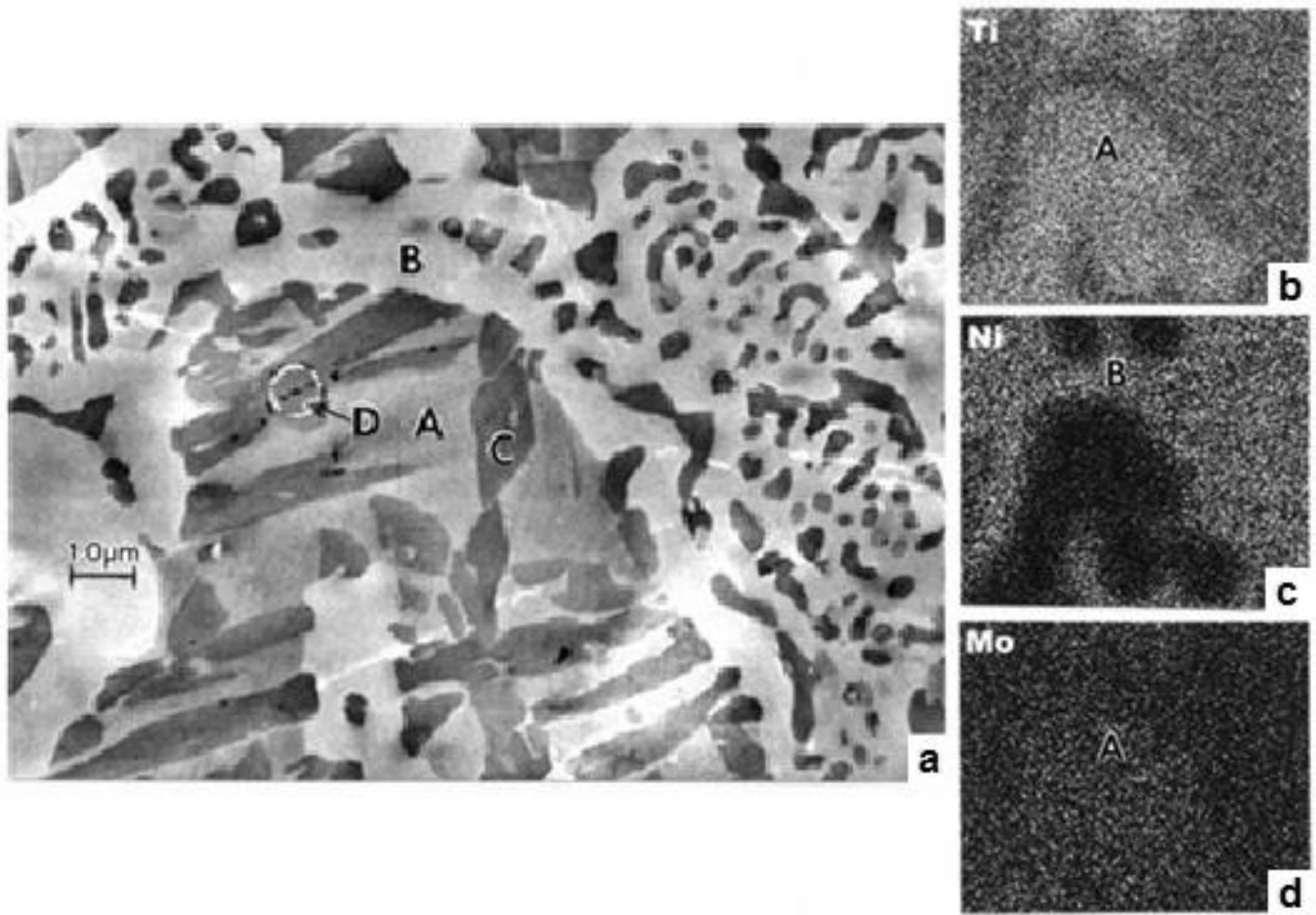
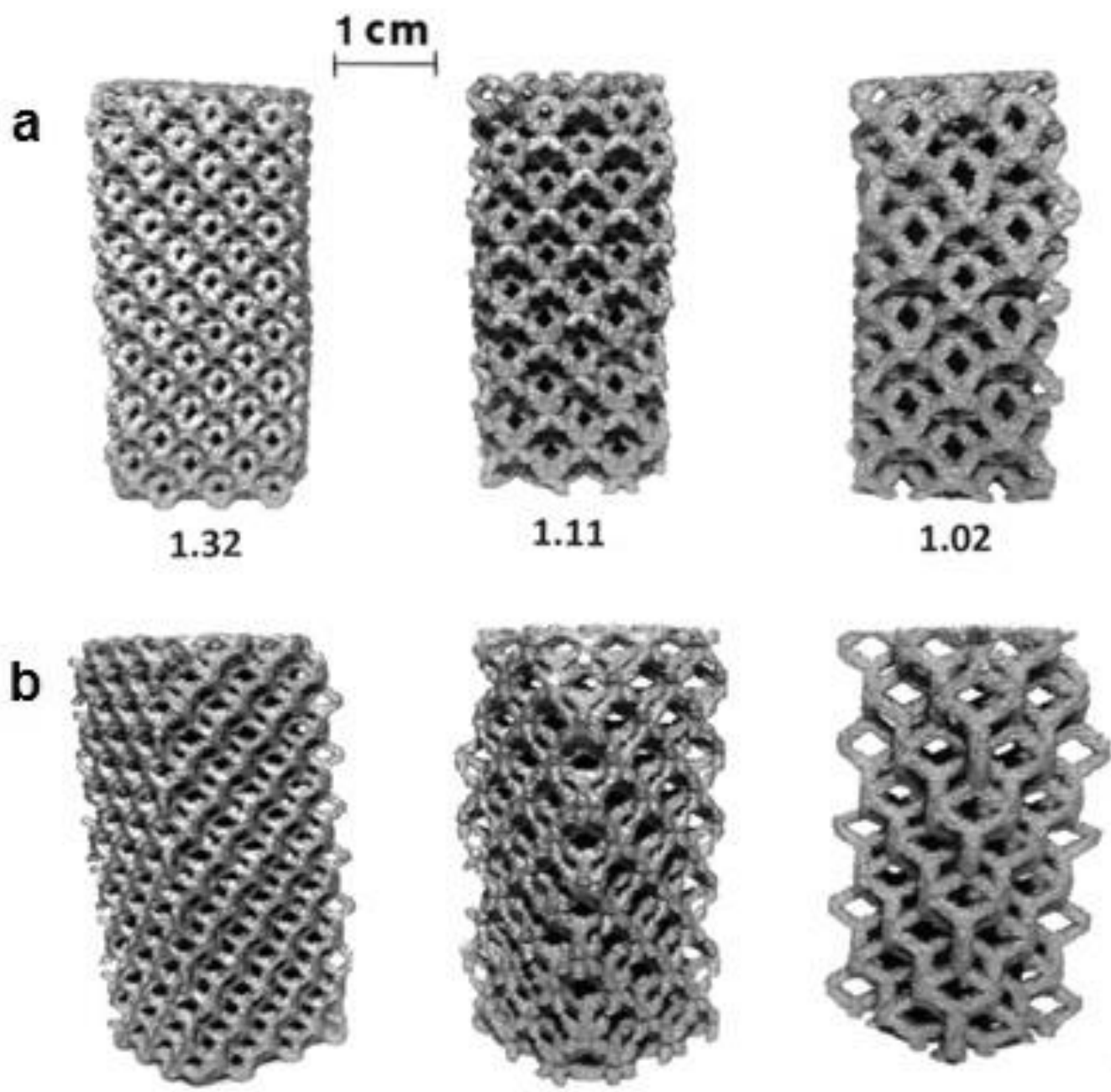


Figure 5.2.11: SEM analysis sequence representing an area corresponding to the horizontal surface region shown in the box in Figure 5.2.7. (a) BE image showing complex phase structure and atomic number (Z) contrast. Phase regions are denoted A, B, C, D. (b) Ti X-ray map. (c) Ni X-ray map. (d) Mo X-ray map. (20 kV accelerating potential)

5.2.3 Open Cellular Mesh and Foam Components

Utilizing a stochastic foam element and a dode-thin reticulated mesh element, foam and mesh components measuring $2.3 \text{ cm} \times 2.3 \text{ cm} \times 3.5 \text{ cm}$ height were fabricated with the following densities: foam: $\rho = 0.74, 0.88, 1.00 \text{ g/cm}^3$; mesh: $\rho = 1.02, 1.11, 1.32 \text{ g/cm}^3$. Figure 5.2.12 illustrates these EBM fabricated components. Figure 5.2.12(a) and (b) show the three mesh components viewed at 45° (face and diagonal or edge views: (a) and (b), respectively). Figure 5.2.12(c) shows the three corresponding foam components. Figure 5.2.13 shows mounted and polished sections for the 1.11 g/cm^3 mesh (Figure 5.2.13(a)) and the 0.74 g/cm^3 foam. The corresponding cylindrical mesh strut dimensions in contrast to the triangular foam ligament cross-sections can be observed on comparing Figure 5.2.13(a) and (b). In

contrast to the regular strut arrays for the mesh components, the foam ligaments form along the edges of randomly packed polyhedral cells with 9 to 17 faces (Jang, *et al.*, 2008; Gibson & Ashby, 1997).



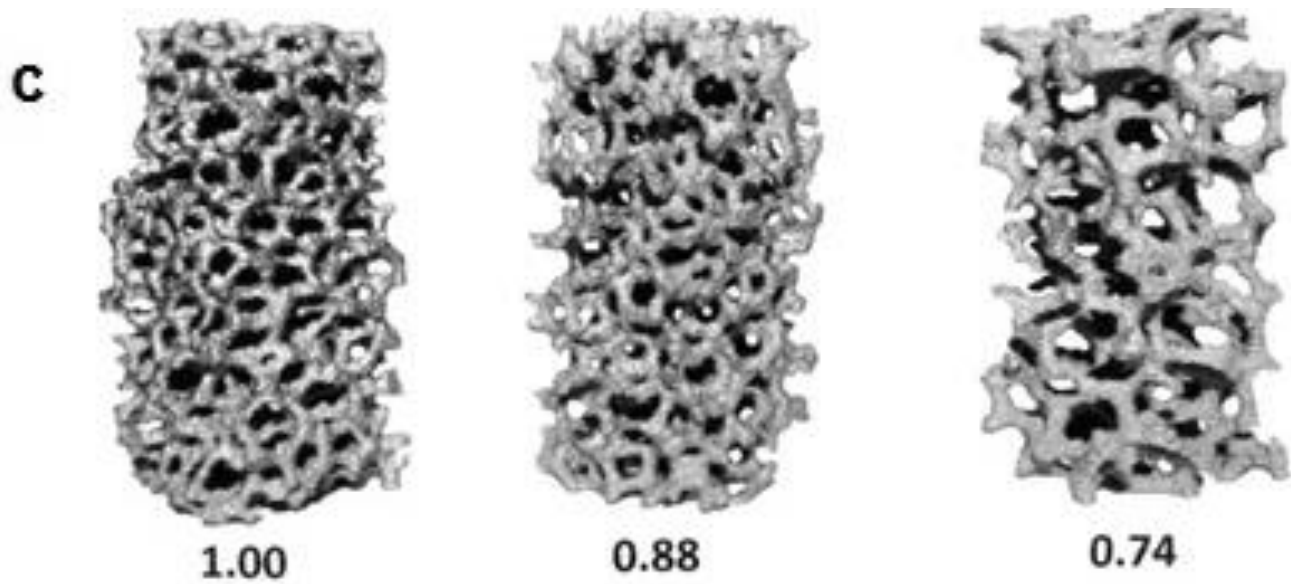


Figure 5.2.12: EBM-fabricated open-cellular structures. (a) Mesh components observed in the face plane. Arrow shows the build direction. (b) Mesh components observed along an edge at 45° to the face view in (a). Densities shown in units of g/cm^3 . (c) Foam components observed in the face plane. Densities shown in units of g/cm^3 .

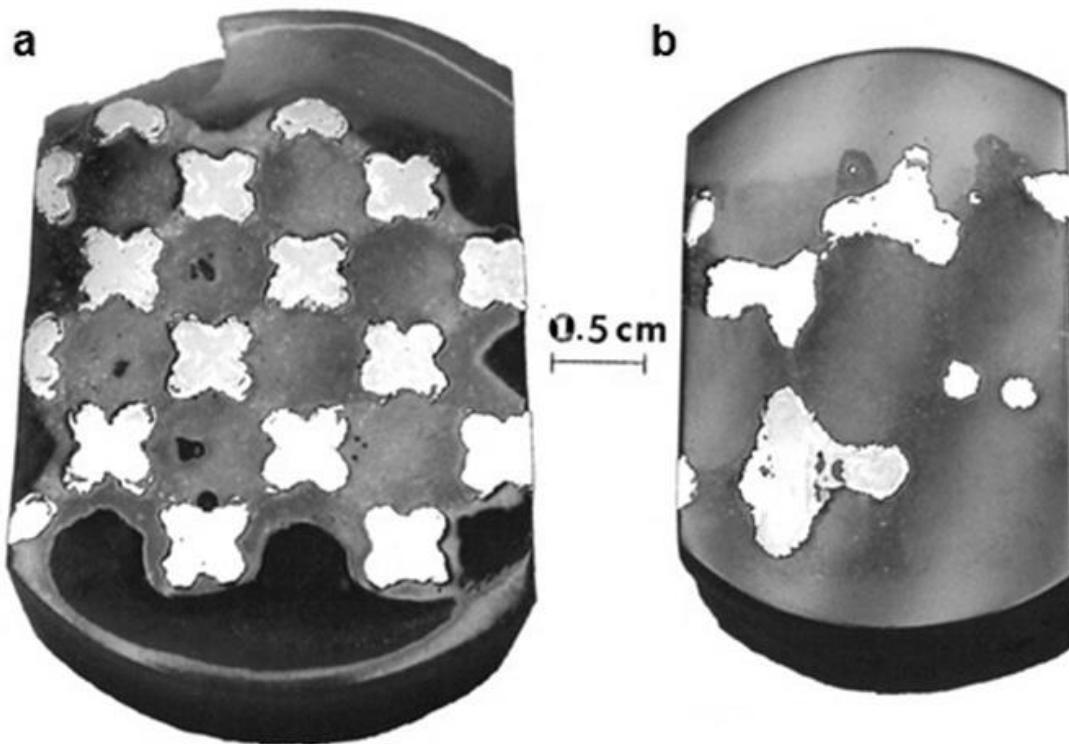


Figure 5.2.13: Blended TiAl mesh (a) and foam (b) cross-sections in the top face section perpendicular to the build direction. (a) corresponds to a density of 1.11 g/cm^3 ; (b) corresponds to a density of 0.74 g/cm^3 .

Figure 5.2.14 shows a horizontal reference plane section through a mesh component indicating zones of unmelted 2-phase TiAl powder particles. The enlarged view of a powder particle in Figure 5.2.14(b) (arrow) illustrates classical liquid-phase particle sintering showing a melt phase surrounding the 2-phase TiAl particle. These unmelted TiAl particle zones were also observed in the ligaments for the foam components, and occur as a consequence of the very rapid cooling of the mesh and foam struts and ligaments in contrast to the solid components. This rapid cooling differentiates the higher melting point gamma-TiAl powder particle ($\sim 1460^{\circ}\text{C}$) from the lower melting point Inconel 625 powder particles ($\sim 1336^{\circ}\text{C}$) (Froes, *et al.*, 1992) which allows the Inconel 625 powder blend to melt preferentially in some areas. This sinter/melt phenomena in the open-cellular component fabrication also alters the complex phase mixtures and morphologies in contrast to the solid components. These features are apparent on comparing the 3D OM composites for the mesh and foam components shown in Figure 5.2.15 and 5.2.16, respectively, with the microstructure composite for the blended solid components represented by Figure 5.2.7. Figure 5.2.17 also compares the XRD spectra corresponding to the horizontal reference plane (perpendicular to the build direction) for the mesh (Figure 5.2.17(a)) and foam (Figure 5.2.17(b)) components. In contrast to the corresponding XRD spectra for the solid blended TiAl components in the horizontal reference plane in Figure 5.2.10(a), there are subtle variations in peak intensities. It can be observed on careful comparison of Figure 5.2.7 with Figures 5.2.15 and 5.2.16, that the phase morphologies and sizes for the open-cellular components are similar in both the horizontal and vertical reference planes which are also similar to the vertical reference plane microstructure shown in Figure 5.2.7. The horizontal reference plane microstructures/phase structures in Figure 5.2.7 are somewhat different but as illustrated in Figure 5.2.11(a), the phase sizes range from ~ 100 nm to ~ 5 μm within stoichiometrically different zone or grain structures measuring ~ 10 μm . A similar range of size features are also observed in Figures 5.2.15 and 5.2.16 although the phase morphologies are different. The BE image in Figure 5.2.18 illustrates this feature for the horizontal reference plane for a mesh strut, corresponding to Figure 5.2.15. The phase compositions are referenced to the solid blend shown as A, B, C, and D in Figure 5.2.11(a).

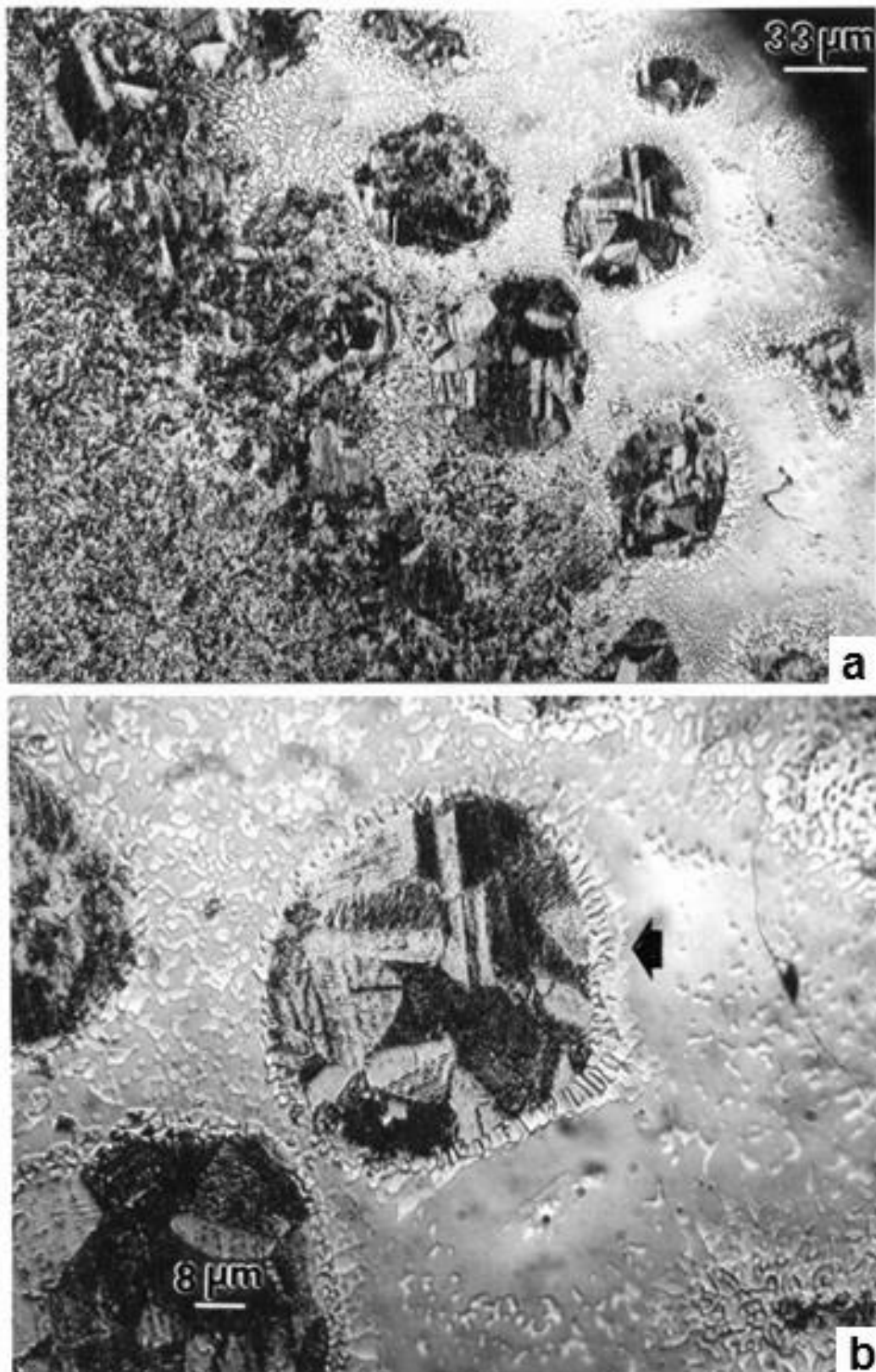


Figure 5.2.14: Polished and etched section for a mesh strut shown in Figure 5.2.13(a). Unmelted, liquid-phase sintered TiAl powder particles are observed in (a). (b) shows a magnified view of (a) (arrow).

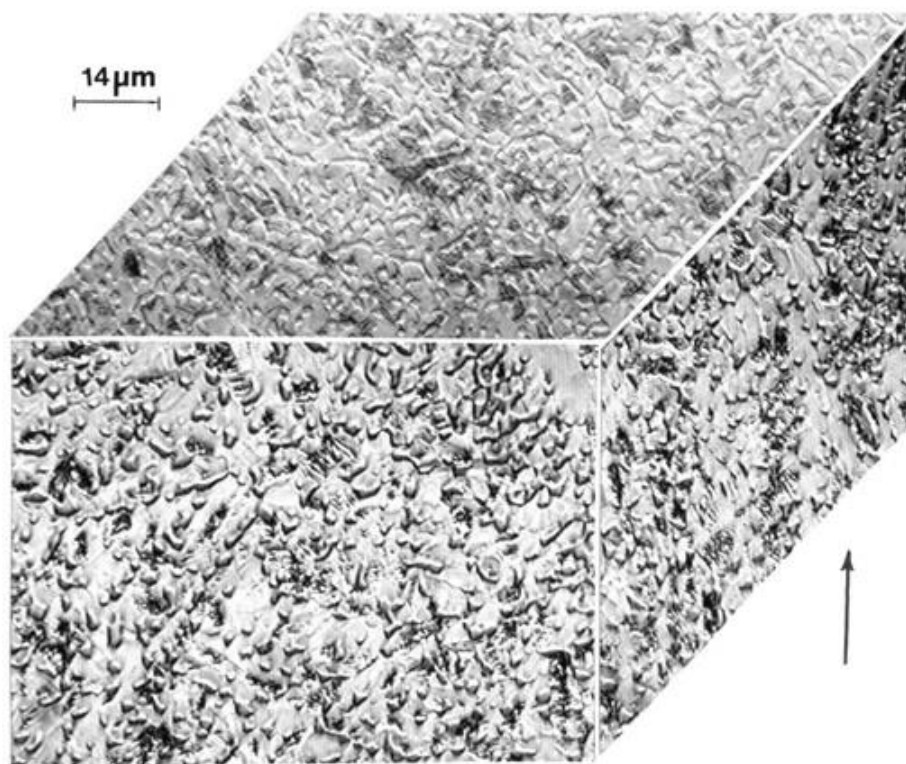


Figure 5.2.15: 3D OM composite for a mesh strut cross-section. The build direction is shown by arrow.

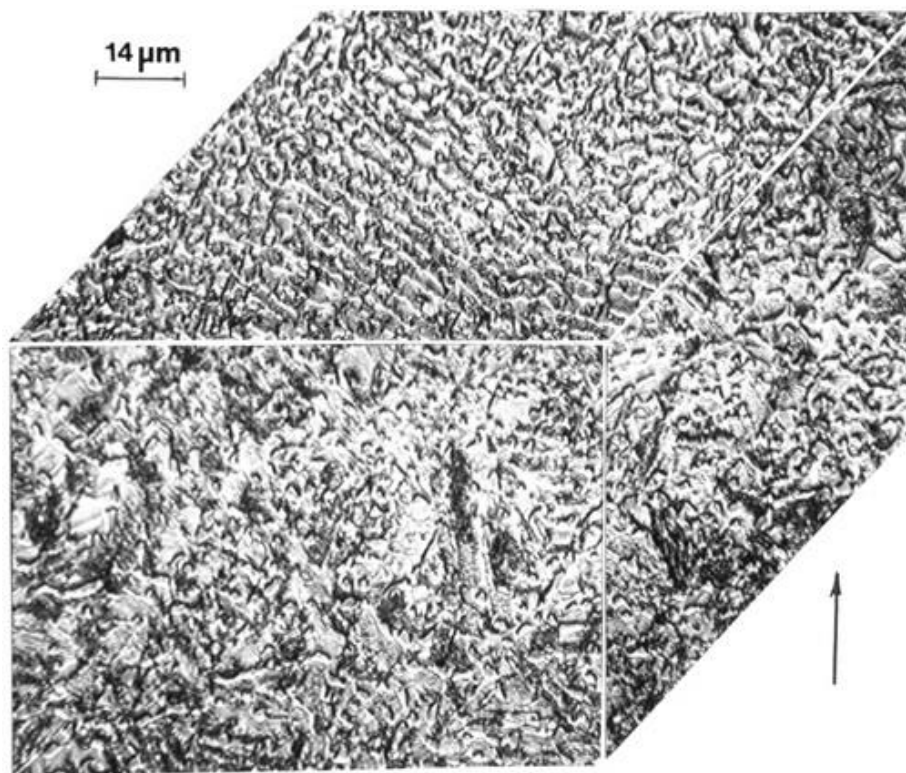


Figure 5.2.16: 3D OM composite for a foam ligament cross-section. The build direction is shown by arrow.

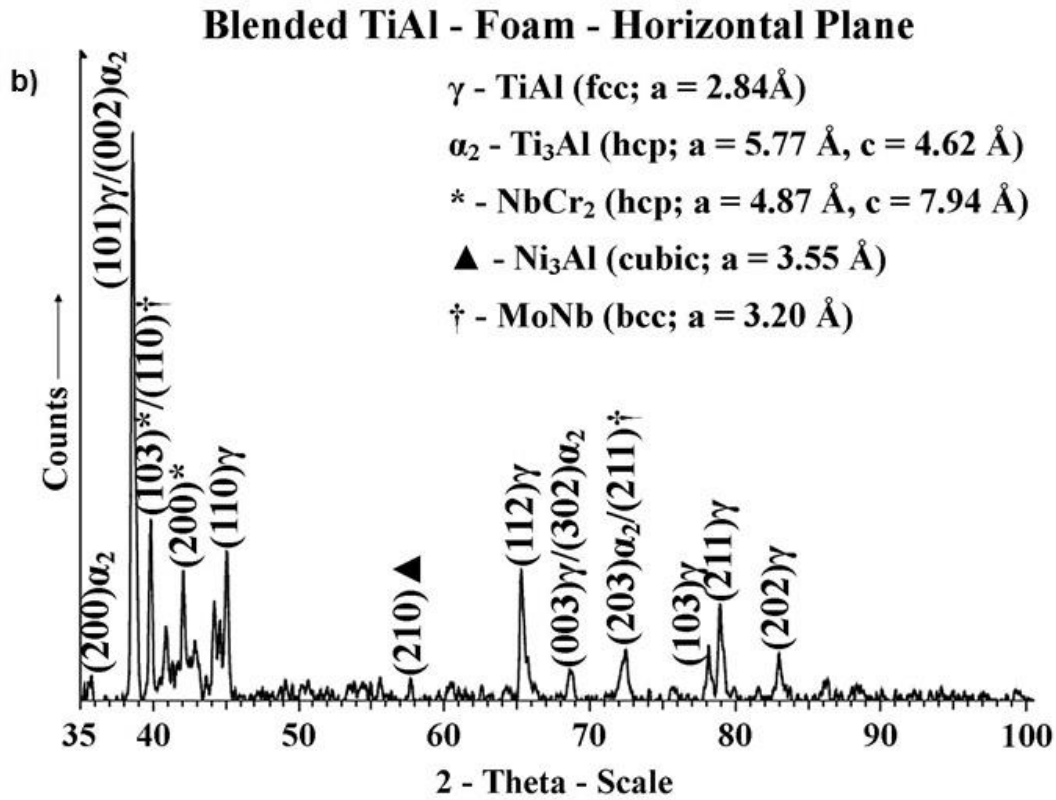
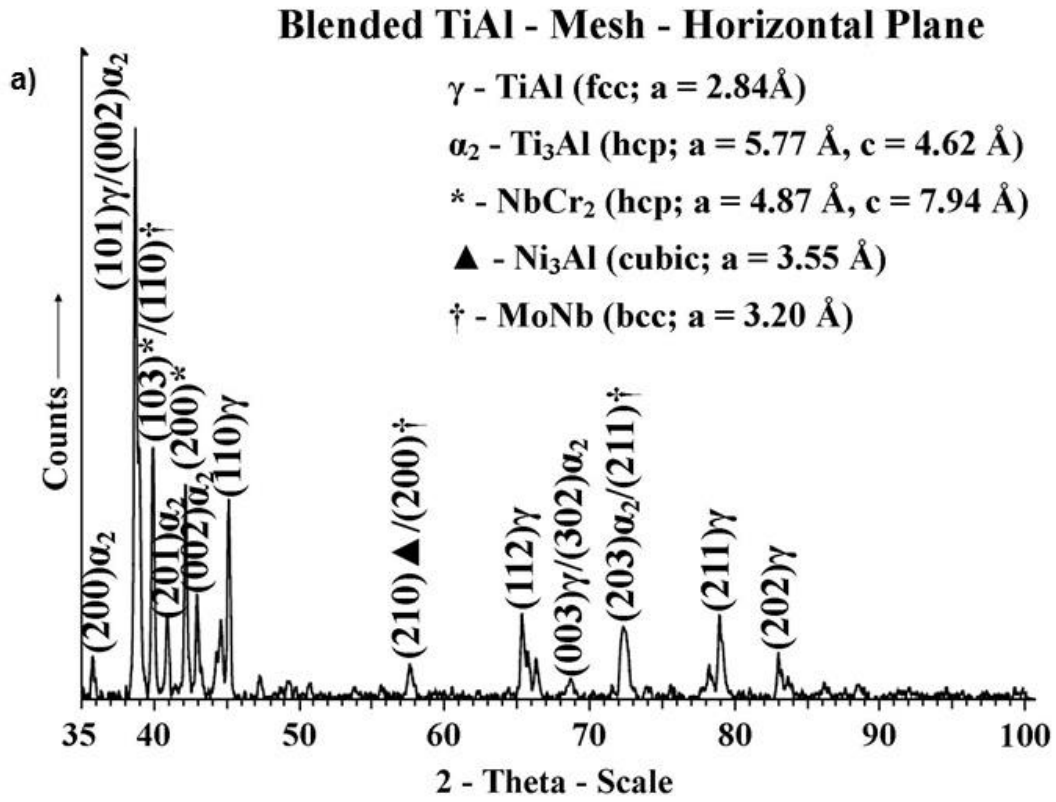


Figure 5.2.17: XRD spectra for blended TiAl mesh strut and foam ligament section. (a) Horizontal reference plane for a mesh strut. (b) Horizontal reference plane for a foam ligament.

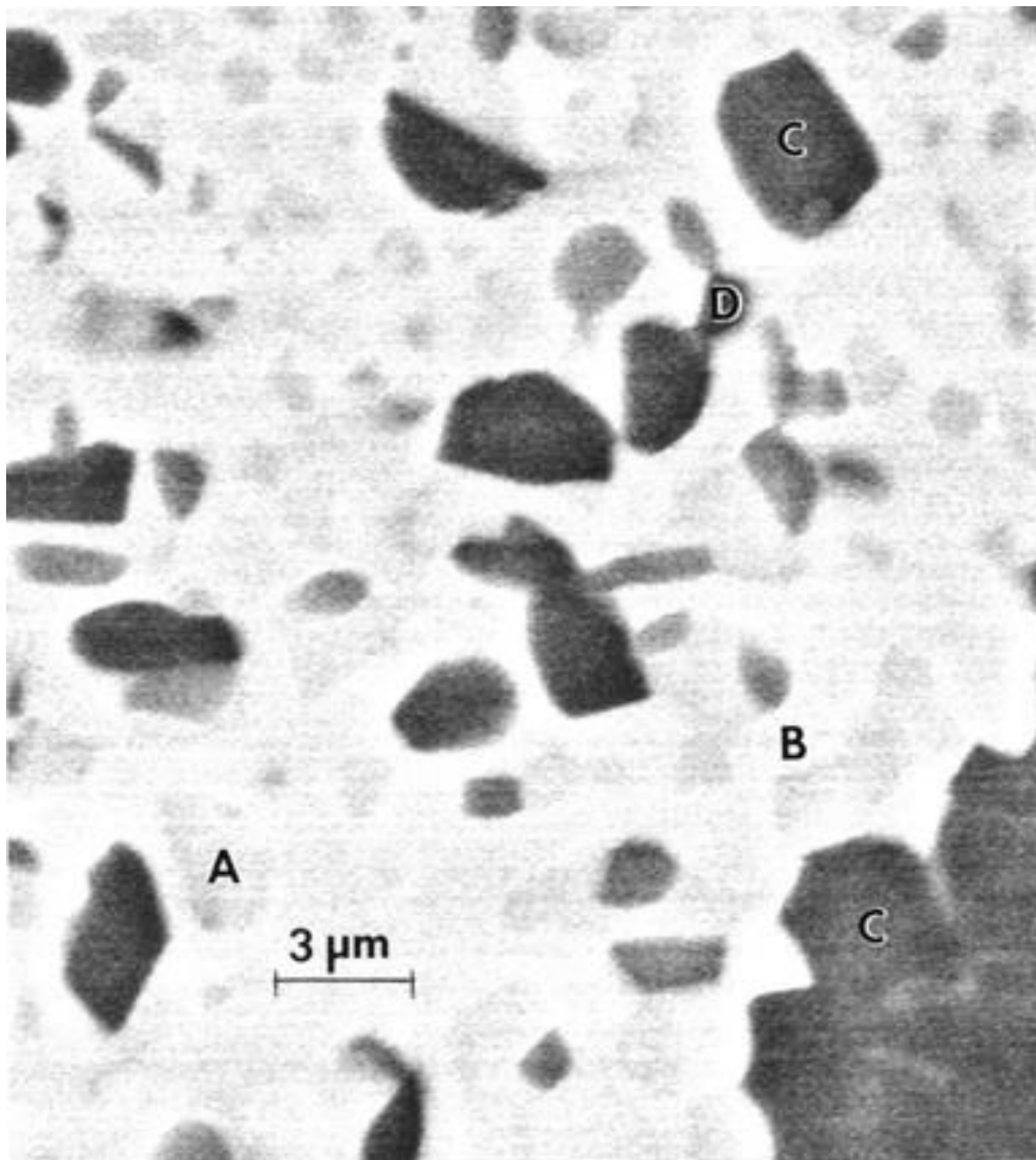


Figure 5.2.18: Backscatter electron (BE) image showing phase morphologies and stoichiometries referenced to Figure 5.2.11(a): A, B, C, and D.

5.2.4 Hardness Measurements

Figure 5.2.19 summarizes the hardness averages for blended TiAl solid and open-cellular (mesh and foam) components.

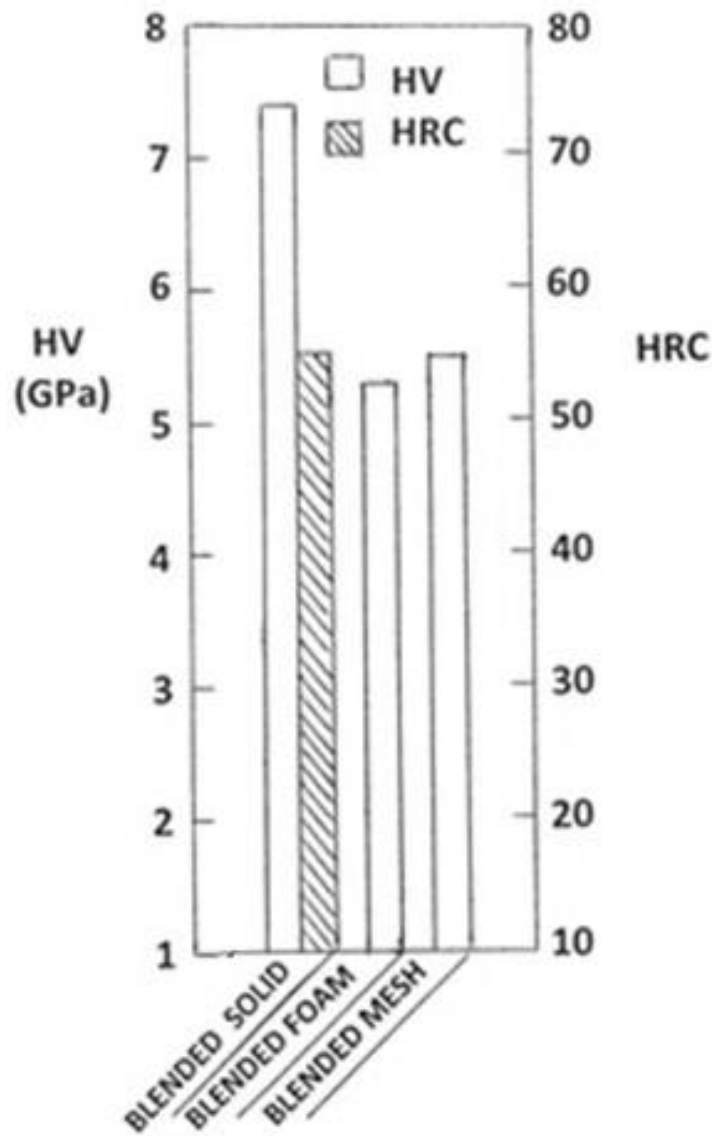


Figure 5.2.19: Vickers microindentation hardness (HV) and Rockwell C-scale macrohardness (HRC) measurements for blended TiAl alloy EBM-fabricated components.

5.2.5 Measurement of Dynamic Stiffness for Blended TiAl Mesh and Foam Components: Implications for Ideal Foam Model

Gibson and Ashby (1982) considered a simple lattice element structure similar to the mesh element utilized in this study, consisting of short, connected struts described by Timoshenko-type beams (Timoshenko & Gere, 1972) to derive a general open-cellular element relationship in the form:

$$E/E_0 = C_1 (\rho/\rho_0)^2 \quad (1)$$

where E_0 is the fully dense (solid) modulus (or dynamic stiffness) having a density ρ_0 , and C_1 is a constant. This ideal model has been demonstrated to fit a wide range of foam materials including polymers, aluminum and aluminum alloys, and other alloys (Gibson & Ashby, 1982; Murr, *et al.*, 2011b).

Table 5.2.3 lists the measured stiffnesses (E) and corresponding densities (ρ) for the blended TiAl foam and mesh components shown in Figure 5.2.12. Attempts to measure the fully dense ($\rho_0 = 4.13 \text{ g/cm}^3$) stiffness were unsuccessful because the solid, blended TiAl components were so brittle they shattered when impacted for resonant frequency production. This behavior is somewhat consistent with the high hardness as shown in Figure 5.2.19 and the presence of brittle phases such as NbCr_2 laves (Radakrishna, *et al.*, 1995) and the eutectic Ti_3Al and Ni_3Al phases. Consequently, in order to approximate the solid (dynamic) Young's modulus, we plotted values of E in Table 5.2.3 against corresponding densities (ρ), and extrapolated the fitted line in the log-log plot to $\rho = \rho_0 = 4.13 \text{ g/cm}^3$ as shown in Figure 5.2.20. The corresponding stiffness (E_0) was found to be 135 GPa at $\rho = \rho_0$ (Figure 5.2.20).

Table 5.2.3: Dynamic Stiffness and Density Measurements for TiAl/Ni-Cr Alloy (Blended TiAl)

Sample	Density $\rho \text{ (g/cm}^3\text{)}$	Stiffness $E \text{ (GPa)}$	ρ/ρ_0^*	E/E_0^*	Porosity [†] (%)
Foam	0.74	1.81	0.19	0.010	81
Foam	0.88	3.42	0.23	0.020	77
Foam	1.00	4.00	0.26	0.023	74
Mesh	1.02	3.43	0.26	0.020	74
Mesh	1.11	4.40	0.29	0.025	71
Mesh	1.32	7.31	0.34	0.040	66

* Solid density, $\rho_0 = 4.13 \text{ g/cm}^3$; solid stiffness, $E_0 = 135 \text{ GPa}$
 E_0 was determined graphically from Figure 5.2.20; at $\rho = 4.13 \text{ g/cm}^3$
for log-log plot of E versus ρ .

† Porosity calculated from density (ρ); porosity = $(1 - \rho/\rho_0) 100\%$

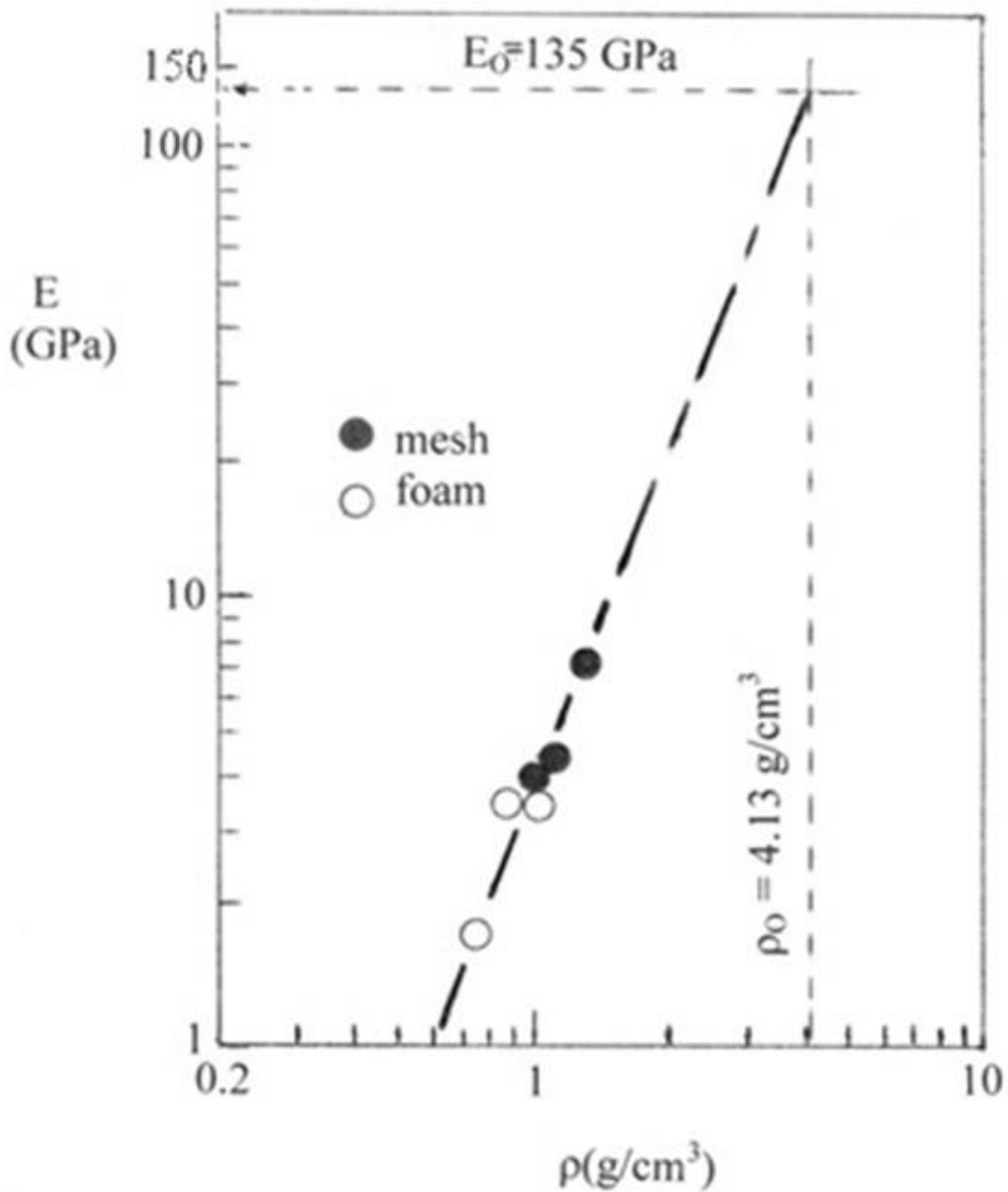


Figure 5.2.20: Log-log plot of measured stiffness versus density for the blended TiAl mesh and foam samples.

5.2.6 Summary

The mixing or blending of powders to produce novel alloy systems by additive manufacturing has been explored in this paper involving a 10:1 mixture of 2-phase TiAl : Inconel 625 alloy; having average powder particle sizes of 52 μm and 22 μm , respectively. The blended alloy produced a hardness increase of more than 30 percent over the hardest component in the mix, but there was no elongation

corresponding to a very brittle solid product. Because a systematic study of powder mixing ratios was not performed in this study, it is not possible to speculate on the much higher hardness developed. Additional, more systematic studies may shed some light on design strategies for alloy development using powder mixtures in electron beam melting. The implications of this work are that powder mixing or blending may provide a viable route to fabricate unique alloy systems, but considerably more systematic studies will be required to establish clear trends or routes for specific property development.

CHAPTER 6: DISCUSSION

6.1 TRANSMISSION ELECTRON MICROSCOPY

The contrasting microstructures evident on comparing Figures 5.2.6 and 5.2.7 are illustrated in more detail on comparing corresponding TEM bright-field images for each as shown in Figure 6.1.1. Figure 6.1.1(a) shows the thin lamellar α_2 (hcp Ti_3Al) phase coincident with the γ -TiAl {111} planes while Figure 6.1.1(b) shows a complete absence of this lamellar microstructure within a multiphase region represented by the enclosure shown in the horizontal reference plane for the 3D image composition in Figure 5.2.7 for the blended TiAl.

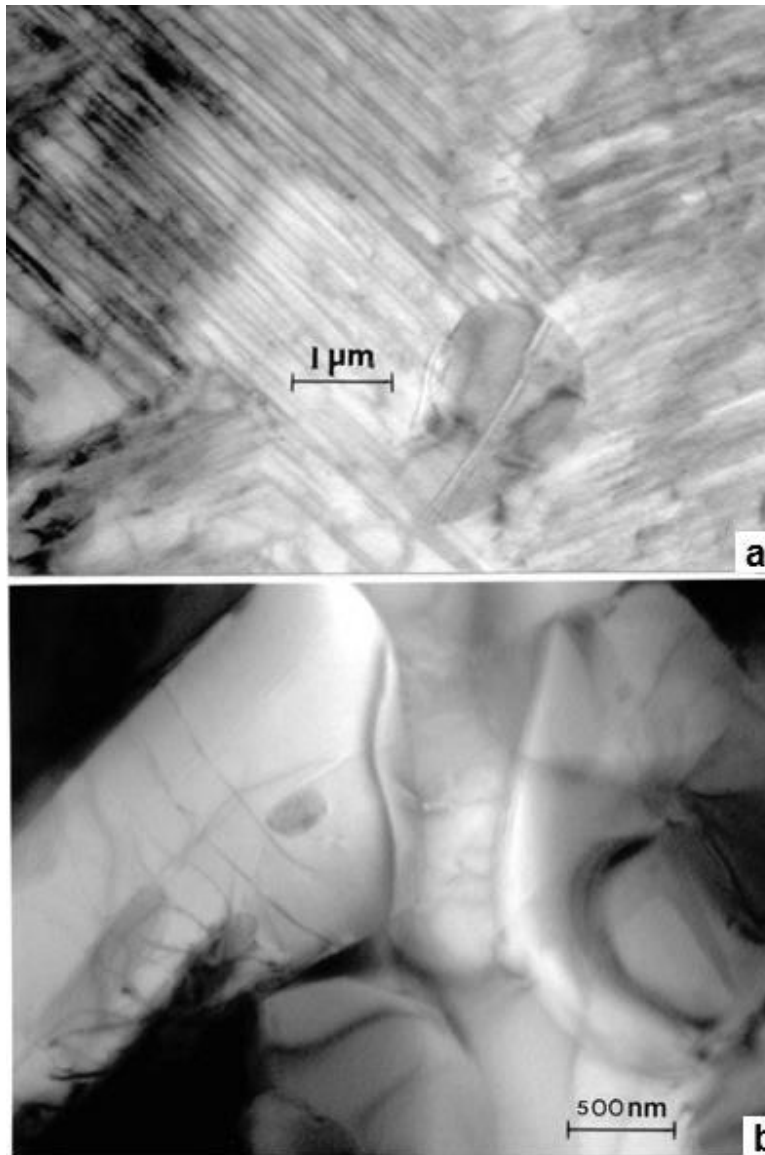


Figure 6.1.1: TEM horizontal plane section views (perpendicular to the build direction). (a) 2-phase TiAl. (b) Blended TiAl.

6.2 HARDNESS

Figure 6.2.1 summarizes the hardness averages for solid EBM components of Inconel 625 and 2-phase TiAl in contrast with the precursor powders and blended TiAl solid and open-cellular (mesh and foam) components. Note that HRC measurements were not possible for the powders and, mesh and foam components, while HV measurements were made for all of the samples. It is interesting to note the significant hardness increase for the blended TiAl solid components in contrast to both of the mixed powders (Inconel 625 and TiAl). The increase in the solid blend over the 2-phase TiAl is observed to be ~40% in Figure 6.2.1. Correspondingly, the blended TiAl mesh and foam hardness increased ~30% relative to the TiAl solid components, although the Vickers microindentation hardness (HV) for the precursor (pre-alloyed) 2-phase TiAl powder remained the same for both the EBM-fabricated mesh and foam components from blended TiAl powder.

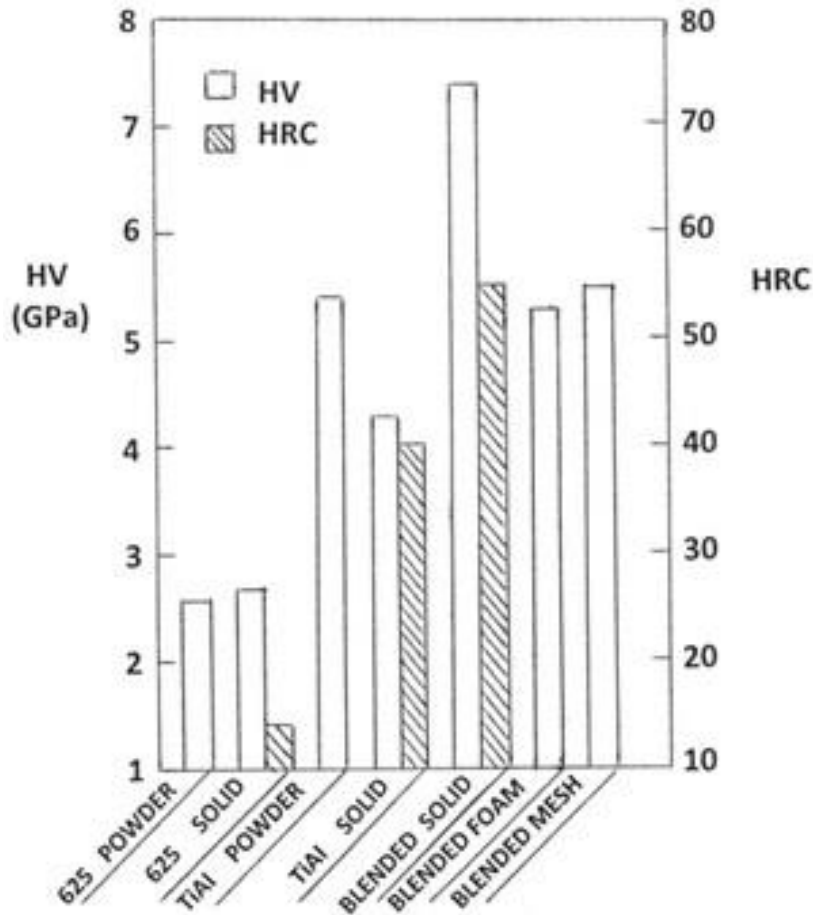


Figure 6.2.1: Comparison of Vickers microindentation hardness (HV) and Rockwell C-scale macrohardness (HRC) measurements. Blended refers to the blended TiAl components – 10:1 – 2-phase TiAl : Inconel 625.

6.3 DYNAMIC STIFFNESS

The stiffness value, $E = E_0 = 135$ GPa, was employed to calculate relative stiffness values (E/E_0) as shown in Table 5.2.3, and these values were plotted against relative density values (ρ/ρ_0) as shown in the log-log plot in Figure 6.3.1; in comparison with data for Ti-6Al-4V where $E_0 = 110$ GPa, and a Co-base superalloy where $E_0 = 210$ GPa (Murr, *et al.*, 2010; 2011b). The data in Figure 6.3.1 is very closely fitted to a straight line with $n = 2$. This is especially notable because the blended TiAl alloy is very complex, and taken together with other relative stiffness versus relative density log-log plotted data (Murr, *et al.*, 2010; 2011b; 2012) strengthens the case for metal alloy open-cellular structures generally following the ideal foam relationship shown in eqn. (1).

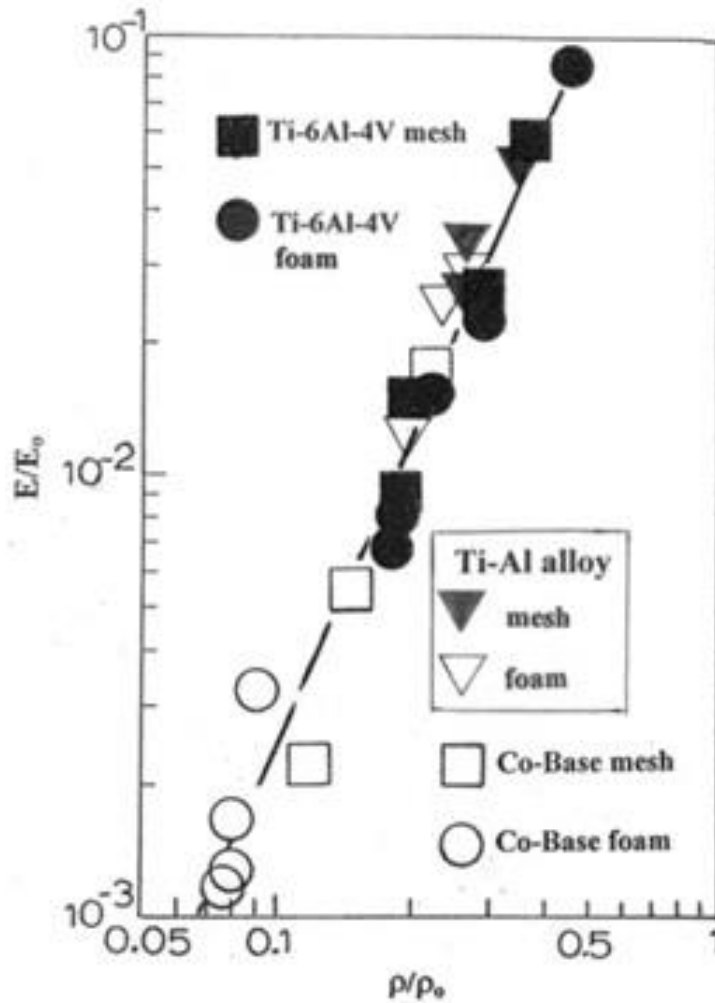


Figure 6.3.1: Log-log plot of relative stiffness versus relative density for blended TiAl mesh and foam components (indicated by Ti-Al alloy) in comparison with Ti-6Al-4V and Co-based alloy data from Murr et al. (2010a, 2010b).

CHAPTER 7: CONCLUSIONS

Gamma TiAl is an advanced material available in powder form for use in additive manufacturing processes. In bulk form, γ -TiAl has good resistance against oxidation and corrosion up to $\sim 700^{\circ}\text{C}$, as well as high specific stiffness and low density of $\sim 3.85 \text{ g/cm}^3$. This material also has good thermo-physical properties, such as, high melting point, high elastic modulus, and good structural stability. These properties make this material an excellent candidate for use in aerospace applications, especially to replace the heavier nickel-based superalloy used in low pressure turbine blades. In these studies, it was important to obtain valuable results comparable to results obtained in previous studies of not only γ -TiAl-based superalloys, but other “advanced” materials as well.

It is shown, in this study, that the microstructure of Ti-48Al-2Cr-2Nb can be altered by different heat treatment cycles. Therefore, it is possible to obtain any desired microstructure from EBM-fabricated material using sufficient heat treatment cycles. The goal here is to improve the overall properties of the materials.

The EBM technology is an excellent way to manufacture different TiAl components that are superior compared to that of other processes. This technology system allows for near net shape components of TiAl material to be manufactured having complex shapes, for example, turbine blades for aircraft engines. This is almost near impossible to manufacture using conventional processes, if so, there are many steps involved. Steps, such as machining, that are time consuming and tedious in conventional manufacturing processes, such as casting, forging, or wrought, are able to be eliminated in the process of additive manufacturing because any sort of tool or fixture is not needed. Additive manufacturing by electron beam melting is very cost-efficient and energy-efficient, and there is very little waste material.

Even though the blended alloy wasn't at all “planned”, the blended TiAl open-cellular mesh and foam components used in this research exhibited relative stiffness versus relative hardness values fitted to an ideal foam log-log line slope for $n = 2$. Therefore, we were still able to prove that any metal or alloy will generally follow the ideal open-cellular relationship: $E/E_0 = (\rho/\rho_0)^2$.

REFERENCES

- Amato, K. N., Hernandez, J., Murr, L. E., Martinez, E., Gaytan, S. M., Shindo, P. W., Collins, S., 2012. Comparison of microstructures and properties for a Ni-base superalloy (Alloy 625) fabricated by electron and laser beam melting. *J. Materi. Sci. Res.* 1, Vol. 2, 2-41.
- Angel, P. C., & Subramanian, R., 2009., *Powder Metallurgy: Science, Technology & Applications*, PHI Learning Private, Ltd., New Delhi.
- Appel, F., Wagner, R., 1998. Microstructure and deformation of two-phase γ -titanium aluminides. *Mater. Sci. Eng.* 187-268.
- Appel, F., Borssmann, U., Christoph, U., Eggert, S., Janschek, P., Lorenz, U., ... Paul, J.D.H., 2000. Recent Progress in the Development of Gamma Titanium Aluminide Alloys. *Advanced Engineering Materials*, 2, No. 11, 699-720.
- Appel, F., Paul, D. H., Oehring, M., 2011., *Gamma Titanium Aluminide Alloys*. Wiley-VCH.
- ARCAM. <<http://www.arcam.com/technology/ebm-process.aspx>>
- Arcam A2: Setting the Standard for Additive Manufacturing.
<<http://www.arcam.com/CommonResources/Files/www.arcam.com/Documents/Products/Arcam-A2.pdf>>
- Biamino, S. et al., 2011. Electron beam melting of Ti-48Al-2Cr-2Nb alloy: Microstructure and mechanical properties investigation. *Intermetallics*. 19, 776-781.
- Choi, B.W., Deng, C., McCullough, C., Paden, B., Mehrabian, R., 1990. Densification of Rapidly Solidified Titanium Aluminide Powder – I. Comparison of Experiments to HIPing Models. *Acta metall. mater.*, 38, No. 11, 2225-2243.
- Clemens, Helmut and Kestler, Heinrich, 2000. Processing and Applications of Intermetallic γ -TiAl-Based Alloys. *Advanced Engineering Materials*. 2, No. 9, 551-570.
- Franzen, S. F., Karlsson, J., 2010. γ -Titanium Aluminide Manufactured by Electron Beam Melting.
- Froes, F.H., Suryanarayana, C., Eliezer, D., 1992. Review: Synthesis, properties and applications of titanium aluminides. *J. Materi. Sci.* 27, 5113-5140.
- German, R. M. ,2005. *A-Z of Powder Metallurgy*. Metal Powders Technology Series: Bernard Williams.
- Gibson, L.J. & Ashby, M.F., 1982. The mechanics of three-dimensional cellular materials. *Proc. Roy. Soc. London A, Math Phys. Sci.*, 382, 43-59.
- Gibson, L.J. & Ashby, M.F., 1997. *Cellular Solids: Structure and Properties* (2nd Ed.). England: Cambridge Univ. Press.
- Gibson, I., Rosen, D.W., Stucker, B., 2010. *Additive Manufacturing Technologies: Rapid Prototyping to Direct Digital Manufacturing*. Springer.
- Hernandez, J., Murr, L.E., Gaytan, S.M., Martinez, E., Medina, F., Wicker, R.B., 2012a. Microstructures For Two-Phase Gamma Titanium Aluminide Fabricated by Electron Beam Melting. *Metallogr. Microstruct. Anal.* 1, 14-27.
- Hernandez, J., Murr, L.E., Amato, K.N., Martinez, E., Shindo, P.W., Terrazas. C.A., Rodriguez, E., Medina, F., Wicker, R.B., Li, S.J., Cheng, X.Y., Yang, F., 2012b. Microstructures and Properties

for a Superalloy Powder Mixture Processed by Electron Beam Melting. *Journal of Materials Science Research*, Vol. 1, No. 3, 124-144.

- Jang, W.Y., Kraynik, A.M., Kyriakides, S., 2008. On the microstructure of open-cell foams and its effect on elastic properties. *Solids & Structures*, 45, 1845-1875.
- Kim, Y. W., 1994. Ordered intermetallic alloys: Part III: Gamma titanium aluminides. *JOM*, 46, 30-35.
- Kim, Y.W., Wagner, R., Yamaguchi, M. (eds.), 1995. *Gamma Titanium Aluminides*. TMS, Warrendale.
- Koeppel, C., Bartels, A., Seeger, J., Mecking, H., 1993. General aspects of the thermomechanical treatment of two-phase intermetallic TiAl compounds. *Metall. Trans.*, 24A, 1975-1802.
- London, B., 1993. *Structural Intermetallics*. TMS, Warrendale, p. 151.
- Lu, L., Shen, Y.F., Chen, X.H., Qian, L., Lu, K., 2005. Ultrahigh strength and high electrical conductivity in copper. *Science*, 304, 422-426.
- Lu, K., Lu, L., Suresh, S., 2009. Strengthening materials, by engineering coherent internal boundaries at the nanoscale. *Science*, 324, 349-352.
- Murr, L.E., 1975. *Interfacial Phenomena in Metals and Alloys*. Addison-Wesley, Reading (reprinted in 1990 and available from CRBL.com).
- Murr, L.E. et al., 2009. Advanced Metal Powder Based Manufacturing of Complex Components by Electron Beam Melting. *Materials Technology*, Vol. 24, No. 3, 180-190.
- Murr, L.E., Gaytan, S.M., Medina, F., Lopez, H., Martinez, E., Machado, B.I., Hernandez, D.H., Martinez, L., Lopez, M.I., Wicker, R.B., Bracke, J., 2010a. Next-generation biomedical implants using additive manufacturing of complex, cellular and functional mesh arrays. *Phil. Trans. R. Soc. A*, 368, 1999-2032.
- Murr, L.E. et al., 2010b. Next generation biomedical implants using additive manufacturing of complex cellular and functional mesh arrays. *Phil. Trans. Roy. Soc. A* 368, 1999-2032.
- Murr, L. E., Martinez, E., Gaytan, S. M., Ramirez, D. A., Machado, B. I., Shindo, P. W., Wicker, R. B., 2011a. Microstructural architecture, microstructures, and mechanical properties for a nickel-base superalloy fabricated by electron beam melting. *Metall. Mater. Trans. A*, 42A, 3491-3508.
- Murr, L.E., Li, S.J., Tian, Y.X., Amato, K., Martinez, E., Medina, F., 2011b. Open-cellular Co-base and Ni-base superalloys fabricated by electron beam melting. *Materials*, 4, 782-790.
- Murr, L. E., Gaytan, S. M., Ramirez, D. A., Martinez, E., Hernandez, J., Amato, K. N., Shindo, P. W., Medina, F., Wicker, R. B., 2012. Metal fabrication by additive manufacturing using laser and electron beam melting technologies. *J. Mater. Sci. Technol.*, 28, 1, 1-14.
- Peretti, M. W., 2012. Titanium for Non-Aerospace Applications. *JOM*, 64, No. 5, 551-552.
- Porter, W. J. III, John, R., Olson, S., 2003. Determination of Young's Modulus of Grains in a Gamma Titanium Aluminide Alloy. *Scripta Metall.*, 49, 327-332.
- Radikrishna, C., Rao, K.P., Srinivas, S., 1995. Laves Phase in Superalloy 718 weld metals. *J. Mater. Sci. Lett.*, 14, 1810-1812.
- Sabbadini, Salvia, et al. Additive Manufacturing of Gamma Titanium Aluminide Parts by Electron Beam Melting. Seattle, Washington, USA : Washington State Convention Center, 2010. TMS 2010 139th Annual Meeting & Exhibition. February 14-18.

- Sachdev, A. K., Kulkarni, K., Fang, Z. Z., Yang, R., Girshov, V., 2012. Titanium for Automotive Applications: Challenges and Opportunities in Materials and Processing. JOM, 64, No. 5, 553-565.
- Timoshenko, S., Gere, J.M., 1972. Mechanics of Materials. Van Nostrand, Reinhold G. New York.
- Wagner, R., Appel, F., Dugan, B., Eniss, R.J., Lorenz, U., Mullauer, J., Nicolai, H.P., Quadakkers, W., Singheiser, L., Smarsly, W., Vaidya, W., Wurzwallner, K., 1975, in Gamma Titanium Aluminides, ed. By Kim, Y.W., Wagner, R., Yamaguchi, M. Tms, Warrendale, p. 387.

APPENDIX A: PERMISSION TO INCLUDE MATERIAL FROM THE JOURNAL METALLOGRAPHY, MICROSTRUCTURE, AND ANALYSIS

Re: Permission to use published paper

Sue Sellers [Sue.Sellers@asminternational.org]

Sent: Tuesday, February 05, 2013 8:19 AM

To: Hernandez, Jennifer [jhernandez42@miners.utep.edu]

Dear Ms. Hernandez,

You can request permission to use your *Metallography, Microstructure, and Analysis* paper in your dissertation by going through RightsLink at the link below. There is no charge to use the paper as you are the original author and using it for your dissertation although you are required to obtain a license through Rightslink.

<https://s100.copyright.com/AppDispatchServlet?publisherName=Springer&imprint=Springer+Science%2BBusiness+Media%2C+LLC+and+ASM+International&publication=2192-9262&title=Microstructures+for+Two-Phase+Gamma+Titanium+Aluminide+Fabricated+by+Electron+Beam+Melting&publicationDate=2012&author=Jennifer+Hernandez&AuthorEmail=jhernandez42%40miners.utep.edu&authorAddress=El+Pas+TX%2C+79968%2C+USA&contentID=10.1007%2Fs13632-011-0001-9&volumeNum=1&issueNum=1&startPage=14&endPage=27&orderBeanReset=true&orderSource=SpringerLink>

Best Regards,
Sue

Sue Sellers

Product & Project Administrator
ASM International
9639 Kinsman Road
Materials Park, OH 44073- 0002
440.338.5151, ext. 5465
sue.sellers@asminternational.org

=====
Permission to use published paper

Hernandez, Jennifer [jhernandez42@miners.utep.edu]

Sent: Friday, February 1, 2013 2:40 PM

To: Ania Levinson [ania.levinson@springer.com]

Hello Ms. Levinson,

My name is Jennifer Hernandez and I am a Ph.D. candidate graduating May 2013. I have submitted a paper to the journal, *Metallography, Microstructure, and Analysis*, and it was accepted and published February 2012 in Volume 1, Issue 1. The title to the paper is "Microstructures for Two-Phase Gamma

Titanium Aluminide Fabricated by Electron Beam Melting". Our university allows us to use published journal papers as part of our final dissertation document. Therefore, I wanted to ask for permission to include my paper in my dissertation. Please let me know if I need to give you more information or if I need to do something further.

Thank you,
Jennifer Hernandez

SPRINGER LICENSE TERMS AND CONDITIONS

Feb 05, 2013

This is a License Agreement between Jennifer Hernandez ("You") and Springer ("Springer") provided by Copyright Clearance Center ("CCC"). The license consists of your order details, the terms and conditions provided by Springer, and the payment terms and conditions.

All payments must be made in full to CCC. For payment instructions, please see information listed at the bottom of this form.

License Number	3082630600529
License date	Feb 05, 2013
Licensed content publisher	Springer
Licensed content publication	Metallography, Microstructure, and Analysis
Licensed content title	Microstructures for Two-Phase Gamma Titanium Aluminide Fabricated by Electron Beam Melting
Licensed content author	Jennifer Hernandez
Licensed content date	Jan 1, 2012
Volume number	1
Issue number	1
Type of Use	Thesis/Dissertation
Portion	Full text
Number of copies	1
Author of this Springer article	Yes and you are the sole author of the new work
Order reference number	
Title of your thesis / dissertation	Microstructures and Properties for Titanium Aluminide Superalloy Prototypes Fabricated by Electron Beam Melting and Thermally Processed
Expected completion date	May 2013
Estimated size(pages)	98
Total	0.00 USD

APPENDIX B: PERMISSION TO INCLUDE MATERIAL FROM THE JOURNAL OF MATERIALS SCIENCE RESEARCH

Re: Permission to use published paper

Journal of Materials Science Research [jmsr@ccsenet.org]

Sent:

To: Hernandez, Jennifer [jhernandez42@miners.utep.edu]

Dear Jennifer Hernandez,

You got the permission to include your paper "Microstructures and Properties for a Superalloy Powder Mixture Processed by Electron Beam Melting" (JMSR-V1N3) in your dissertation.

Best regards,

Lily Green

Editorial Assistant

Journal of Materials Science Research

2012-12-12

1120 Finch Avenue West, Suite 701-309, Toronto, ON., M3J 3H7, Canada

Tel: 1-416-642-2606 ext.241

Fax: 1-416-208-2608

E-mail: jmsr@ccsenet.org

Website: www.ccsenet.org/jmsr

=====
Permission to use published paper

Hernandez, Jennifer [jhernandez42@miners.utep.edu]

Sent: Tuesday, December 11, 2012 12:19 PM

To: Lily Green [jmsr@ccsenet.org]

Hello Ms. Green,

My name is Jennifer Hernandez and I am a Ph.D. candidate graduating May 2013. I submitted a paper to the *Journal of Materials Science Research*, and it was accepted and published July 2012 in Volume 1, No. 3. The title to the paper is "Microstructures and Properties for a Superalloy Powder Mixture Processed by Electron Beam Melting". Our university allows us to attach an exact copy of my entire published journal paper as part of our final dissertation document. Therefore, I wanted to ask for permission to include my paper in my dissertation. Please let me know if I need to give you more information or if I need to do something further.

Thank you,

Jennifer Hernandez

VITA

Jennifer Hernandez was born in El Paso, Texas on December 16, 1987. She is the daughter of Antonio and Antonia Elorreaga, and older sister to Andrea Marie and Jason Nicholas Elorreaga. She was awarded her Bachelor of Science degree in Metallurgical and Materials Engineering at The University of Texas at El Paso in May of 2010. She has been awarded a number of scholarships, including the Workforce Solutions STEM Scholarship and Thelma E. Morris Endowed Graduate Scholarship, to name a few and a Graduate Research Award. While pursuing her degree, Jennifer worked as a teaching assistant and research assistant for the department of Metallurgical and Materials Engineering. She has had the privilege to present her research at international conference meetings including TMS 2013 Annual Meeting & Exhibition and the MS&T 2011 Conference and Exhibition. Jennifer is the co-author of several publications and the main author of two publications.

Publications/Projects assisted/Co-authored by Jennifer Hernandez:

* L.E. Murr, E. Martinez, **J. Hernandez**, S. Collins, K.N. Amato, S.M. Gaytan, and P.W. Shindo. Microstructures and Properties of 17-4 PH Stainless Steel Fabricated by Selective Laser Melting. *Journal of Materials Research and Technology*, 2012, Vol. 1 (3), 167-177.

* **J. Hernandez**, L.E. Murr, K.N. Amato, E. Martinez, P.W. Shindo, C.A. Terrazas, E. Rodriguez, F. Medina, R.B. Wicker, S.J. Li, X.Y. Cheng, and F. Yang. Microstructures and Properties for a Superalloy Powder Mixture Processed by Electron Beam Melting. *Journal of Materials Science Research*, 2012, Vol. 1 (3), 124-144.

* **J. Hernandez**, L.E. Murr, S.M. Gaytan, E. Martinez, F. Medina, and R.B. Wicker. Microstructures for Two-Phase Gamma Titanium Aluminide Fabricated by Electron Beam Melting. *Metallurgy, Microstructure, & Analysis*, 2012, Vol.1 (1), 14-27.

* L.E. Murr, E. Martinez, K.N. Amato, S.M. Gaytan, **J. Hernandez**, D.A. Ramirez, P.W. Shindo, F. Medina, and R.B. Wicker. Fabrication of Metal and Alloy Components by Additive Manufacturing: Examples of 3D Materials Science. *Journal of Materials Research and Technology*, 2012, 42-54.

* K.N. Amato, S.M. Gaytan, L.E. Murr, E. Martinez, P.W. Shindo, **J. Hernandez**, S. Collins, and F. Medina. Microstructures and Mechanical Behavior for Inconel 718 Fabricated by Selective Laser Melting. *Acta Materialia*, 2012, Vol. 60 (5), 2229-2239.

* L.E. Murr, S.M. Gaytan, D.A. Ramirez, E. Martinez, **J. Hernandez**, K.N. Amato, P.W. Shindo, F. Medina, and R.B. Wicker. Metal Fabrication by Additive Manufacturing Using Laser and Electron Beam Melting Technologies. *Materials, Science, and Technology*, 2012, Vol. 28 (1), 1-14.

* K.N. Amato, **J. Hernandez**, L.E. Murr, E. Martinez, S.M. Gaytan, and P.W. Shindo. Comparison of Microstructures and Properties for a Ni-Base Superalloy (Alloy 625) Fabricated by Electron and Laser Beam Melting. *Journal of Materials Science Research*, 2012, Vol. 1 (2), 3-41.

* L.E. Murr, E. Martinez, K.N. Amato, **J. Hernandez**, P.W. Shindo, S.M. Gaytan, D.A. Ramirez, F. Medina, and R.B. Wicker. 3D Microstructural Architectures for Metal and Alloy Components Fabricated by 3D Printing/Additive Manufacturing Technologies. *Proceedings of 1st International Conference on 3D Materials Science*, submitted, 2012.

* L.E. Murr, E. Martinez, **J. Hernandez**, S. Collins, K.N. Amato, S.M. Gaytan, and P.W. Shindo. Microstructures and Properties of 17-4 PH Stainless Steel Fabricated by Selective Laser Melting. *Materials Science and Engineering: A*, 2011

* S. K. Varma, C. Parga, K. Amato, and **J. Hernandez**. Microstructures and High Temperature Oxidations Resistance of Alloys from Nb-Cr-Si System. *Journal of Materials Science*, 2010, Vol. 45 (14), 3931-3937.

Presentations:

* **J. Hernandez**, K. Thomas, E. Soto, D. Alvarez, and S.K. Varma. Phase stability in Nb-(20, 25)Cr-(20, 15) Si-5Al from 700°C to 1400°C. *Materials, Science, and Technology 2010 Conference and Exhibition (MS&T'10)*, Houston, Texas, October 17-21, 2010. Poster Presentation.

* **J. Hernandez**, L.E. Murr, S.M. Gaytan, E. Martinez, S.J. Li, X.Y. Cheng, F. Medina, and R. Wicker. Microstructures and Properties of Solid and Open-Cellular γ -TiAl Fabricated by Electron Beam Melting (EBM). *The Minerals, Metals, and Materials Society (TMS) 2012 141st Annual Meeting & Exhibition*, Orlando, Florida, March 11-March 15, 2012. Oral Presentation.

* **J. Hernandez**, L.E. Murr, S.M. Gaytan, E. Martinez, S.J. Li, X.Y. Cheng, F. Medina, and R. Wicker. Novel TiAl Open-Cellular Structure Fabricated by Electron Beam Melting. *Materials, Science, and Technology 2010 Conference and Exhibition (MS&T'10)*, Columbus, Ohio, October 16-20, 2011. Oral Presentation.

* **J. Hernandez**, S.J. Li, E. Martinez, L.E. Murr, X. Pan, K. Amato, X.Y. Cheng, F. Yang, C.A. Terrazas, E. Rodriguez, S.M. Gaytan, Y.L. Hao, R. Yang, F. Medina, and R.B. Wicker. *The Minerals, Metals, and Materials Society (TMS) 2013 142nd Annual Meeting & Exhibition*, San Antonio, Texas, March 3-7, 2013. Poster Presentation.

* **J. Hernandez**, L.E. Murr, S.J. Li, X.Y. Cheng, F. Medina, and R.B. Wicker. Titanium Aluminide Solid and Open-Cellular Prototypes Fabricated by Electron Beam Melting (EBM): Microstructures and Properties. *22nd Annual Solid Freeform Fabrication Symposium*, University of Texas at Austin, August 8-10, 2011. Poster Presentation.

* **J. Hernandez**, L.E. Murr, F. Medina, and R.B. Wicker. Titanium Aluminide Prototypes Fabricated by Electron Beam Melting. *The Minerals, Metals, and Materials Society (TMS) 2011 140th Annual Meeting & Exhibition*, San Diego, California, February 27-March 3, 2011. Poster Presentation.

* **J. Hernandez**, K. Thomas, E. Soto, D. Alvarez, and S.K. Varma. Phase stability in Nb-(20, 25)Cr-(20, 15) Si-5Al from 700°C to 1400°C. *Materials, Science, and Technology 2010 Conference and Exhibition (MS&T'10)*, Houston, Texas, October 17-21, 2010. Poster Presentation.

Permanent address: 9818 Honolulu

El Paso, Texas 79925

This dissertation was typed by Jennifer Hernandez.